## Politecnico di Milano

School of Industrial and Information Engineering

Master thesis in Materials engineering and nanotechnology

# Hydrogen treated Titania nanostructures for photoelectrochemical (PEC) Water Splitting

Supervisor:
**Prof. Andrea Li Bassi**

Co-supervisor:
**Dr. Luca Mascaretti**

Candidate:
**Simona Ferrulli**
**Id:804593**

## Abstract

Photoelectrochemical (PEC) solar water splitting represents a green and low cost method to produce clean hydrogen fuel from solar energy and water. The nanostructured semiconductor photoanode is a key component of the PEC cell and titanium dioxide is the most widely investigated material. However, the current solar-to-hydrogen efficiency is quite low, due to some intrinsic material limitations such as the bandgap —titanium dioxide absorbs only UV light— and the high density of trap sites, which act as recombination centers. In this work, an overview of recent developments of some promising materials and methods to improve the photoanode performance and thus the PEC efficiency is presented, such as metal and non-metal $TiO_2$ doping and modification of size and morphology (nanostructures). Recently, a novel strategy has been developed, consisting of a new form of $TiO_2$, hydrogenated $TiO_2$ or black titania, which is black in color and exhibits high efficiency for photocatalytic reactions under visible light illumination. This new material is very attractive but not fully understood, in particular the role of hydrogen and nano-morphology must be clarified and optimized. However, in this context, it is useful to try to hydrogenate hierarchical structures.

In this thesis, we focus on hydrogen treated hierarchical nanostructured $TiO_2$ photoanodes, prepared by Pulsed Laser Deposition (PLD) in the presence of a background atmosphere. Different morphologies are obtained as a consequence of the variation of a background gas in the deposition chamber. Post-annealing in air at $500\,°C$ or $650\,°C$ is performed, followed by or

substituted with a thermal treatment in $Ar/H_2$ (97%-3%), aiming to introduce hydrogen and to form the so-called black (or reduced) titania. Scanning Electron Microscopy (SEM), Raman and UV/VIS/NIR spectroscopy are employed as characterization techniques, while the photoelectrochemical performances are investigated in collaboration with the Laboratory of Catalysis and Catalytic Process (LCCP), by monitoring the photocurrent produced under solar illumination in a three-electrode cell. A correlation between structural, morphological, optical properties and PEC behaviour is found. The best performances are associated with the sample prepared at $5\,Pa$ of $Ar/O_2$ and annealed in air followed by hydrogen treatment at $500\,°C$. However, this work represents only a preliminary and exploratory study. Further developments consist in the understanding of the physical/chemical mechanisms involved in the hydrogenation process at the atomic scale.

# Premessa

Il *solar water splitting* foto-elettrochimico (PEC) rappresenta un metodo ecologico e a basso costo per la produzione di idrogeno a partire da acqua e energia solare. Il foto-anodo, semiconduttore nano-strutturato, è l'elemento fondamentale della cella PEC e il biossido di titanio è il materiale più studiato. Tuttavia, attualmente, l'efficienza di conversione dell'energia solare in idrogeno è ancora piuttosto bassa, a causa di alcune limitazioni intrinseche del materiale, come l'ampio band-gap —$TiO_2$ assorbe solo radiazione UV— e l'alta densità di siti trappola, che agiscono come centri di ricombinazione. In questo lavoro è presentata un'ampia descrizione di alcuni materiali e metodi promettenti per aumentare le prestazioni del foto-anodo e quindi l'efficienza della cella PEC, come il drogaggio di $TiO_2$ con elementi metallici e non metallici e la modificazione delle dimensioni e morfologia del materiale (nanostrutture). Recentemente, una nuova strategia è stata sperimentata, la quale consiste in una nuova forma di $TiO_2$, biossido di titanio idrogenato o *black titania*, che si presenta di colore nero e ha mostrato un'alta efficienza per le reazioni foto-elettrochimiche, indotte da radiazione luminosa nel visibile. Questo nuovo materiale attrae moltissimo ma non è completamente compreso, in particolare il ruolo dell'idrogeno e della nano-morfologia dovrà essere chiarito e ottimizzato. Tuttavia, in questo contesto, appare utile provare a idrogenare strutture gerarchiche.

In questa tesi, ci siamo focalizzati sullo studio di sistemi gerarchici nanostrutturati a base di $TiO_2$ trattati in idrogeno, preparati mediante Pulsed laser deposition (PLD) in presenza di un'atmosfera di fondo. Diverse mor-

fologie sono state ottenute in base alla miscela di gas utilizzata in camera durante la deposizione. In seguito, trattamenti termici in aria a 500 °C o 650 °C sono stati effettuati, seguiti o sostituiti con trattamenti di idrogenazione in atmosfera di Ar/H$_2$ (97%-3%) con l'obiettivo di introdurre idrogeno e formare la cosiddetta *black titania*. Scanning Electron Microscopy (SEM), spettroscopia Raman e UV/VIS/NIR sono state utilizzate come tecniche di caratterizzazione, mentre le prestazioni foto-elettrochimiche sono state indagate in collaborazione con il Laboratorio di Catalisi e Processi Catalitici, monitorando la foto-corrente prodotta con radiazione luminosa solare in una tipica cella a tre elettrodi. Una correlazione tra le proprietà strutturali, morfologiche e ottiche e il comportamento foto-elettrochimico è stata trovata. Le migliori prestazioni sono state ottenute per il campione depositato a pressione di 5 Pa in Ar/O$_2$ e scaldato prima in aria e poi in Ar/H$_2$ a 500 °C. Tuttavia, questo lavoro rappresenta un preliminare ed esplorativo studio a cui seguir un'approfondita ricerca con l'obiettivo di comprendere meccanismo fisico/chimico alla base dell'idrogenazione a livello atomico.

# Contents

# List of Figures

# Introduction

With the rapid demographic expansion of the world population and the consequent increasing energy demand, the supply of sustainable and inexpensive energy is one of the top challenges in this century. Even though fossil fuels would be capable of meeting this demand, the increasing concentration of $CO_2$ in the atmosphere, as a result of the combustion of these carbon-based fuels, is predicted to result in unacceptable changes in the Earth's climate. This phenomenon points to the need for carbon-free alternative energy sources.

The renewable solar energy is believed to be a potential solution to solve the faced energy crisis. Although solar energy is an abundant and sustainable form of energy, the large scale distribution of solar energy system is still limited. There are two main limitations. One problem is that it is quite diffuse, requiring large areas of solar collectors to harvest significant amounts of power. Second, in order to obtain continuous and stable power supply during day and night, it requires efficient and cost effective energy storage devices to store the excess energy for later utilization. One of the most attractive means proposed is to store solar energy into the chemical bonding of fuels, such as hydrogen.[1]

Hydrogen is a clean and carbon-free burning fuel with high energy density. Actually, hydrogen can be made by several methods: steam reforming, water electrolysis using hydrocarbons, thermochemical processes, photoelectrolysis of water. However only some of them are pollution-free.[2]

Photoelectrolysis of water (or solar water splitting) is a green and low

1

cost method to produce hydrogen from water dissociation using sunlight. It can be achieved with phoelectrochemical (PEC) cell, which is a promising device to convert solar energy directly to chemical energy, in the form of hydrogen, without $CO_2$ emissions. The PEC water splitting cell typically is composed by two electrodes, a photoanode and a counter electrode, immersed in an electrolyte. What is needed in PEC application are semiconducting materials, as photoanode, that can accomplish the absorption of light, the separation of the photo-generated charge carriers, and the efficient transfer of the carriers to an electrolyte solution to produce hydrogen and oxygen from water. In addition, the semiconducting materials must be highly stable and they must have conduction and valence band energies such that the photo-generated electrons are sufficiently reducing to produce hydrogen, and the holes are sufficiently oxidizing to produce oxygen from water. Finally, they must be inexpensive. Therefore, actually no material or combination of material, that meets these requirements is known.[1]

Since Fujishima and Honda (1972) reported for the first time the photoelectrochemical (PEC) water splitting over a $TiO_2$ photoanode, many other materials have been considered in PEC applications. However $TiO_2$ still remains the most widely investigated photocatalyst in consideration of its high activity, chemical inertness, low cost and non toxicity. Moreover, the photoconversion efficiency of $TiO_2$ is substantially limited by its large band gap energy (3.0 eV for rutile and 3.2 eV for anatase) and usually fast electron-hole recombination due to a high density of trap states. Owing to its large band gap, $TiO_2$ absorbes only a small fraction of solar light, less than 5% of solar energy is emitted as UV radiation and the maximum radiation intensity of the solar spectrum occurs in the visible range around 500 nm. So far, many strategies have been proposed to increase the efficiency and two main research pathways have been followed.

Enormous amount of research efforts have been focused on enhancing the visible light absorption of large band-gap metal oxides, for instance via elemental doping. This strategy basically introduces impurities and/or defects that produce midgap states. Impurities successfully doped into $TiO_2$ include metals, nonmetallic elements such as C, N, S, and I, and many others. Through doping, the $TiO_2$ absorption in the visible has been increased but its overall photocatalytic efficiency remains insufficient to compete with other solar energy harvesting devices.[3][4][5]

2

**Introduction**

On the other hand, it is equally important to improve the morphology and electronic structure of $TiO_2$ for effective separation and transportation of photoexcited charge carriers. Several studies have been devoted to the maximization of the effective surface area. In this contest, nanostructured $TiO_2$ architectures and in particular nanotubes have attracted increasing interest due to their highly ordered structure and the fine control of size.[6] More recently, novel quasi 1-D hierarchical structures received attention for their advantages in combining large surface area, light scattering potential and anisotropic morphology (similarly to nanotubes) to ensure better electron transport [7]. In particular, in the last years the activity of our laboratory, was focused on the development of nanocrystalline tree-like $TiO_2$ hierarchical microstructures prepared by reactive pulsed laser deposition (PLD).

Moreover, recently, a large reduction in the $TiO_2$ band gap has been realized by hydrogenation of anatase $TiO_2$ nanocrystals. This consists of a new form of $TiO_2$, which is black in color (the so-called *black or reduced titania*). In literature, it is reported that annealing $TiO_2$ nanostructures in a reducing gas atmosphere, such as $H_2$, introduces surface disorder or increases the density of oxygen vacancies (donor density) and thereby, enhances the electrical conductivity as well as the visible absorption. In addition to a large absorption in the visible and infrared region, these $TiO_2$ powders exhibit both high efficiency and stability in photocatalytic splitting of water under solar irradiation.[8] However, the physical/chemical mechanisms behind the hydrogenation process are not fully understood and further developments are needed to optimize this system.

Our strategy of increasing the PEC performance is to develop hydrogenated quasi 1D hierarchical $TiO_2$ nanostructures. Hierarchical nanostructured photoanodes with large surface area were prepared by Pulsed Laser Deposition (PLD). This versatile physical deposition technique allows to have a fine control on morphology at the nanometer scale. Instead hydrogen thermal treatments were performed in a furnace at atmospheric pressure, aiming to induce visible band-gap shift and to increase PEC efficiency. The effect of hydrogen treatments on morphology, structural and optical properties was investigated by Scanning Electron Microscopy (SEM), Raman spectroscopy, performed in our laboratory and UV/VIS/NIR spectroscopy, carried out at IIT (The Italian Institute of Technology). On the contrary,

the PEC water splitting behaviour was investigated in collaboration with the Laboratory of Catalysis and Catalytic Process (LCCP) at the Polytechnic of Milan.

This thesis is organized in five chapters, according to the following scheme.

- In **Chapter 1** general properties of oxide photoanodes for solar water splitting application are discussed. First of all, the water splitting mechanism and PEC apparatus are described. Then photoanode materials aspects are introduced, in particular advantages and limitations are underlined. Besides, the main methods to increase photoanode efficiency are described. In the second part only $TiO_2$ photoanode is considered. First, a short introduction of $TiO_2$ properties and structure is given. In the end new nanostructured $TiO_2$ photoanodes are reported, especially hierarchical nanostructured $TiO_2$ and hydrogenated $TiO_2$.

- In **Chapter 2** all experimental methods used in this work are described. It starts with a description of deposition apparatus, Pulsed Laser Deposition (PLD). Then a short description about all the other instruments and characterization methods follows: Scanning Electron Microscopy (SEM), Raman spectroscopy, optical spectrophotometer and photocurrent apparatus.

- In **Chapter 3** all experimental results and discussions regarding sample deposition and characterization are reported. First, the morphological and structural characterization of samples after different deposition condition and hydrogen thermal treatments is shown. Second, optical properties are discussed for different samples after sensitization annealing, in order to evaluate the bandgap shift. Finally the photocurrent measurements are reported.

- In **Chapter 4**, other approches aiming to optimizing $TiO_2$ samples performance are investigated and the preliminary results are reported. The development of these strategies is based on the results discussed in chapter 3. Morphological and structural characterizations and photocurrent tests are performed.

- Finally, in **Chapter 5**, conclusions are summarized and possible outlooks are described.

CHAPTER 1

---

Nanostructured oxide photoanodes for solar water splitting

---

## 1.1 Hydrogen as energy carrier: Solar-hydrogen

The typical resources used to supply the world energy needs, such as coal and oil products, have been largely depleted. Due to this situation and the need for a cleaner environment, interest in alternative and renewable fuels for energy production has increased rapidly around the world.

Hydrogen has been identified as one of potential clean energy carriers, that can be produced from any primary energy source. It's not a primary energy source but can be used to store, transport and provide energy over long distances and in large quantities.

Hydrogen is a colorless, odorless, tasteless and the most abundant element in the universe. It cannot be destroyed unlike hydrocarbons but it simply changes state, for example, from water to hydrogen and back to water during consumption. Hydrogen is also the simplest element, an atom consisting of only one proton and one electron.

Despite its simplicity and abundance, hydrogen does not occur naturally as a gas on the Earth and it is always combined with other elements in water and in many organic compounds, notably the hydrocarbons that make up many of our fuels such as gasoline, natural gas, methanol and propane. Hydrogen bound in water and organic forms accounts for more than 70% of the Earth's surface.

The general enthusiasm for the use of hydrogen as an enviromently friendly fuel has been encouraged by the fact that it produces a high energy yield (the energy content per unit mass is about $120 \, \mathrm{KJ/g}$), it is pollution free and can be easily stored. Infact, the combustion of hydrogen in pure oxygen produces only water ($H_2 + O_2 \rightarrow H_2O$), which neither results in air pollution nor leads to the emission of greenhouse gases. However, if hydrogen is burned in air oxides of nitrogen, $NO_x$ can be formed, known to be the cause of urban smog and acid rain. Nevertheless in comparison to the burning of fossil fuels the amount of these oxides generated by hydrogen combustion is essentially nil.

The energy, stored in the form of hydrogen, can be used to supply the needs of a great variety of industrial activities and aspects of society, from homes to electric utilities to business and industry (Figure 1.1). Currently, most of hydrogen is made by separating it from hydrocarbons by applying heat, a process known as "reforming hydrogen" or by water electrolysis exploiting the electric energy, often produced by carbon-fuels. Both these technologies produce $CO_2$ emissions. Therefore, new methods to generate $H_2$ expecially from renewable and sustainable resources, have been developed. Photoconversion production is a promising option.
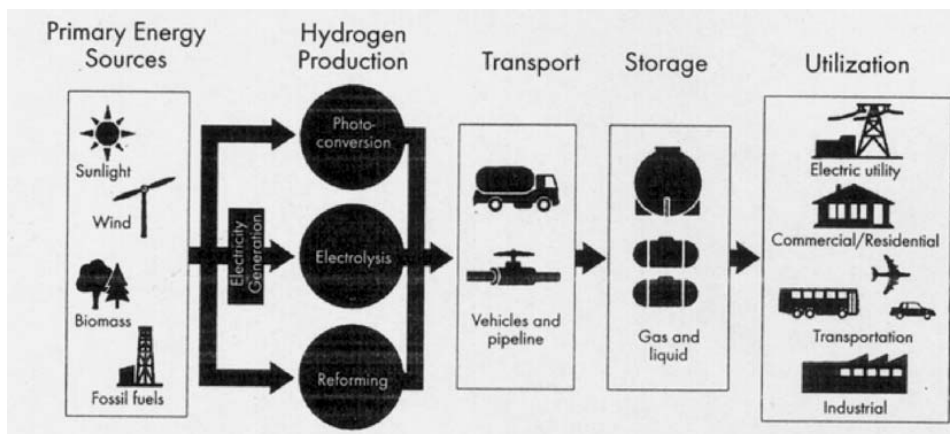


***Figure 1.1:*** *A hydrogen energy system.[2]*

The researchers are exploring the use of renewable resources such as sunlight to produce hydrogen economically.[2] This approch uses semiconductors to absorb sunlight, split water and produce hydrogen. Water splitting using solar energy for hydrogen production is general called Solar-Hydrogen

production. Tipically, solar-hydrogen is obtained by an electrolytic process using solar energy in the photoelectrochemical cell (PEC).[9] The net reaction is:

$$H_2O(liquid/vapor) + solar \quad energy \longrightarrow H_{2(gas)} + 1/2O_{2(gas)}$$
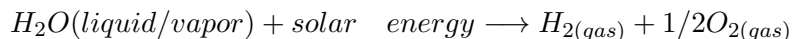
As seen in Figure 1.2, the amount of energy produced by the combustion of hydrogen is considerably greater than that from other fuels. Furthermore, unlike the production of hydrogen from methane, solar-hydrogen offers the dual capacity of hydrogen fuel with nil $CO_2$ emission. Of course, hydrogen is environmentally safe also when it is generated from other types of renewable energy, such as wind, hydroelectric, tidal and geothermal energies, however solar -hydrogen results the most promising method due to the following reasons:

- Solar-hydrogen technology is relatively simple.

- The only raw material for the production of solar-hydrogen is water, which is a renewable resource.

- Large areas of the globe have ready access to solar energy which is the only required energy source for solar-hydrogen generation.

Actually solar-hydrogen technology can not be applied for commercial application because the efficiency is still low. The main limits of this method are related to the materials used as photoanode in the PEC. Fujishima and Honda [10] first reported in 1972 the experiment of water electrolysis using solar-energy as the sole driving force for water decomposition. Since the first reports, there have been many papers published on the impact of different structures and materials on the performance of photo-electrochemical cells (PECs). Consequently, commercial applications for hydrogen generation from solar energy and water will be determined by the progress in materials science and engineering applied to the candidate materials for photo-electrodes.[11]

This chapter concerns the mechanism of the splitting of the water molecule to generate hydrogen and oxygen, the priciples of the photoelectrochemical cell (PEC) and the materials used as photoanode, in particular $TiO_2$ nanostructures. The performance of the cell is discussed in terms of the solar to hydrogen conversion efficiency. The $TiO_2$ properties (charge transport,
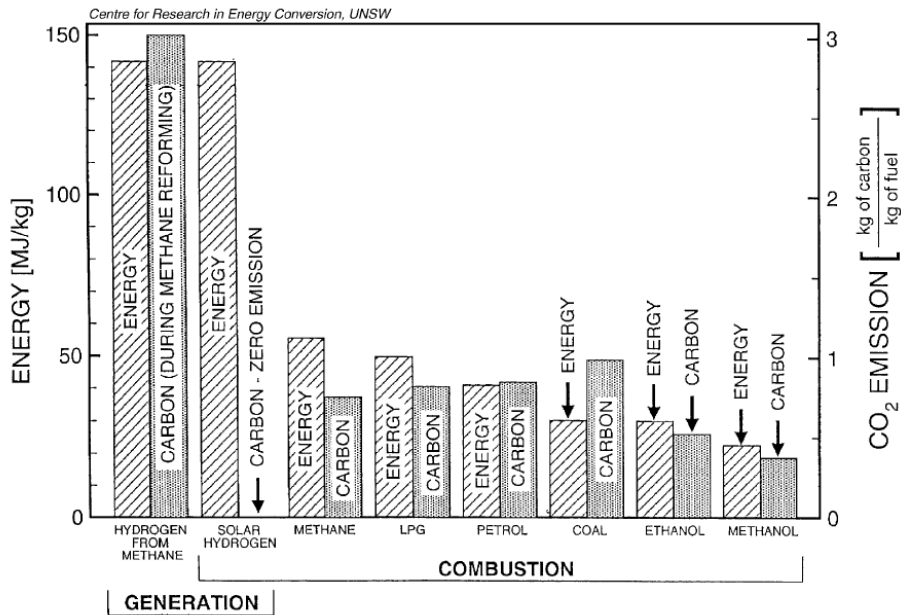
**Figure 1.2:** *Amount of energy produced by combustion of different fuels and related carbon emissions.[9]*

crystallinity, surface area) are outlined. Finally, the modification of TiO$_2$ in order to achieve desidered performance parameters is discussed, such as doping, modification of morphology and hydrogenation.

## 1.2 Photoelectrochemical (PEC) cell.

### 1.2.1 Principles and electrode reactions

In general, a PEC cell consists of a working photoelectrode and a counter electrode, immersed in an electrolyte. In the most simple terms, the principle of photoelectrochemical water decomposition is based on the conversion of light energy into electricity within a cell involving two electrodes, of which at least one is made of a semiconductor exposed to light and able to absorb the light. This electricity is then used for the decomposition of water. In theory there are three different arrangement of photo-electrode in the PEC[11]:

- photoanode made of n-type semiconductor and the cathode made of a metal;

8

- photoanode made of n-type semiconductor and photocathode made of p-type semiconductor;

- photo-cathode made of p-type semiconductor and anode made of a metal.

The following section will be limited to the first photocell option, although the performance principles are the same for all three cases.
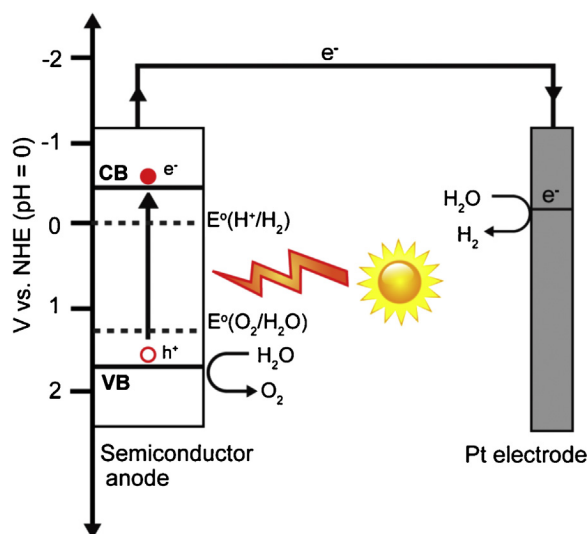


**Figure 1.3:** *Photoelectrochemical water splitting cell based on n-type semiconductor TiO$_2$ photoanode.[12]*

Fujishima and Honda in 1972 first reported the concept and performance of a PEC with a n-type TiO$_2$ as a photoanode and platinum as a cathode.[10] When the surface of the TiO$_2$ electrode was irradiated with UV light, as result of a water oxidation reaction, oxygen evolution occured at the TiO$_2$ electrode. On the contrary, reduction led to hydrogen evolution at the platinum electrode. A schematic rapresentation of photoelectrochemical cell used by Fujishima and Honda is shown in Figure 1.3.

An essential component of the device for hydrogen generation is the photoanode, which is a semiconductor material. A semiconductor material has a band structure and the energy difference between the valence band and the conduction band is known as the "band gap". When a semiconductor is irradiated with light with photon energy larger than or equal to its band gap the electrons in valence band are excited to the conduction band,

while the holes are left in the valence band. This, therefore, creates the negative-electron ($e^-$) and positive-hole ($h^+$) pairs. This stage is referred to as the semiconductor "photo-excited" state. After photoexcitation, the excited electrons and holes separate and migrate to the surface of photo-catalyst. When the semiconductor is contacted with the electrolyte, the charge transfer occurs at interface between semiconductor and electrolyte. The photoexcited electrons transfer to the counter electrode through the external circuit and reduce water to generate $H_2$ ( hydrogen ions migrate to the cathode through the internal circuit via the electrolyte ), while holes diffuse to the surface of the semiconductor and oxide water to form $O_2$.

The net water decomposition reaction is:

$$H_2O_{(liquid)} + h\nu \longrightarrow 1/2O_{2(gas)} + H_{2(gas)}$$
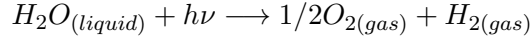
where $h$ is Planck's constant and $\nu$ is the frequency of light.
The reaction equations on each electrode (at pH=0) are shown in the following:

$$Photoanode: \qquad 2h^+ + H_2O_{(aq)} \longrightarrow 2H^+ + 1/2O_{2(gas)} \qquad E^\circ_{ox} = -1.23V$$

$$Cathode: \qquad 2H^+_{(aq)} + 2e^- \longrightarrow H_{2(gas)} \qquad E^\circ_{red} = 0V$$
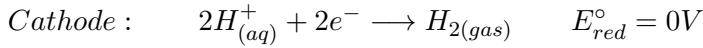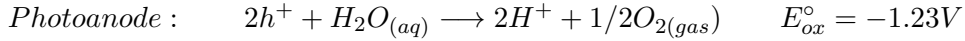
The free energy change for the conversion of one molecule of $H_2O$ to $H_2$ and $1/2$ $O_2$ under standard conditions is:

$$\Delta G = 237.2 kJ/mol$$

according to the Nernst equation corresponds to:

$$\Delta E^\circ = 1.23V$$

per electron transferred.

This means that to use a semiconductor and drive this reaction with light, the semiconductor must absorb radiant light with photon energies of >1.23 eV (equal to wavelengths of ~1000 nm and shorter) and convert the energy into $H_2$ and $O_2$. In the ideal case, a single semiconductor material, having a band gap energy ($E_g$) large enough to split water, and having a
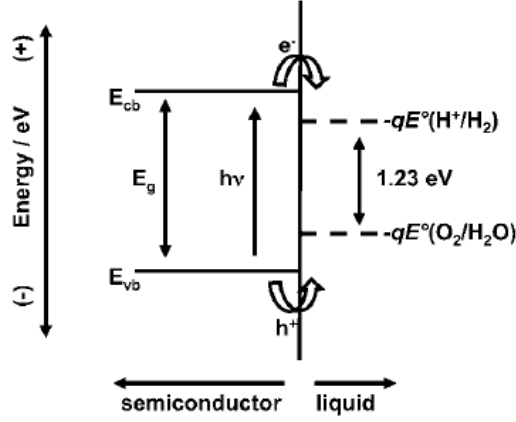
***Figure 1.4:*** *Ideal semiconductor material for splitting water[13]*

conduction band-edge energy ($E_{cb}$) and valence band-edge energy ($E_{vb}$) that straddles the electrochemical potentials $E°(H^+/H_2)$ and $E°(O_2/H_2O)$, can drive the hydrogen evolution reaction and oxygen evolution reaction using electrons/holes generated under illumination without using any PEC (Figure 1.4). Therefore theoretically the minimun energy required for PEC water splitting is 1.23 eV. However, in practice photons with energy larger than theoretical limit is needed due to the energy loss during PEC water splitting. The energy loss include:

- the electron-hole recombination,

- the voltage losses at the contacts,

- the potential loss due to the electrode and contact resistance.

The estimated energy loss is around 0.8 eV, accordingly, the practical voltage required for PEC water splitting is $\sim$ 2 eV.

As it will seen in section 1.3, many materials has suitable band position to achieve non-biased water electrolysis. However, in most cases, an exernal potential (bias potential) is needed to be applied even if the bandgap of the photoelectrode is larger than 2 eV. This phenomenon can be explained considering the band energy diagram of PEC components.

The band structures of both electrodes, involving the photoanode of an n-type semiconductor and metallic cathode, at different stages in the formation of the electrochemical chain of the PEC, are shown schematically
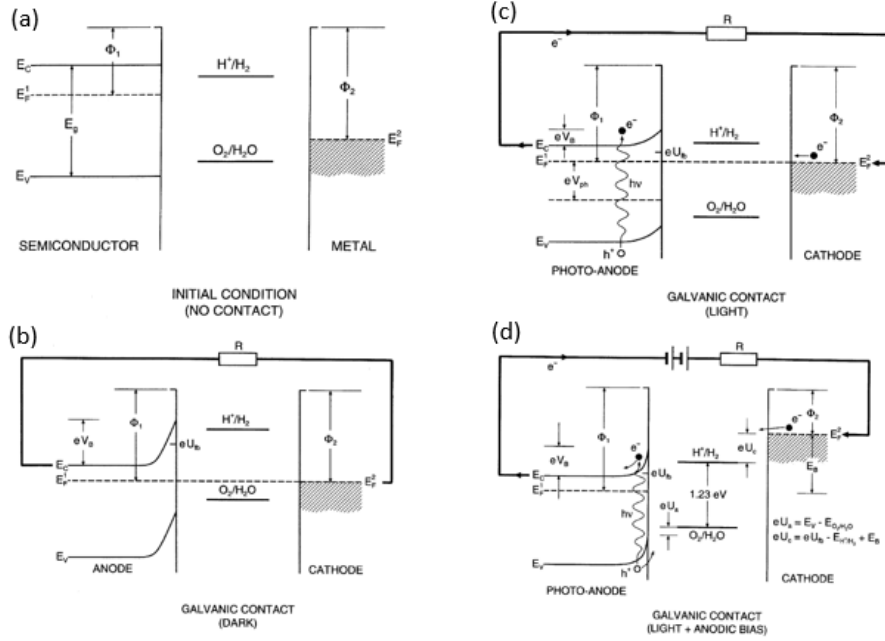
***Figure 1.5:*** *Energy diagram of PEC components: before galvanic contact (a), after galvanic contact in dark (b), after galvanic contact under light irradiation (c), with externally applied voltage, voltage-bias (d)[11]*

in Figure 1.5. This figure shows the band structure, illustrating various energy quantities, such as work function, band levels of the electrodes before and after the connection is established (in comparison with the potentials corresponding to the $H^+ = H_2$ and $O_2 = H_2O$ redox couples) and band bending.[11] Figure 1.5 (a) shows the energy diagram before the galvanic contact is made between the two electrodes. As seen in Figure 1.5 (b), the contact between the two electrodes (in the absence of light) results in electronic charge transfer from the solid of lower work function (semiconductor) to the solid of higher work function (metal) until the work functions of both electrodes assume the same value. This charge transfer results in a change in the semiconductor surface electrical potential, leading to band bending. This energy relation is not favourable for water decomposition because the $H^+ = H_2$ energy level is above the Fermi energy level of the cathode. As seen in Figure 1.5 (c), the application of light results in the lowering of the surface potential of the photo-anode and the lowering of the $H^+ = H_2$ potential. However, the latter still is above the $E_F$ level of the cathode.

## 1.2 Photoelectrochemical (PEC) cell.

Consequently, Figure 1.5 (d) shows that the application of an anodic bias is required to elevate the cathode $E_F$ level above the $H^+ = H_2$ energy level, thus making the process of water decomposition possible.[11]

In general, water splitting is very complex mechanism and involves several processes, most of which are accompanied by charge transfer. A detailed description of all reactions that take place in a PEC is reported in the following Table 1.1.

Table 1.1: The concept of solar-hydrogen generation in terms of elementary reactions.[9]

| Reaction | Process description |
|---|---|
| $H_2O_{(l)} \rightarrow H_2O^*_{(ads)}$ | Adsorption of water molecules on surface active centres resulting in the formation of catalytically active complex. |
| $H_2O^*_{ads} \rightarrow OH^-_{(ads)} + H^*_{(ads)}$ | Dissociation of water molecules on the surface of photo-anode. |
| $h\nu \rightarrow \{e' + h^\bullet\}_s$ | Light-induced formation of electron-hole pair through ionization over band gap of a semiconducting photo-electrode near the surface (s). |
| $\{e' + h^\bullet\}_s \rightarrow h^\bullet_s + e'_b$ | Separation of light-induced formed near the surface, leading to transfer of electron holes toward the surface (s) and electrons toward the bulk (b). |
| $OH^-_{(ads)} + h^\bullet \rightarrow O^-_{(ads)} + H^+_{ads}$ | Reaction of OH radicals with electron holes leading to the formation of O chemisorbed species and hydrogen ions. |
| $O^-_{(ads)} + h^\bullet \rightarrow O^*_{(ads)}$ | Reaction between the surface oxygen species and electron holes resulting in the formation of atomic oxygen radicals. |
| $O^*_{(ads)} \rightarrow O^*_{(gas)} \rightarrow 1/2O_{2(gas)}$ | Desorption of oxygen radicals and their subsequent association leading to the formation of gaseous oxygen. |
| $H^+_{(ads)} + H_2O \rightarrow \{H_3O^+\}_a$ | Formation of hydronium ions in the vicinity of anode. |
| $(e'_b)_a \rightarrow (e'_s)_c$ | Transfer of electrons from the bulk (b) of photo-anode (a) to the surface (s) of the cathode (c) over exernal circuit. |
| $\{H_3O^+\}_a \rightarrow \{H_3O^+\}_e$ | Migration of hydronium ions from the vicinity of photoanode (a) to the vicinity of cathode (c). |
| $\{H_3O^+\}_e \rightarrow \{H^+_{(ads)}\}_c + H_2O$ | Adsorption of hydrogen ions on the surface of the cathode (c). |
| $\{H^+_{(ads)}\}_c + e' \rightarrow \{H^*_{(ads)}\}_c$ | Reaction between adsorbed hydrogen ions and electrons leading the formation of hydrogen radicals in the vicinity of cathode(c). |
| $H^*_{(ads)} \rightarrow (H^*_l)_v$ | Transfer of hydrogen radicals from the adsorbed layer (ads) to the electrolyte (l) inthe vicinity of the cathode (c). |
| $2(H^*_l)_c \rightarrow H_{2(gas)}$ | Association of hydrogen radicals leading to the formation of gaseous molecules (gas). |

## 1.3 Materials aspects of the photoanode

As described in the previous section the photoanode is a semiconductor that absorbs light and generates electron-hole pairs. To design an efficient solar water splitting cell, it is critical to understand the fundamental device physics of semiconductors, the thermodynamic and kinetic parameters of semiconductor-liquid contacts, and the function of surface electrocatalysts.[14] However, this section aims to present a concise view of photoelectrochemical processes that occur in the PEC and the main properties of a semiconductor photoanode.

As already mentioned, several approaches to photoelectrolysis are possible. Here, a n-type semiconductor electrode and a metal electrode configuration is considered. The principal aspects of photoelectrolysis of water to take into account are:

(1) light absorption and charge carrier generation in the semiconductor;

(2) charge separation and transport in the semiconductor and at semiconductor-liquid interface;

(3) charge carrier extraction and electrochemical product formation.

Suitable photo-electrode materials for efficient solar hydrogen generation have to fulfil the following requirements:

- spectral sensivity;

- proper positioning of valence and conduction bands;

- stability;

- large surface area;

- low recombination rate (crystallinity, low defectivity);

- good and preferential electron transport;

- low cost.

**Spectral sensivity: band gap**

The spectral region in which the semiconductor absorbs light is determined by the bandgap of the material. The minimum bandgap is determined by the energy required to split water (1.23 eV) plus the thermodynamic losses (about 0.4 eV) and the overpotentials that are required at various points in the system to ensure sufficiently fast reaction kinetics (about 0.4 eV). As a result, the bandgap should be around 2 eV, which corresponds to an absorption onset at 600 nm. The maximum value of the bandgap is determined by the solar spectrum shown in Figure 1.6. Below 400 nm the intensity of sunlight drops rapidly, imposing an upper limit of around 3 eV on the bandgap. Hence, the optimum value of the bandgap should be somewhere between 2 and 3 eV, which is within the visible range of the solar spectrum. However, actually the most used semiconductor materials have a bandgap higher that 3 eV.
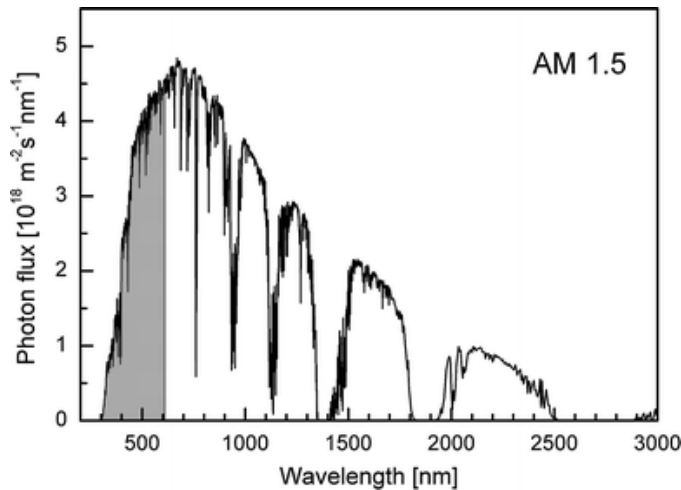


**Figure 1.6:** *Intensity of sunlight versus wavelength for AM1.5 conditions. The grey area represents the part of the spectrum that can be absorbed by an hypothetically ideal bandgap of 2.03 eV.*

**Proper positioning of valence and conduction bands**

The two fundamental reactions of water splitting, $O_2$ formation at n-type semiconductor and $H_2$ formation at the counter electrode, can only occur if the bandgap is higher than 1.23 eV, the conduction band being above (negative) of $E_{red}(H_2/H^+)$ and the valence band below (positive) $E_{ox}(OH/O_2)$.

## 1.3 Materials aspects of the photoanode

Figure 1.7 shows the band-edge positions of various semiconductors, along with the reduction and oxidation potentials of water, at pH=14. The figure indicates that most non-oxide semiconductors are able to reduce, but not oxidize water. Conversely, most oxide semiconductors are able to oxidize, but not reduce water. Materials as $KTaO_3$, $SrTiO_3$, $TiO_2$ are in principle able to both oxide and reduce water. However, as described in the previous section, in the most cases, an externally applied voltage is necessary to assist the reduction reaction (also for $TiO_2$, when potential losses are considered).
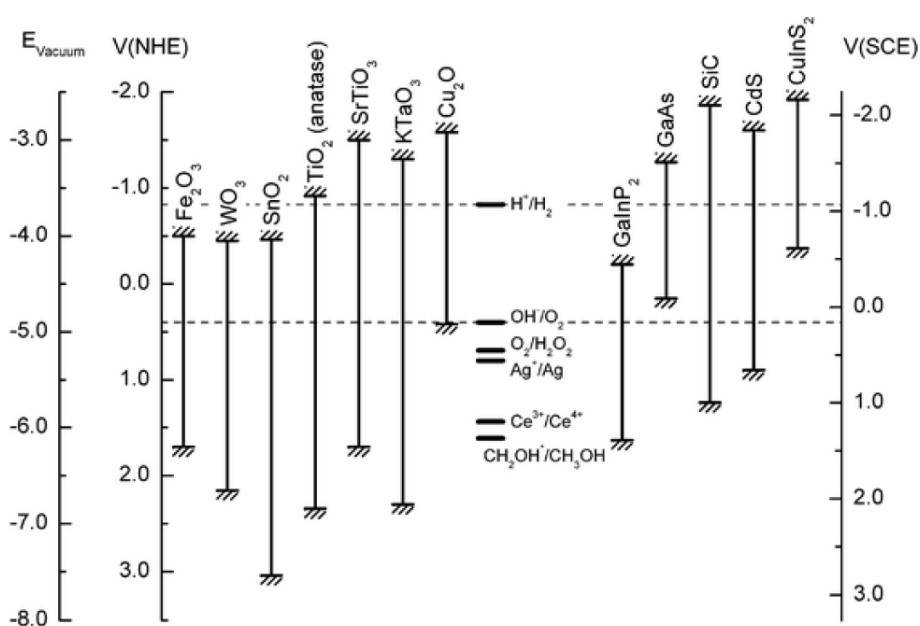


**Figure 1.7:** *Energy band positions for various semiconductors at pH 14.[15]*

### Stability

It is clear from the cell design that only semiconductor electrodes which are chemically stable can be used. The photoelectrode must be resistant to reactions at solid/liquid interface, resulting in degradation of its properties.[14] These reactions include:

- electrochemical corrosion;

- photocorrosion;

- dissolution.

There are several oxide semiconductors which show sufficient stability. However, only a few oxides meet the energetic conditions discussed above: the general trend is that wide-bandgap metal oxide semiconductors are stable against photocorrosion, while small bandgap semiconductors are not. This is in obvious conflict with the requirement of visible-light absorption. $TiO_2$, $SnO_2$ and $WO_3$ show excellent stability over a wide range of pH values and applied potentials, while ZnO always decomposes in aqueous environments upon illumination. $Fe_2O_3$ rapresents an intermediate case, for which the stability appears to depend on the presence of dopants, pH, and oxygen stoichiometry. [16]

## Surface area

Surface properties such as particle size, surface area, surface structure, and active reaction sites, which are mainly related to the morphology of the materials, are also very important.[17] Large surface area is desidered in order to increase light harvesting and available surface active sites, where redox reactions occur. In this view, nanostructured semiconductor photoelectrodes, such as nanoparticles, nanorods and hierarchical structures have attracted great interest. In literature there are various examples of nanostructures, some of them are reported in section 1.4.3.

## Charge transport and low recombination

The fourth requirement, that of efficient charge transport, is easily fulfilled by some materials, while in others it is the main cause of poor overall conversion efficiency. The intrinsic electron and hole mobilities are determined by the electronic structure of the material. The conduction and valence bands of the most (but not all) metal oxides are primarily composed of metal 3d orbitals and oxygen 2p orbitals, respectively. Hence, extensive overlap of the metal 3d orbitals will lead to high electron mobilities, while the amount of overlap between the O-2p orbitals determines the hole mobility. While orbital overlap arguments may provide some initial guidelines for evaluating the charge transport properties of a material, extrinsic factors such as the presence of defects often play a much more important role. Shallow donors or acceptors enhance the conductivity of a semiconductor, whereas defects with deeper lying energy levels usually act as recombination centers. The

fast recombination of electron/hole reduces the photonic efficiency and represents the major drawback of photocatalytic application. Charge separation and transfer of photogenerated electrons and holes are strongly affected by the crystal structural features of the materials, namely, crystallinity, defects, and any crystal structure distortion. Due to the requirement of large surface area the materials emplyed are nanocrystalline, characterized by a lot of defects, grain boundaries and surface states, that can act as reconbination center.

The recombination of electrons and holes can be prevented by the presence of an electric field close to the surface of the semiconductor. This field, indicated by a bending of the energy bands in Figure 1.8, is formed during the formation of a Schottky-type contact between the semiconductor and the aqueous electrolyte. During the formation of the Schottky contact, free electrons from the bulk are trapped into surface states at the semiconductor/electrolyte interface. This sheet of negative charge is compensated by the remaining positive charges in the bulk.[15]
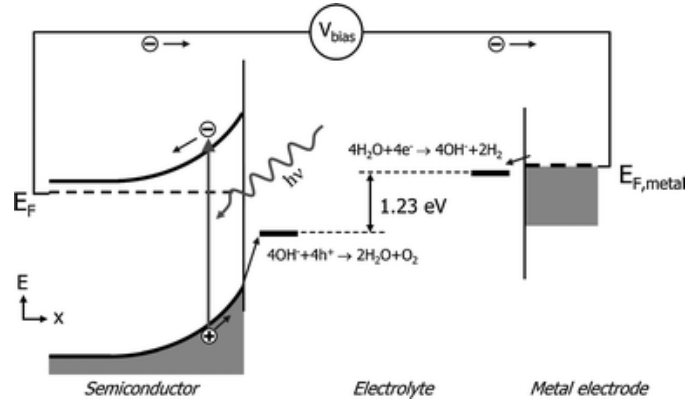


**Figure 1.8:** *Energy diagram of a PEC cell for the photo-electrolysis of water.[15]*

### Anodic and cathodic overpotentials

The last requirement implies that hole transfer across the n-type semiconductor/electrolyte interface should be sufficiently fast in order to compete with the anodic decomposition reaction. Furthermore, hole transfer should also be fast enough to avoid the accumulation of holes at the surface, as this would lead to a decrease of the electric field and a concomitant increase in

electron-hole recombination. To improve the kinetics of hole transfer, the anodic and cathodic overpotentials must be low.

### 1.3.1 Solar-to-hydrogen efficiency

The most important property of a semiconductor photoelectrode is the photoconversion efficiency for water splitting, which is defined as the ratio of the chemical potential energy stored in the form of hydrogen molecules to the incident radiative energy. The benchmark efficiency is 10%, which is generally considered to be required for commercial implementation.

There are two methods to calculate the efficiency of photocatalytic hydrogen generation: direct measurement of the hydrogen gas evolved or indirect photocurrent measurement based on the electrons transferred from the semiconductor to water within a certain time period under light irradiation. Most measurements of the photoconversion efficiency are performed under illumination by artificial light sources. This is convenient because artificial sources are stationary, and their intensity is essentially constant with time, while the spectrum and intensity of real solar radiation reaching the ground depends on the time of day, atmospheric conditions such as cloud cover, water vapour content and ozone column. A standard solar spectrum, usually AM 1.5 (air mass) spectrum, must be used to compare the photoconversion effiencies of different material. [18]

Assuming that all the current that flows through the outer circuit corresponds to the water splitting reaction, the overall solar-to-hydrogen conversion efficiency of the device is given by:

$$\eta_{STH} = \frac{j(V_{redox} - V_S)}{P_{light}} \tag{1.1}$$

Here, j is the photo-current density ($A/m^2$), $P_{light}$ is the incident light intensity in $Wm^{-2}$, $V_{redox}$ is the potential required for water splitting (1.23 eV), and $V_s$ is the difference between the bias voltage, which can be added in series with the to electrods in order to assist the water splitting reaction, and the open circuit voltage under illumination ($V_S = V_{bias} - V_{OC,light}$).[19]

In the case of direct measure of H$_2$ evoluted, the solar-to-hydrogen efficiency is given by:

$$\eta_{STH} = \frac{\phi_{H_2} G^0_{f,H_2}}{P_{light}} \tag{1.2}$$

where $\phi_{H_2}$ is rate of $H_2$ evolution at the illuminated area $(\text{mol/s}/m^2)$ and $G^0_{f,H_2}$ is the Gibbs free energy of formation of hydrogen (237 kJ/mol) and $P_{light}$ is the incident light intensity.[19]

Moreover, when trying to identify performance-limiting factors in PEC photoelectrodes, another important parameter is the quantum efficiency as a function of wavelength. The definition of the external quantum efficiency is the fraction of the incident photons that is converted to electrons that can be measured by the outer circuit. This is the IPCE (incident photon-to-current conversion efficiency), which is given by

$$IPCE(\lambda) = \frac{hc}{e}\left(\frac{j_{photo}(\lambda)}{\lambda P(\lambda)}\right) \tag{1.3}$$

Where $h$ is Plack's constant, $c$ is light velocity, $e$ is electron's charge, $j_{photo}$ is photogenerated current, $\lambda$ is the wavelength and $P(\lambda)$ is the incident light intensity.

An IPCE of 100% corresponds to the generation of one photoelectron for each incident photon. Moreover, IPCE values are always below 100%. There are two fundamental limits to the photoconversion efficiency, which depend on the band-gap of the semiconductor and on the spectrum of the incident radiation. First of all, as seen in the previous section the energy gap of the semiconductor must be higher than the potential required to water splitting (1.23 V) plus the losses, which have been estimeted to be at least 0.8 V, corresponding to a limiting band-gap wavelength of around 600 nm. On the other hand, below 400 nm the intensity of sunlight drops rapidly (see Figure 1.6).

## 1.4 Materials and methods to improve PEC efficiency

### 1.4.1 Introduction

As already discussed, the photocatalytic generation of hydrogen is a very complex process, that consists of many steps. They include light absorption of the semiconductor photocatalyst, generation of excited charges (electrons and holes), recombination of the excited charges, separation of excited charges, migration of the charges and transfer of excited charges to water or other molecules. All of these processes, summarized in Figure 1.9, affect the

final generation of hydrogen from the semiconductor photocatalyst system.
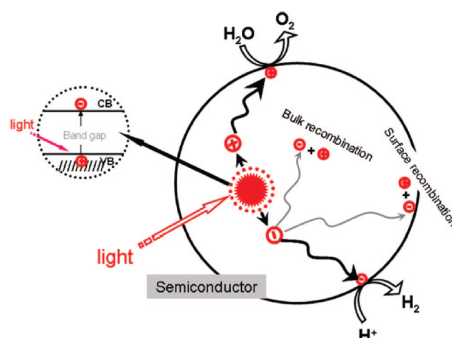


***Figure 1.9:*** *Processes in photocatalytic water splitting.[17]*

The total amount of hydrogen generated is mainly determined by the amount of excited electrons in the water/photocatalyst interface. Consequently, any process that generates excited electrons should be considered to act in a possible way to improve the efficiency. From this point of view, the semiconductor photocatalyst should first have a low band gap to absorb as much light as possible in the visible range, where the intensity of sunlight reaches the maximun value, and reflection or scattering of light by the photocatalyst should be minimized. Second, using the absorbed photons, the semiconductor photocatalyst should have a high efficiency in generating excited charges, any other processes that consume excited electrons (surface and bulk recombination) should be avoided. Therefore efficient charge separation and fast charge transport, avoiding any bulk/surface charge recombination, are fundamentally important for photocatalytic hydrogen generation through water splitting.[17]

A wide range of semiconducting materials have been developed as photocatalysts. $TiO_2$ is the first reported, but also ZnO, $Fe_2O_3$, $WO_3$, metal nitrides, metal chalcogenides, such as CdS and CdSe have been studied. However each semiconductor electrode material has its limitations, that decrease the efficiency of water splitting. For example, $TiO_2$ and ZnO absorb UV radiation due to their large energy gap. They absorb only a small fraction of the solar light (less than 5% of solar energy is emitted as UV radiation). A quite narrow band gap oxides, such as $WO_3$, CdS and CdSe have also limitations. Relatively positive conduction band of $WO_3$ proved dissatisfactory for hydrogen production, while CdS and CdSe are not stable

in oxidative environment and they suffer from photocorrosion.

Taking into consideration the basic mechanisms and processes of photo-catalytic water splitting, there are two main approches to develop a suitable high-efficiency semiconductor:

(1) Approches to modifying the electron band structure for visible light harvesting: doping.

(2) Approches for efficient photogenerated charge separation and transport: modification of size and morphology.

### 1.4.2 Metal and Nonmetal doping

**Metal-Ion doping**

One of the most effective ways to develop visible-light driven photocatalysts is to create impurity levels in the forbidden band through metal ion doping. This makes the wide band gap photocatalysts active in the visible-light region. Over the past decades, there have been numerous reports on the modification of wide band gap photocatalysts using metal ion doping to make them visible-light active. These include doped $TiO_2$, doped $WO_3$, doped CdS and doped ZnS, among others.[17]

Figure 1.10 depicts the sketch of visible-light-driven photocatalysts by metal ion doping to create active photocatalysts with wide band gaps. In the forbidden band, either a donor level above the original valence band or an acceptor level below the original conduction band is created to make the photocatalysts respond to visible light.

Doped-$TiO_2$ is one of the most studied material as photoanode. Until now, many different metal ions have been doped into $TiO_2$ to improve the visible-light absorption and photocatalytic activities, such as V, Ni, Cr, Mo, Fe, Sn, Mn, and so on. In particular, the electronic structures of $TiO_2$ compounds doped with the 3d transition metals (V, Cr, Mn, Fe, Co, and Ni) were analyzed by Umebayashi et al. using ab initio band calculations (Figure 1.11)[4]. They found that the 3d metal doping created an occupied level either in the band gap or in valence band (VB) due to the $t_{2g}$ state of the dopant. The charge transfer transition between this $t_{2g}$ level and the conduction band (CB) (or VB) of $TiO_2$ contributed to the photoexcitation under visible light.
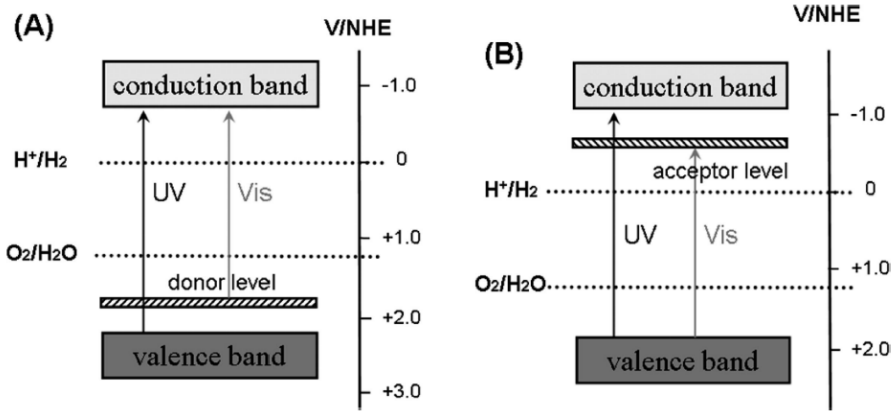
**Figure 1.10:** *Donor level (A) and acceptor level (B) formed by metal ion doping.[17]*
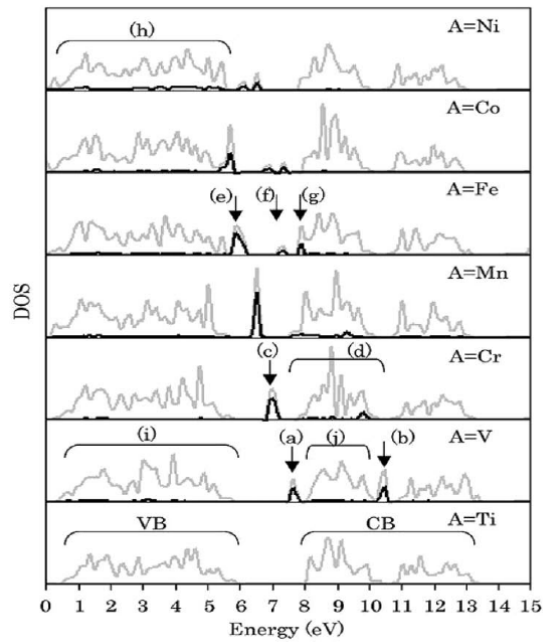


**Figure 1.11:** *Density of states (DOS) of the metal-doped $TiO_2(Ti_{1-x}A_xO_2$: A = V, Cr, Mn, Fe, Co, or Ni). Gray solid lines: total DOS. Black solid lines: dopants DOS. The states are labeled a-j.[4]*

## 1.4 Materials and methods to improve PEC efficiency

Anpo and co-workers prepared various metal-ion-doped $TiO_2$ materials using advanced ion implantation. They found that the absorption band of metal-ion-implanted $TiO_2$ (the metals used were V, Cr, Mn, Fe, and Ni) shifted smoothly toward the visible-light region. The extent of the red shift depended on the amount and type of metal ions implanted.[3]

Choi et al.[20] found that doping of metal ions could expand the photo-response of $TiO_2$ into visible spectrum. As metal ions are incorporated into the $TiO_2$ lattice, impurity energy levels in the band gap of $TiO_2$ are formed. Furthermore, electron (hole) transfer between metal ions and $TiO_2$ can alter electron-hole recombination or photocatalytic reactions, carrier transferring is as important as carrier trapping. Only if the trapped electron and hole are transferred to the surface, photocatalytic reactions can occur. Therefore, metal ions should be doped near the surface of $TiO_2$ particles for a better charge transferring. In case of deep doping, metal ions likely behave as recombination centers, since electron/hole transferring to the interface is more difficult. Furthermore, there exists an optimum concentration of doped metal ion, above which the photocatalytic activity decreases due to the increase in recombination.

In literature examples of other doped oxides found , such as $WO_3$. Hameed et al.[21] studied the effect of different transition metals (Fe, Co, Ni, Cu and Zn), at different concentrations, on the photocatalytic activity of $WO_3$ for splitting of water into hydrogen and oxygen, under UV laser irradiation. $WO_3$ is a yellow solid semiconductor with a band gap of 2.8 eV. The band edge position of pure $WO_3$, conduction (+0.4 V) and valence bands (+3.1 V) at pH = 0, are suitable to oxidize water but does not support the formation of $H_2$ gas. The doped transition metals (TM) in ionic form bind with surface oxygen to form "patches" of doped metal oxides at the surface. These "patches" act as electron capture and transfer sites under bandgap excitation. After $WO_3$ absorbs the photons and generates the electron-hole pair, the photoexcited electron is transferred to the conduction band of the doped metal oxide. Therefore, the valence band of $WO_3$ is used for the oxidation of water while the reduction of $H^+$ ions, produced by the photocatalytic oxidation of the water, occurs at the doped metal oxide. This study revealed that among transition metals, nickel doping gave maximum hydrogen production.

The last example of metal-ion doping is about the visible-light active CdS

photoanode. Some visible-light active photocatalysts were also modified by metal ion doping with aim of narrowing their band gaps in order to utilize visible light in further longer-wavelenght regions to produce more efficient photocatalytic water splitting. Reber and Meier modified CdS photocalyst by doping it with $Ag^+$ in order to extend the spectral response up to 620 nm. A significant enhancement in the photocatalytic activity for hydrogen evolution was obtained with CdS powders containing 0.77% $Ag^+$.[5]

**Nonmetal-Ion Doping**

Nonmetal ion doping is another approach used to modify UV-light-active photocatalysts. It has been widely used to narrow the band gap and improve the visible-light-driven photocatalytic activity. Unlike metal-ion dopants, non metal ion dopants are less likely to form donor levels in the forbidden band but instead shift the valence band edge upward. This results in a narrowing of band gap as indicated in Figure 1.12.
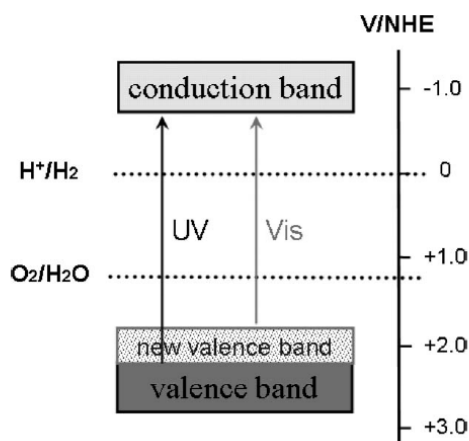


**Figure 1.12:** *New valence band formation by doping of nonmetal ions.[17]*

Various non-metal ions (such as C, N, S, etc.) were used to dope $TiO_2$, and the products were studied for their optical and photocatalytic properties. Chen and co-workers [22] used X-ray photoelectron spectroscopy (XPS) to show that additional electronic states exist above the valence band edge of pure $TiO_2$, for C-, N-, and S-doped $TiO_2$ (Figure 1.13 A). This additional electron density of states can explain the red shifted absorption of these potential photocatalysts, as observed in the "shoulder" and "tail-like" features in the UV-VIS spectra (Figure 1.13B).
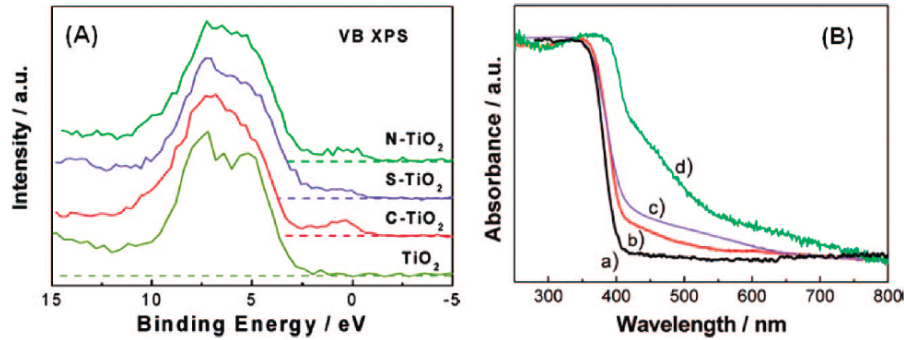
***Figure 1.13:*** *VB XPS spectra (A) and diffuse reflectance spectra (B) of (a) pure TiO2, (b) C-TiO2, (c) S-TiO2, and (d) N-TiO2.[22]*

Asahi et al.[23]studied the substitutional doping of C, N, F, P, and S for O in anatase $TiO_2$. They calculated the electronic band structure of anatase $TiO_2$ with different substitutional dopants and they found that the substitution of N for O, which leads to the mixing of the 2p states of N with the 2p of O, was the most effective. It led to the band gap narrowing by shifting the valence band edge upward, which in return resulted in N-doped $TiO_2$ having a much higher photocatalytic activity than pure $TiO_2$ in the visible-light region. Up until now, N-doped $TiO_2$ has been both widely investigated and successfully prepared by many different methods. Similar to the case of N-doped $TiO_2$, N-doping in $Ta_2O_5$ also caused a valence band upward shift to a higher energy level, which narrows the band gap.[24]

The photocatalytic activity of S-doped $TiO_2$ has also been studied in depth. Using different synthetic methods, anionic sulfur can be doped into $TiO_2$ to replace the lattice oxygen or as an cation to replace the Ti ion. It was found that S-doped $TiO_2$ showed different photocatalytic activities under visible light. In Nishijima and co-workers study of S-doped $TiO_2$, a higher activity level for hydrogen evolution than for N-doped $TiO_2$ photocatalysts under visible light was reported.[25]

Kahn et al. prepared C-doped $TiO_2$ with main rutile structure by pyrolyzing Ti metal in a natural gas flame. The C-doped $TiO_2$ possessed lower band gap energy and displayed a much higher photoactivity in water splitting than pure $TiO_2$ with the mixed phase of anatase and rutile. [26]

To further enhance the visible-light activity, another strategy reported in literature is codoping. Nonmetal codoping of $TiO_2$ such as F/B-codoping[27],

F/N-codoping[28], C/N-codoping [29] and others have been studied. Results suggested that non metal-codoped $TiO_2$ compounds had significant visible photocatalytic activities due to the synergetic effect of two different elements.

### 1.4.3 Modification of size and morphology

To obtain high efficiency, a photoelectrode film must be thick enough to absorb more light, however photogenerated carriers deep within the photoelectrode must be able to reach the surface, where they can be collected and redox reaction occurs. Therefore crystallinity, defects, particle size, surface area, surface structure and in general the morphology are very important parameters in order to obtain high photocalyst efficiency. The morphology of a photoelectrode influence the transfer distance of photoinduced carriers. Consequently, morphology control of photoelectrodes, in particular those with porous structures or nanostructures (such as nanorods, nanotubes, and nanowires), has attracted much attention.

The potential advantages of nanostructured photo-electrodes over conventional semiconductor photo-electrodes are the relatively short transfer distance of carriers and the increase in the surface reaction sites, which lower the recombination probability of carriers and improve PEC performances. It is well-known that particle size is a crucial factor in the dynamics of electron/hole recombination processes, expecially in semiconductor nanomaterials, and that the movement of electrons and holes is primarily governed by the well-known quantum confinement.[22] Generally, a decrease in particle size could be expected to lead to a higher efficiency in photocatalysis. This was because the bulk charge recombination of photogenerated electrons and holes, dominant in the well-crystallized large semiconductor particles, was reduced by decreasing particle size. Reduction in particle size could also lead to a larger surface area and increased the available surface active sites.

Various architectures with nanometer- and micrometersized dimensions have been found to play an important role in achieving fast charge transfer and efficient charge separation for the improvement of photocatalytic activity. One dimensional (1D) nanostructures, such as nanowires, nanotubes, and nanorods/nanoribbons, have all displayed great potential in photocatalysis applications.

Jitputti and co-workers reported that $TiO_2$ nanowires with high crys-

tallinity and surface area could promote higher $H_2$ evolution than commercial $TiO_2$ nanoparticles. It was proposed that the unique 1D structure might facilitate the electron transport for reacting with water molecules adsorbed at the $TiO_2$ surface along the 1D structure.[30] Another example of 1D structure, that have attracted great attention, was titania nanotube. Paulose at al.[6] showed that the highly ordered nanotube arrays are an excellent photoelectrochemical material platform architecture that is both low cost and stable against photocorrosion with no detectable sample degradation over testing periods of several months. Grimes and co-workers demostrated that nanotubular structure gave rise to superior electron lifetime in addition to high surface area.[31]

Two-dimensional (2D) nanostructures such as nanobelts, nanosheets, and nanoplates also favor the transfer of electrons and holes generated inside the crystal to the surface and promote the charge separation, which helps to enhance the photocatalytic activity to some degree. Ultrathin nanosheets of brookite $TiO_2$ displayed high phtocatalytic activity. The atomic scale thickness and large surface area allowed shorter migration time of carriers, suppressed bulk recombination.[17]

Finally, self-assembly of nanoscale building blocks into three dimensional (3D) complex structures is another important research field. Hierarchical structures of photoelectrodes have attracted interest. Tree-like quasi 1D structures characterised by relevant porosity have shown promising results achieving high level of efficiency, up to 8%. These optimal performances were attributed to a balance between available surface area and electron transport/recombination related to the crystallinity and connectivity of the structure.[32]

In Figure 1.14 SEM images of three types of nanostructures of $TiO_2$, nanowires, nanotubes and tree-like quasi 1D structure are reported.

In our laboratory, the latter type of structure are deeply studied for photovoltaic application and water splitting. In this work, hierarchical tree-like $TiO_2$ structures are used as photoanode for water splitting application. Their characteristics and properties will be described in the section 1.5.1.

### 1.4.4   Other methods

Traditional strategies have been developed to enhance solar light absorption (e.g., ion doping, narrow-band-gap semiconductor) and to improve charge
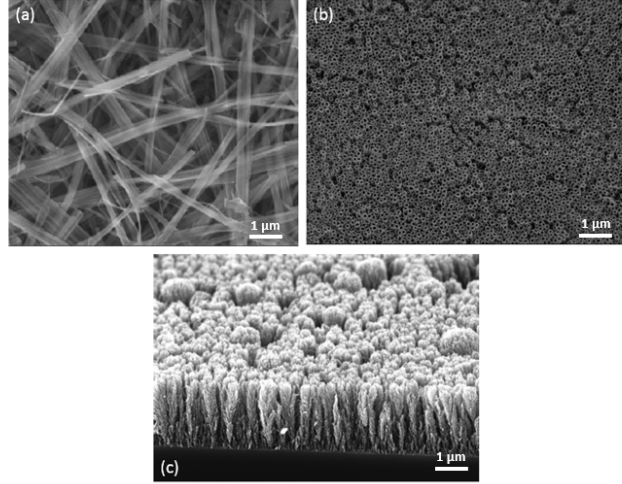
**Figure 1.14:** *TiO$_2$ nanostructures:(a) nanowires[30], (b) nanotube [6], (c) tree-like quasi 1D structure [32]*

separation/transport to prompt surface reaction kinetics (e.g. nanostructure design) for better utilizing solar energy. However, the solar-to-hydrogen efficiency is still limited. Therefore some novel concepts of solar-active nanostructures design have been introduced, which include surface engineering, design of novel nanostructured heterojuctions, and semiconducting photonic crystals.[33] Here some of these new approches are reported.

Mao and his team demonstrated a conceptually new approach to enhancing solar absorption of TiO$_2$ nanocrystals by introducing disorder in the surface layers. The disorder-engineering TiO$_2$ was typically synthesized by the hydrogenation. In the following section 1.5.2 hydrogenated Titanium Dioxide approch is studied in deep.[34] Plasmonic metal/semiconductor nanostructures, characterized by their strong interaction with resonant photons through an excitation of localized surface plasmon resonance (LSPR), have received significant attention. It has been demonstrated that plasmonic metal/semiconductor nanostructures achieved significantly higher rates in various photocatalytic reactions compared to their pure semiconductor counterparts, due to the plasmonic effects of noble metal nanoparticles. The presence of noble metal particles on the surface of the photocatalyst increases the electron-hole pair separation because photogenerated electrons can be captured by the noble metal. Therefore noble metal particles can serve as electron traps. Under light irradiation, the electrons are transferred from

the $TiO_2$ conduction band to the metal, and the holes accumulated in the $TiO_2$ valence band. Hence, photogenerated electrons and holes are efficiently separated. However, the noble metal clusters at a higher concentration may also work as a recombination center.

Chen et al.[35] found that the photocatalytic activity for hydrogen and oxygen production over $Au/TiO_2$ under the irradiation of both UV and visible light was significantly increased. A schematic illustration of Au-loaded $TiO_2$ is reported in Figure 1.15.
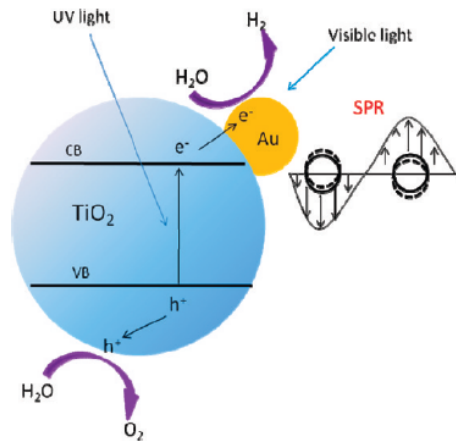


**Figure 1.15:** *Schematic illustration of Au-loaded $TiO_2$ for water splitting by the SPR effect.[35]*

## 1.5 Titanium dioxide.

Since Fujishima and Honda (1972) reported for the first time the photoelectrochemical (PEC) water splitting into $H_2$ and $O_2$ over $TiO_2$ anode, a lot of investigation has been dedicated to research of good photoanode materials. Although many other materials have been considered in PEC applications, $TiO_2$ still remains the most widely investigated photocatalyst in consideration of its properties, such as:

- high photocathalitic activity

- chemical inertness

- photocorrosion resistence

- non toxicity

- low cost

- abundant reserves.

It is well known that $TiO_2$ exists in three crystalline structures: rutile, anatase and brookite. Brookite phase has been scarcely used as photocatalysts, and consequently we will focus on anatase and rutile. All $TiO_2$ forms can be described as arrangement of slightly elongated $TiO_6$ octahedra connected in different ways by vertices and edges. Rutile and anatase $TiO_2$ are both tetragonal. The tetragonal anatase structure contains 12 atoms per conventional unit cell compared to the tetragonal rutile structure which contains only 6 atoms per conventional unit cell. The crystalline structure of the three phases are reported in Figure 1.16.
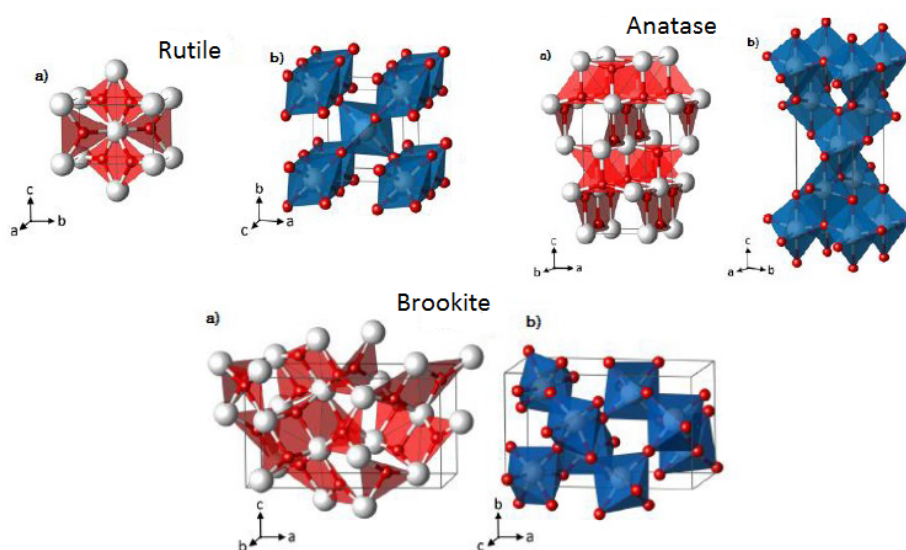


**Figure 1.16:** *Bulk structures of rutile, anatase and brookite*

Although rutile is generally considered the most stable polymorph, differences in the Gibbs free energy of formation between rutile and anatase are small (lower than $15\,KJ\,mol^{-1}$). Consequently, anatase can be easily obtained by synthesis at low temperature treatments (below $400\,°C$), but rutile frequently starts to appear at moderate temperatures ($400-600\,°C$) and it becomes the predominant phase after annealing at higher temperatures.

Due to the presence of a small amount of oxygen vacancies, which are compensated by the presence of $Ti^{3+}$ centres, $TiO_2$ is an n-type semiconductor. The valence band of this material is mainly formed by the overlapping of the oxygen 2p orbitals, whereas the lower part of the conduction band is mainly constituted by the 3d orbitals, with $t_{2g}$ symmetry, of $Ti^{4+}$ cations. The band gaps are 3.2 and 3.0 eV for anatase and rutile, respectively. Interband transitions of $TiO_2$ are indirect but factors like the crystalline size or the presence of dopants can modify the type of transition and somewhat conflicting reports are found in the literature.[36]

Although some discrepancies can be found in the literature, anatase is usually considered the most photoactive phase of $TiO_2$. Several reasons are proposed to explain differences in photoactivity between anatase and rutile structures, including variation in electronic (e.g. Fermi level position, electronic mobility) or surface properties (e.g. hydroxyl concentration). In addition, rutile generally presents lower surface area and higher density than anatase, due to the larger crystalline size imposed by thermodynamic constraints, and this fact may also contribute to lower photoactivity of this phase.[36]

The crystalline structure of the three phases and their properties are summarized in Table 1.2.

Table 1.2: Properties of bulk structures of $TiO_2$

| Structure | System | a (nm) | b (nm) | c (nm) | Density | Bandgap |
|---|---|---|---|---|---|---|
| Rutile | tetragonal | 0,4584 | 0,4584 | 0,2953 | 4240 | 3,0 |
| Anatase | tetragonal | 0,3733 | 0,3733 | 0,937 | 3830 | 3,2 |
| Brookite | orthorhombic | 0,5436 | 0,9166 | 0,5135 | 4170 | 3,3 |

## 1.5.1   Hierarchical quasi-1D Nanostructured $TiO_2$.

As already mentioned in the section 1.4.3, nanostructured photoanodes have attracted considerable attention over the last years. In the contrast to the bulk solid, nanocrystals present two main benefits for photocatalytic application: high surface area (increase of light harvesting and surface active sites) and relatively short transfer distance of carriers (decrease of electron/hole recombination).

In particular novel quasi 1-D hierarchical structures are among the most exciting developments in material engineering, in these recent years. Hierarchical tree-like $TiO_2$ nanostructures prepared by pulsed laser deposition (PLD) have been proposed as photoanodes for photoelectrochemical water splitting.[7].

Inspired by natural photosynthesis, hierarchical $TiO_2$ nano-forest, constituted by features which can be engineered at different length scales, have been developed for artificial photoelectrochemical water splitting. To clarify the concept of hierarchical assembled structures, a multiscale image of $TiO_2$ film prepared by PLD at 40 Pa is shown in Figure 1.17. The whole forest, corresponding to the whole film, has a film thickness in the µm range, the individual trees have diameters of hundreds of nanometers (mesoscale), and the size of each leaf is in nm range.[7]
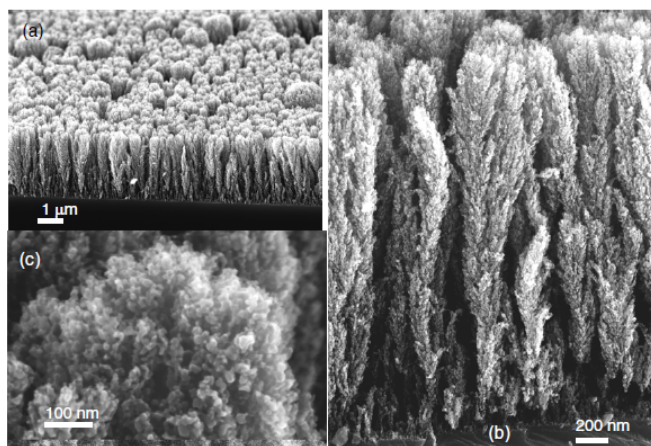


*Figure 1.17:* *SEM images of the sample deposited at* 40 Pa *after one hour annealing in air at* 400 °C, *showing the organization at different scales: (a) the uniform forest like assembly; (b) single trees; (c) high resolution image of a tree tip. This series of images clearly indicates that single $TiO_2$ nanoparticles are assembled in a three level hierarchical structure.[7]*

As a natural forest maximizes the gaseous exchange with the atmosphere by maximizing leaf area, while at the same time optimizing leaf exposure to the sunlight, in a similar way, a hierarchical structure with a multiscale organization and with a large and accessible surface area should opitimize photocatalytic performance.

It was demonstrated the possibility to obtain, by proper control of pulsed laser deposition parameters, $TiO_2$ films with different organizations, density,

particle size and specific surface area.[7]. PLD bottom-up synthesis approach allows the assembling of ultrafine nanoparticles (<10 nm) in a hierarchical superstructure that resembles a forest of trees, without any use of templates or pre-patterning. Indeed, by optimizing the PLD parameters, the single tree structure and the entire forest assembly were grown, with tailored crystalline structure and morphology at the sub-micrometer scale.

These mesoporous photocatalysts with controlled porosity possess two major beneficial characteristics. The first is the high specific surface area, which provides more reactive sites at the surface for photocatalytic reaction to occur. The second is the nanoscale channel wall of mesopores, which can facilitate the transfer of photogenerated electrons and holes to the surface, thus avoiding their recombination in the bulk. Since some years hierarchical tree-like $TiO_2$ nanostructures prepared by PLD are object of study at our laboratory for photovoltaic and water splitting application. Open morphologies characterized by a relevant porosity and a tree-like quasi-1D morphology have shown promising results achieving photocurrent values up to $200\,\mu A/cm^2$ and efficiency up to 8%.[32]

In this thesis, our work concerns the realization of $TiO_2$ quasi-1D nanostructures with optimized morphology and electronic properties through proper doping/stoichiometry control, and their testing as photoanodes for hydrogen production by photoelectrochemical water splitting.

### 1.5.2   Hydrogenated Titanium Dioxide. Black Titania.

$TiO_2$ as the most investigated photoelectrode and photocatalytic material, has a large band gap of about 3.2 eV, which limits its visible and infrared light absorption for solar water splitting. Doping of either metal or non-metal ions has proved effective to narrow the band gap of $TiO_2$ by introducing acceptor or donor levels in the forbidden band, which makes $TiO_2$ responsive to visible light (see section 1.4.2). However, because of the doping creates energy levels could also act as charge recombination centers, the solar water splitting activities of doped $TiO_2$ are limited and still at a low level.

As introduced in the section 1.4.4, Mao and his team [8] developed a new approach to improve visible and infrared optical absorption by engineering the disorder of nanophase $TiO_2$ with simultaneous dopant incorporation. In its simplest form, a disorder-engineered nanophase $TiO_2$ consists of two

phases: a crystalline $TiO_2$ quantum dot or nanocrystal as a core, and a highly disordered surface layer where dopants are introduced. (Figure 1.18 A) Nanocrystal core retains the benefits of crystalline $TiO_2$ quantum structures for photocatalytic processes, while the introduction of disorder and dopant at their surface would enhance visible and infrared absorption, with the additional benefit of carrier trapping. Instead of forming discrete donor states near the conduction band edge, large amounts of lattice disorder form a continuum extending bands that can overlap with the conduction band edge; thus they are often also known as band "tail states". These extended energy states, in combination with the energy levels produced by dopants, can become the dominant centers for optical excitation and relaxation. An additional potential advantage of these engineered disorders is that they provide trapping sites for photogenerated carriers and prevent them from rapid recombination, thus promoting electron transfer and photocatalytic reactions.

The disorder-engineered $TiO_2$ was typically synthesized by the hydrogenation of nanophase $TiO_2$ of approximately 8 nm in diameter in a 20 bar $H_2$ atmosphere at approximately 200 °C for 5 days, accompanied by a dramatic color change from white to black.(Figure 1.18 D) After hydrogenation, the black $TiO_2$ nanocrystals maintained the anatase structure. As revealed in Figure 1.18 B, the band gap of the unmodified white $TiO_2$ nanocrystals was approximately 3.3 eV, while the onset of optical absorption of the black disorder-engineered $TiO_2$ nanocrystals was lowered to approximately 1.0 eV ($\sim$ 1200 nm), which suggests that the optical gap of the black $TiO_2$ nanocrystals was substantially narrowed by intraband transitions. As illustrated in Figure 1.18 C, optical transitions from the blue-shifted valence band edge to these conduction band tail states arising from disorder are presumably responsible for optical absorption onset around 1.0 eV in black $TiO_2$ . In addition, the disorder-engineered $TiO_2$ nanocrystals exhibited substantial activity and stability in the photocatalytic production of hydrogen from water under sunlight. A full-spectrum solar simulator was used as the excitation source. During a 22-day testing period, black $TiO_2$ nanocrystals produced hydrogen continuously at a steady rate, without an obvious decrease in hydrogen evolution rate. It was demostrated that solar energy conversion efficiency as high as 24 % , is about two orders of magnitude greater than the yields of most semiconductor photocatalysts.[37] This is

because the disorder-engineered black $TiO_2$ can efficiently harvest photons from UV to near-infrared for photocatalysis.
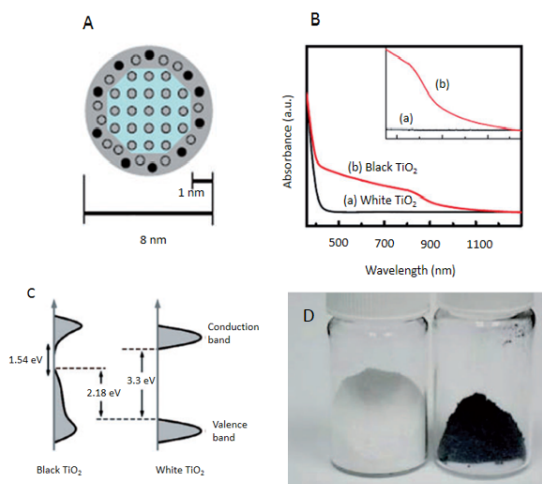


***Figure 1.18:*** *(A) Schematic illustration of the structure of disorder-engineered black $TiO_2$. (B) Spectral absorbance of the white and black $TiO_2$ nanocrystals. The inset enlarges the absorption spectrum in the range from approximately 750 to 1200 nm. (C) Schematic illustration of the DOS of disorder-engineered black $TiO_2$ nanocrystals, as compared to that of unmodified $TiO_2$ nanocrystals. (D)A photo comparing unmodified white and disorder-engineered black $TiO_2$ nanocrystals.*

Li et al.[38] revealed the significant effect of hydrogen treatment on the photocatalytic properties of rutile $TiO_2$ nanowires arrays (diameters of 100, 200 nm), which were prepared on a fluorine-doped tin oxide (FTO) glass substrate. They found that the color of the hydrogen-treated rutile $TiO_2$ nanowire films changed from white (untreated sample) to yellowish green (350 °C) and finally to black (450 °C or above). Under simulated sunlight illumination, the photo-current densities of the hydrogenated $TiO_2$ nanowire samples are at least two times higher than that of pristine $TiO_2$ nanowires.

Huang et al.[39] also evaluated the effect of hydrogen treatment on the photocatalytic activity of anatase $TiO_2$ nanowires. They showed that the hydrogen production rate over hydrogenated $TiO_2$ nanowires is 3.2 and 3.8 times higher than those over air-treated $TiO_2$ and commercial $TiO_2$, respectively.

Actually, the enhancement in the visible-light absorption of hydrogenated black $TiO_2$ is mainly attributed to two factors:

1. surface disorder;

2. the formation of oxygen vacancies.

However, the mechanism behind the disorder-engineering process is not fully understood. Liu et al. [40] have demostrated, by performing calculations based on the density functional theory (DFT), that a disordered lattice containing O-H and Ti-H bonds can generate midgap states in $TiO_2$ and thereby shrink its absorption onset. Recently, it has also shown that the H adatoms on surface $Ti_{5c}$ and $O_{2c}$ atoms can induce lattice disorders and contribute to midgap states. However, to explain the formation of black $TiO_2$ via hydrogenation requires more than just the hydrogen termination of Ti and O dangling bonds on the anatase surface. The exactly role of hydrogen in disordering the surface of anatase nanocrystals is still an open issue. In fact, normally, defects associated with disordered materials are detrimental to photocatalysis by acting as recombination sities.

Mao et al. showed that the surface disorder of anatase $TiO_2$ nanoparticles following hydrogen treatment shifted the valence band position by 2.18 eV. The density of states (DOS) of the valence band of $TiO_2$ nanocrystals was measured by valence band XPS. The white $TiO_2$ nanocrystals displayed typical valence band DOS characteristics of $TiO_2$, while for the black $TiO_2$ nanocrystals, a blue-shifts of the valence band maximum was appeared (see Figure 1.18 C). Moreover, the conduction band DOS of the black $TiO_2$ nanocrystals would not have as substantial a change. Nevertheless, there may be conduction band tail states arising from disorder that extend below the conduction band minimum. Optical transitions from the blue-shifted valence band edge to these band tail states are presumably responsible for optical absorption onset around 1.0 eV in black $TiO_2$.

On the contrary, Li et al. found that rutile $TiO_2$ nanowires with and without hydrogen treatment possess the same valence band position. Therefore, they attributed the absorption of visible and infrared light to the formation of oxygen vacancies in hydrogenated rutile $TiO_2$. The energy levels of the oxygen vacancies are about 0.75 and 1.18 eV below the conduction band of hydrogen reduced rutile $TiO_2$ single crystals. The visible- and near infrared- light absorptions are associated with the transitions from the $TiO_2$ valence band to the oxygen vacancy levels or from the oxygen vacancies to the $TiO_2$ conduction band.

Interestingly, it was found that the dramatic improvement in visible-light absorbance of hydrogenated black $TiO_2$ is not a main contributor to its enhanced photoactivity. As shown by both Mao et al. and Huang et al, when full solar radiation was filtered so that only visible and infrared light was allowed to reach hydrogenated $TiO_2$, the rate of $H_2$ production dropped of one order of magnitude. These results are consistent with IPCE measurements (incident-photon-to-current-conversion efficiency) reported by Li et al. For hydrogenated $TiO_2$ nanowires, IPCE values are higher than 95% in the wavelength range from 300 to 370 nm, indicating that the UV light is effectively used for water splitting. In contrast, the IPCE value decreases from roughly 95% at 370 nm to about 1% at 420 nm. This further confirms that the enhanced photocatalytic activity of the hydrogenated $TiO_2$ is mainly due to the improved IPCE in the UV region.[41]

In summary, the remarkable enhancement in the visible light absorption and the photocatalysis of $TiO_2$ after hydrogen treatment is truly a breakthrough in the photocatalytic splitting. This would increase the reality of $H_2$ production with solar energy. However, hydrogenated black $TiO_2$ does not fully exploit visible light for the photocatalytic process, because its enhanced photocatalysis is mainly due to the IPCE increase in the UV region. Therefore, it would be an interesting and important research direction to boost the photocatalytic activity of the hydrogenated black $TiO_2$ in the visible-light region.

## 1.6   Objectives of this work

In this thesis, our work concerns the realization of hydrogenated $TiO_2$ quasi-1D nanostructures, prepared by pulsed laser deposition (PLD), and their testing as photoanodes for hydrogen production by photoelectrochemical water splitting. First, $TiO_2$ thin films are deposited with PLD in $O_2$, $Ar/O_2$ and $Ar/H_2$ atmospheres (pressure at 5 Pa). Then, a thermal treatment in air at 500 °C or 650 °C is performed in order to induce crystallization; in addition, it has been followed by or substituted with a hydrogenation treatment at the same temperatures in a $Ar/H_2$ (97%-3%) mixture at atmospheric pressure, aiming to the introduction of oxygen vacancies and/or a H doping and to form the so called black titania.

We started from the results obtained by the previous research, in our lab-

oratory.[32] The effect of changing the oxygen background pressure during deposition on the morphological/structural properties and on photoelectro-chemical behaviour of $TiO_2$ nanostructured photoanodes prepared by PLD was investigated. At low pressure (3 Pa) a compact and dense film was obtained, while a gradual variation of film morphology from compact to-wards a hierarchical nanoporous assemby was observed changing the pres-sure from 3 Pa to 5 Pa and 10Pa. From photoelectrochemical behaviour point of view the best performance sample has been prepared at 5 Pa, which have shown higher photocurrent density in the whole potential range (around $65\,\mu A/cm^2$), as shown in Figure1.19 (A). Moreover, for optimal $TiO_2$ pho-toanode (5 Pa), the effect of the mass of deposited material (or equivalently the film thickness) has been also analysed. Three samples with mass 0.5 M, M and 2 M (M $\sim$ 0 3-0.4 g/cm$^2$ corresponding to thickness of 1.35 μm) has been deposited at the same oxygen pressure (5 Pa). The phoelectrochemi-cal results are reported in Figure 1.19(B). Finally, the effect of temperature post-deposition annealing on photoresponce has been evaluated. The re-sults, reported in Figure 1.19(C), have revealed that the best performance sample was annealed at 650 °C.
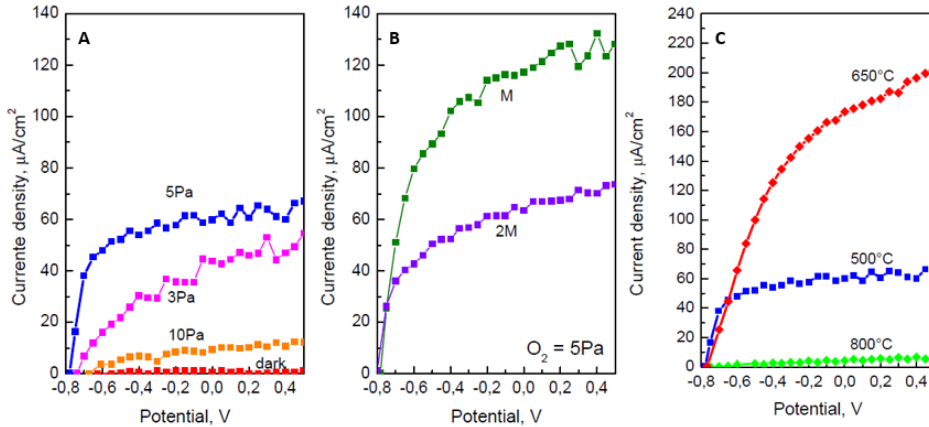


**Figure 1.19:** *Current-potential responses in 0.1M KOH solution under illumination: (A) $TiO_2$ photoanodes produced at different background pres-sure. (B) $TiO_2$ photoanodes produced at 5 Pa $O_2$ by varying the mass surface density. (C) $TiO_2$ photoanodes produced at 5 Pa $O_2$ with 0.5M by varying the annealing temperature.*

Starting from these results, in this framework the main goals of our work

are as follows:

- The preparation of $TiO_2$ samples at room temperature by PLD at pressure of 5 Pa, investigating three different background gases: pure $O_2$, $Ar/O_2$ at 50 % and $Ar/H_2$ with 3% of $H_2$. The effect of different deposition atmospheres on morphological and structural properties is analysed by Scanning Electron Microscopy (SEM) and Raman spectroscopy, in order to obtain hierarchical nanostructured films.

- The investigation of three different types of post-deposition thermal annealing: air annealing at 500 °C for 2 hours, in order to induce crystallization, thermal treatment in $H_2/Ar$ (3%) flow at 500 °C for 3 hours and co-treatment (air annealing for 2 hours followed by $H_2/Ar$ treatment for 3 hours both at 500 °C). Morphological, structural and optical properties are analyzed aiming to understand the effect of hydrogenation. In particular, as it has already been demostrated in the literature, a probable visible band-gap shift, induced by hydrogen treatment, was calculated.[34][8] [42] [43]

- Photocurrent tests and stability in time, performed in Laboratory of Catalysis and Catalytic Processes (LCCP), were evaluate in order to understand photoelectrochemical behavior.

- Finally, further developments are performed in order to optimize photoanode samples. The effect of variation of annealing temperature from 500 °C to 650 °C on samples deposited at 5 Pa of pure $O_2$, on morphological, structural properties and photocurrent behaviour was investigated. Finally the variation of deposition pressure from 5 Pa to 10 Pa, for the sample deposited in $Ar/H_2$ atmosphere was evaluated.

CHAPTER 2

---

Materials and Methods

---

## 2.1 Pulsed Laser Deposition (PLD)

Pulsed Laser Deposition (PLD) is a PVD (Physical Vapour Deposition) technique based on the production of a plasma from a material target irradiated by intense laser pulses.

PLD has demostrated a great versatility for the production of a wide range of materials, such as metals, ceramics, oxides, semiconductors and even biomolecules in the form of films and multilayers. Indeed, PLD has emerged as a powerful method for the deposition of materials with high complex stechiometry.[44]

The ablation process originates from the interaction between the laser pulse and the target surface and the physics of ablation and plume expansion is extremely complex therefore in this section only the main aspects of the process will be considered.

The PLD working principle can be summarized as follows: first, a high energy pulsed laser spot is focused onto the surface of a solid target, whose surface is ablated. The vaporized species subsequently expand in the form of a supersonic plasma with a characteristic plume shape until they reach the deposition substrate placed in front of the target, where condensation and film growth takes place.

The typical scheme of a PLD apparatus, as shown in Figure 2.1, is composed

by a laser source and a vacuum chamber hosting the target material and the substrate. Typically, laser pulses (which in this case is the order of ns) are focused on the target material inside the chamber through an optical path constituted by mirrors, lenses and a viewport. Laser pulses have a typical incidence angle of $40 - 50°$ with respect to the normal direction to the target surface while the substrate is placed in front of the target. The deposition chamber is equipped with manipulators for the exernal control of the positions of target and the substrate. Both target and substrate have a roto-traslational movements in order to have homogeneous deposition. The chamber is evacuated to high vacuum conditions by a pumping system consisting of a primary and a turbomolecular pump and can then be filled with a background gas at a controlled pressure by a gas inlet system with mass flow controllers and pressure gauges.

The background atmosphere (gas type and pressure) can be modified to
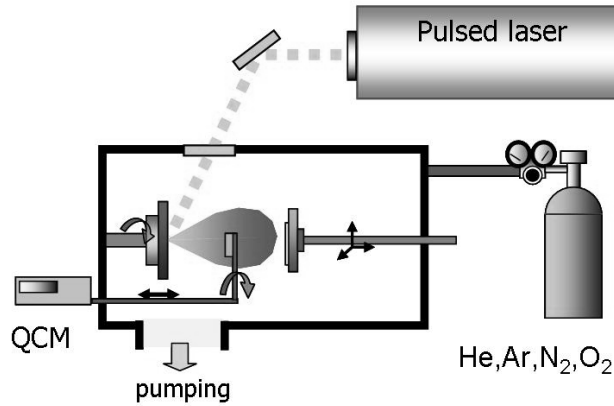


**Figure 2.1:** *schematic of Pulsed Laser Deposition Setup*

achieve control of the growth of the film and of morphology. (Figure 2.2)

- In low pressure conditions, the species ablated from the target proceed almost without collisions and reach the substrate with high kinetic energy, leading to atom-by-atom deposition of compact and bulk-like dense films.

- If pressure is increased, the background gas molecules and the ablated species undergo collisions which can lead to the spatial confinement

44

of the ablation plume. Upon collisions, clusters are formed in the gas phase and the kinetic energy with which the substrate is reached is lower.

- At higher pressures the diffusion of clusters in the gas is favored, and their kinetic energy is further decreased.
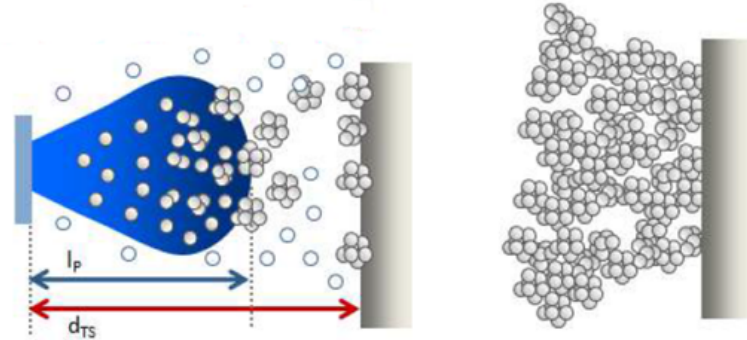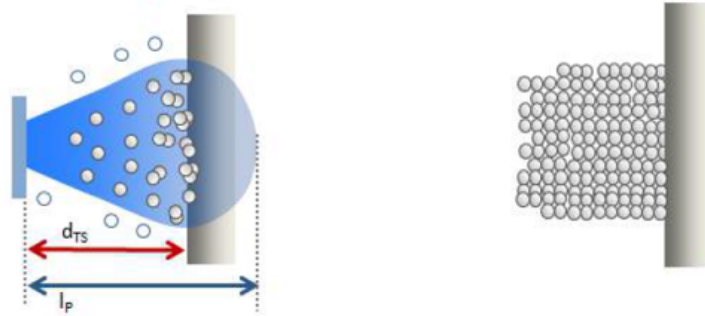


***Figure 2.2:*** *Schematic picture of PLD conditions for different pressure values.*

A useful parameter to identify the deposition regime is L, defined as the ratio of the target-to-substrate distance $d_{TS}$ to the visible plume length $l_p$. L is a non dimensional characteristic length which indicates the relative position of the substrate with respect to the plume length. With reference

to the L parameter we identify distinct deposition regimes in the presence of a background gas:

- L $<$1 (substrate in plume): the collisions are not sufficient to induce signicant clustering, resulting in a smooth surfaces and compact film.

- L $\sim$ 1 (substrate at the plume edge): the expected effect is the increase of interactions between ablated species and the surrounding gas and a reduced kinetic energy of the species, resulting in a vertically oriented film;

- L$>$1 (substrate out of plume): plume confnement induced by collisions favors cluster nucleation and leads to the deposition of cluster assembled nanostructured materials.

Laser fluence is another important parameter for controlling of morphology, since it affects the plume expansion dynamics. It is defined as the incident photon number (or incident photon energy) per unit area. Increasing the fluence, the amount of ablated material increases and kinetic energy also increases.
A few drawbacks of PLD as a deposition technique should also be mentioned: first, the deposited films have uniform thickness only over a small area (of the order of $1\,\mathrm{cm}^2$). Thickness uniformity can be increased by performing off-axis depositions and rotating the substrates, in order to obtain a circular corona of several $\mathrm{cm}^2$ with uniform thickness. Second, during the ablation phase molten particles are ejected in the form of droplets, which appear in the film as spherical protrusions which are detrimental in case low surface roughness is required.

## 2.2   Scanning Electron Microscopy (SEM)

The scanning electron microscope (SEM) uses a focused beam of high-energy electrons to generate a variety of signals at the surface of solid specimens. The signals that derive from electron-sample interactions reveal information about the sample including external morphology (texture), crystalline structure and orientation of materials at high resolution (higher than $1\,\mathrm{nm}$). In most applications, data are collected over a selected area of the surface of the sample, and a 2-dimensional image is generated that displays spatial variations in these properties.

## 2.2 Scanning Electron Microscopy (SEM)

Electrons extracted can be accelerated in the 200-30000 eV range. Accelerated electrons in an SEM carry significant amounts of kinetic energy, and this energy is dissipated as a variety of signals produced by electron-sample interactions when the incident electrons are decelerated in the solid sample. These signals include secondary electrons, backscattered electrons, diffracted backscattered electrons. Secondary electrons and backscattered electrons are commonly used for imaging samples: secondary electrons are most valuable for showing morphology and topography on samples and backscattered electrons are most valuable for illustrating contrasts in composition in multiphase samples.[45]

SEM analysis is considered to be non-destructive, a semplified scheme of
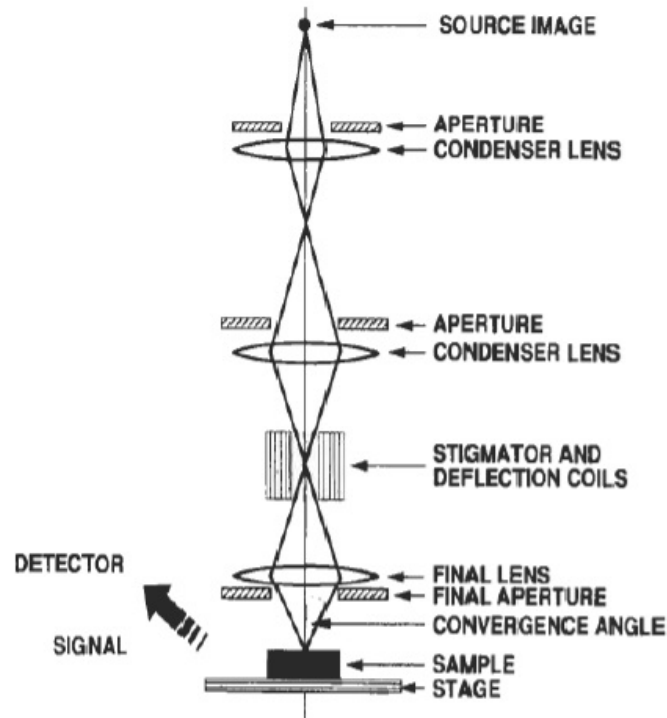


***Figure 2.3:*** *Schematic rapresentation of SEM apparatus[45]*

SEM is reported in Figure 2.3. Essential components of SEM include the following:

- Electron source (electronic gun);

- Electron lenses;

47

- Sample stage;

- Detector;

- Display/Data output device.

In this work Field Emission Zeiss SEM was used to obtain the superficial and cross section images of the specimens ($TiO_2$ on silicon substrate). The voltage was around 5 KV and the work distance was fixed at 4 mm.

## 2.3   Raman Spectroscopy

Raman spectroscopy is a spectroscopic technique based on inelastic scattering of monochromatic light, usually from a laser source. Inelastic scattering means that the frequency of photons in monochromatic light changes upon interaction with a sample. Photons of the laser light are scattered. Frequency of the reemitted photons is shifted up or down in comparison with original monochromatic frequency, which is called the Raman effect. This shift provides information about vibrational, rotational and other low frequency transitions in molecules and crystals. Raman spectroscopy is primarily a structural characterization tool. Because the spectrum is sensitive to the lengths, strengths, and arrangement of bonds in a material it can be used for sample identification and quantitation. The Raman spectrum of crystals is also sensitive to defects, disorder and quantum confinement.

From a physical point of view, the Raman effect of a crystal can be explained by considering a simple molecule. It is based on molecular deformations in electric field $\vec{E}$ determined by molecular polarizability $\alpha$. The laser beam can be considered as an oscillating electromagnetic wave with electrical vector $\vec{E}$. Upon interaction with the sample, it induces electric dipole moment $\vec{P} = \alpha\vec{E}$ which deforms molecules.[46] Because of periodical deformation, molecules start vibrating with characteristic frequency $\nu_m$. The expression of electric dipole moment is:

$$P = \alpha_0 E_0 \cos 2\pi\nu_0 t + \frac{E_0}{2} r_m (\frac{\partial\alpha}{\partial r}) \cos 2\pi(\nu_0 - \nu_m)t$$
$$+ \frac{E_0}{2} r_m (\frac{\partial\alpha}{\partial r}) \cos 2\pi(\nu_0 + \nu_m)t \quad (2.1)$$

where $\alpha_0$ is the instantaneous polarizability at equilibrium intermolecular

displacement, $E_0$ is the amplitude of electric field of incident light, $r$ and $r_m$ are the instataneous and maximum distance from equilibrium position respectively. This expression consist of three terms: the first is elastic scattering (Reyleigh scattering) the others are called Stokes and Anti-Stokes analestic scattering respectively. From the equation (2.1) we can deduce that the condition in order to have Raman effect is $(\frac{\partial \alpha}{\partial r}) \neq 0$.

In other words, a monochromatic laser light with frequency $\nu_0$ excites molecules and transforms them into oscillating dipoles. Such oscillating dipoles emit light of three different frequencies when:

- A excited molecule with no Raman-active modes returns back to the same basic vibrational state and emits light with the same frequency $\nu_0$ as an excitation source. This type of interaction is called an elastic Rayleigh scattering.

- A photon with frequency $\nu_0$ is scattered by Raman-active molecule which at the time of interaction is in the basic vibrational state. Part of the photons energy is transferred to the Raman-active mode with frequency $\nu_m$ and the resulting frequency of scattered light is reduced to $\nu_0 - \nu_m$. This Raman frequency is called Stokes frequency, or just Stokes.

- A photon with frequency $\nu_0$ is scattered by a Raman-active molecule, which, at the time of interaction, is already in the excited vibrational state. Excessive energy of excited Raman-active mode is released, molecule returns to the basic vibrational state and the resulting frequency of scattered light goes up to $\nu_0 + \nu_m$. This Raman frequency is called Anti-Stokes frequency, or just Anti-Stokes.

In Figure 2.4 (a), the molecula energy levels diagram and elestic and analastic scattering are reported. As shown in figure, according to quantum mechanics, the vibrational energy levels of molecules, described as quantum harmonic oscillator model, are quantized. The energies are:

$$E = (n + \frac{1}{2})h\nu \qquad (2.2)$$

where h is Planck's constant and n is integer number from 0 to infinite.

Moreover, as shown in Figure 2.4 (b) the two spectra (Stokes and Anti-Stokes) are mirror images on opposite sides of the Rayleigh line. Indeed,
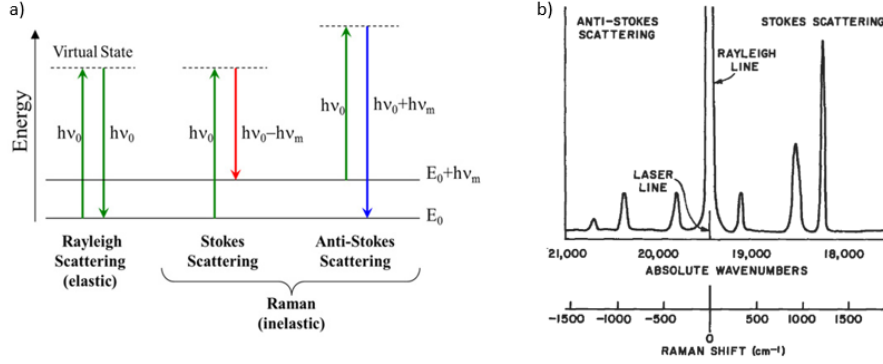
***Figure 2.4:*** *Energy levels diagram (a) and Raman scattering spectrum (b).*

the intensity are different, Stokes peaks are more intense than Anti-Stokes. This effect depends on the different energy level population. According to Bolzmann distribuition:

$$N_1 = N_0 e^{-\frac{\Delta E}{Kt}} \tag{2.3}$$

where $N_1$ and $N_0$ are the number of particles in the energy levels, $\Delta E$ is the energy difference between the two levels and K is the Boltzmann constant. At room temperature, due the fact that most molecules are in the lower state, there is a much lower probability that a photon will be Anti-Stokes scattered.

A Raman system typically consists of four major components:

1. Excitation source (Laser).

2. Sample illumination system and light collection optics.

3. Wavelength selector (Filters).

4. Detector (CCD).

In this work, Raman spectra of all $TiO_2$ samples were collected using a Renishaw InVia micro Raman spectrometer, equipped with a optical microscopy. A schematic rapresentation is illustrated in Figure 2.5. An argon ion laser (514 nm) was used for laser excitation of the Raman signal. The laser power at the sample was around 1 mW and spectral resolution of about $3 \, cm^{-1}$.
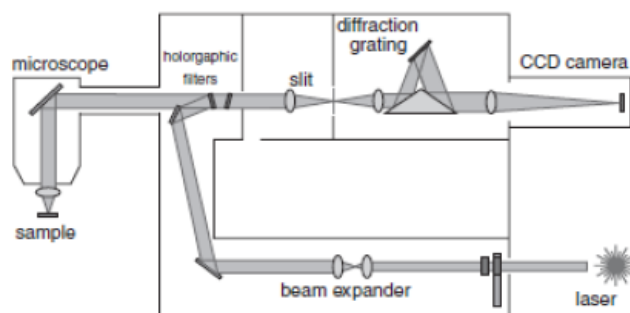
**Figure 2.5:** *Raman apparatus.*

## 2.4  UV/VIS/NIR spectroscopy

A Lambda 1050 UV/Vis/NIR system was used as a spectrophotometer with
an integrating sphere. The integrating sphere modulus is a Perkin Elmer
150 mm sphere. The optical trasmittance (total and diffuse) and reflectance
have been measured in the wavelength range between 250 nm to 2000 nm,
with data interval of 2 nm. The different measurements schemes are shown
in Figure 2.6. In the case of total trasmittance measuraments (Figure 2.6
(a)), the samples were placed at the entrance of the sphere, in order to have
the film in contact with the sphere and the spectralon in the rear position.
The integrating sphere collects all the light which is passed through the sam-
ple, moreover it introduces the possibility to do the diffuse transmittance,
removing the spectralon (Figure 2.6 (b)). For reflectance measurements
(Figure 2.6 (c)), samples were mounted in the rear sample mount.The total
transmitted light intensity T over the whole solid angle at each wavelength
of the used range, is normalized dividing by the contribution of the substrate
(glass). The transmittance of the bare substrate (pure glass) is measured
and then it is used as a reference when measuring T of the samples. Light
scattering properties are measured by calculating the haze factor, i.e. the ra-
tio of diffuse transmittance to total transmittance, according to the scheme
depicted in Figure 2.7. The fraction of scattered transmitted light S is mea-
sured by opening the integrating sphere in order to let the specular light
out, undetected. S is then divided by the total transmittance T in order to
obtain the haze factor H.

From transmittance and reflectance measurements it is also possible to
extract information about the coefficient of absorption ($\alpha$), the absorbance
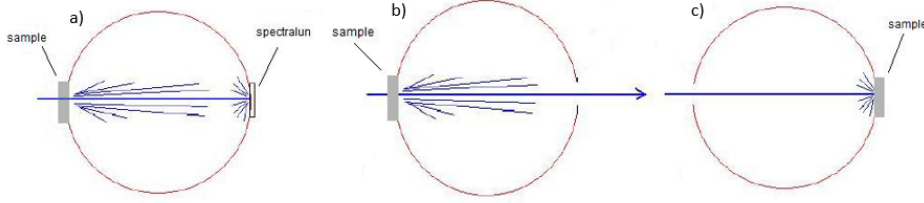
**Figure 2.6:** *Total trasmittance (a), diffuse trasmittance (b) and reflectance (c) measuraments schemes.*
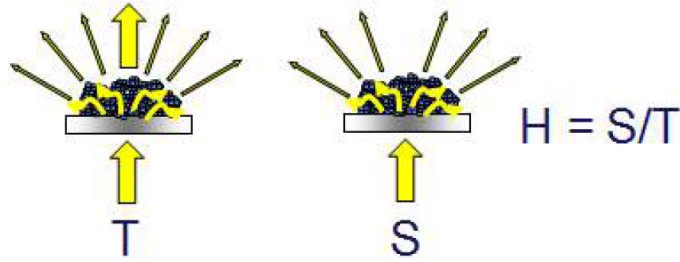


**Figure 2.7:** *Scheme of the haze factor measurements. S is the diffuse transmittance, T the total transmittance, H the haze.*

$(A = 1 - T - R)$ and the optical gap with the Tauc method.[47] For this purpose, trasmittance and reflectance were measured in a reduced wavelength range, from 290 nm to 600 nm with data interval of 0.2 nm. Experimental value of absorption coefficient, according to Lambert Beer' s law is:

$$\alpha = \frac{-1}{d} ln(\frac{T}{1 - R}) \qquad (2.4)$$

where d is the thickness of the sample, T is the trasmittance and R is the reflectance. The theoretical ralationship between the absorption coeffcient $\alpha$ and the optical gap $E_g$ is given by:

$$\alpha = C(h\nu - E_g)^{\frac{1}{r}} \qquad (2.5)$$

where the constant C depends on the optical transition matrix element and the parameter r indicates the type of transition (r $= 1/2$ for indirect bandgap transitions, which is the case of $TiO_2$). The equation (2.5) shows that the function $\alpha^r$ must have a linear behaviour as a function of $h\nu$, and the intercept with the $\alpha = 0$ axis is found for $h\nu = E_g$, i.e. in correspondence of the

optical gap. This is the basic principle of Tauc method, where $\alpha^r$ is plotted as a function of $h\nu$, and a linear fit close to the absorption edge is used to determine $E_g$. In some cases, $(\alpha h\nu)^r$ is plotted rather than $\alpha^r$.

## 2.5   Photocurrent apparatus

The photoelectrochemical water splitting behaviour was investigated through the measurement of the photocurrent in aqueous KOH solution (0.1 M) with a three-electrodes configuration PEC, equipped with a quartz window for illumination, consisting of:

- a $TiO_2$ photoanode (nominally $1\,cm^2$) as working electrode (WE), which potential is established by an external potentiostat system;

- a saturated calomel electrode (SCE) as reference elctrode (RE), which potential is constant during the measure;

- a platinum grid as counter electrode (CE), which close the circuit and acts as catalyst to hydrogen reduction.

The external bias was provided by a potentiostat (Amel 7050) with potential ramps from OCV to about 0.55 V. The lamp used is a solar Simulator with a 300W Xe-Arc lamp and a UV filter was used in order to eliminate UV component and to evaluate visible activity. The photocurrent measurement apparatus is shown in Figure 2.8.
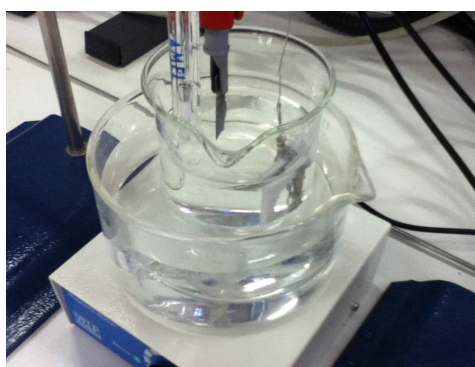


***Figure 2.8:*** *Photocurrent measurament apparatus.*

Experimental results

In this chapter the experimental results are presented and discussed. In general, the followed experimental procedure consists of six steps:

1. sample deposition by PLD;

2. SEM and Raman characterizations;

3. annealing treatments;

4. SEM and Raman characterization in order to evaluate the morphological and structural changes due to annealing;

5. analysis of optical properties;

6. photocurrent measurements in order to evaluate the photocatalytic activity.

Our work concerns the realization of hydrogenated-$TiO_2$ hierarchical nanostructures, prepared by PLD at room temperature. We started from the results obtained by previous researches in our laboratory. The value of deposition pressure (5 Pa) and deposition time are chosen in order to have best performance sample. It was demostrated that $TiO_2$ photoanode deposited at 5 Pa with a thickness around 1.4 μm showed the best photocurrent density in the whole potential range.[32] Thus we have considered it as reference for

our further analysis. The aim of our experiments was the introduction of oxygen vacancies and/or H doping and the formation of hydrogenated-$TiO_2$ (the so-called black titania). For this purpose we have followed two strategies. First of all, exploiting the properties of PLD introduced in section 2.1, three different background gases are used during deposition: pure oxygen (99,999%), already tested in our laboratory, a mixture of argon and oxygen at 50%, in order to have a more reducing atmosphere, and a mixture of argon and hydrogen gas with 3% of $H_2$, aiming to introduce hydrogen already during deposition phase. The effect of different deposition atmospheres on the morphology, structure, optical and photo-catalytic properties was investigated. The second strategy was to introduce hydrogen during post-deposition annealing. For this aim, three different post-deposition thermal treatments were initially carried out:

- Air annealing at 500 °C for 2 hours;

- $Ar/H_2$ annealing at 500 °C for 3 hours;

- Air annealing followed by $Ar/H_2$ annealing at 500 °C for 2 and 3 hours respectively.

After the same thermal treatments were also performed at 650 °C only for samples deposited at 5 Pa of pure $O_2$, as discussed in the chapter 4. The choice of these thermal annealing takes inspiration from literature, considering the available instrumentation in our laboratory. Recently, black titania was reported prepared from hydrogenating $TiO_2$ nanocrystals at 20 bar $H_2$ atmosphere for very long time (∼5 days).[8] However, others report hydrogenated $TiO_2$ prepared by annealing at high pressure $H_2$ at 500 °C for 1 hour or by annealing in $Ar/H_2$ flow at 500 °C for 1 hour.[42][43]

In the first part of the chapter, Section 3.1 presents a detailed description of sample preparation by PLD. In the Section 3.2 morphological and structural characterizations of both the as-deposited and annealed samples are reported, by means of SEM images and Raman spectroscopy. Section 3.3 describes the effects of thermal treatments on the structure of $TiO_2$, while in section 3.4 the effect of background gas during deposition is investigated. In the second part of the chapter, in section 3.5 optical analysis are performed in order to evaluate the film trasmittance and absorbance and optical band gap was evaluated by Tauc method. In section 3.6 photocurrent tests and

stability in time were evaluated for all samples. Finally, in section 3.7 a summary and further developments are presented.

## 3.1   Sample preparation

The $TiO_2$ photoelectrodes were prepared via two steps:

1. deposition by PLD;

2. post-deposition thermal treatments.

$TiO_2$ nanostructured films have been deposited by ablation of a solid $TiO_2$ target with green ($\lambda = 532$ nm) laser pulses from a frequency quadrupled Nd:YAG laser, with pulse duration about 5-7 ns and $10\,Hz$ frequency. The laser fluence on the target was about $3.5\,J/cm^2$. An example of ablation plume of the $TiO_2$ target at $5\,Pa$ oxygen pressure is shown in figure 3.1, we can note that the substrate is at the plume edge (L $\sim$1) in order to increase the interaction between ablated species and the surrounding gas, resulting in low kinetic energy and nanoporous film. Indeed, as explained in section 2.1, when L$\sim$1 the plume is highly directional and unquenched leading to hierarchical quasi 1D tree-like structures. Silicon, glass and Ti were used as substrates (silicon was used for SEM analysis, glass for Raman spectroscopy and titanium for photocurrent measures) mounted on an off-axis rotating sample holder at a fixed target-to-substrate distance of $50\,mm$ in order to have as much as possible uniform films. Ti plate substrates for photoelectrochemical measurements were masked to deposit on a $1\,cm^2$ area and to leave a clean surface for electrical contacts. All the depositions were performed with substrates kept at room temperature. To calculate the deposition rate we made a deposition test for thirty minutes and then we measured the thickness by SEM analysis. However after each deposition the real thickness of the samples was evaluated by SEM analysis. Chamber pressure value (5 Pa) is kept constant during the three types of deposition: pure oxygen (99,999%), argon/oxygen at 50 % and argon/hydrogen at 3% of $H_2$. The deposition parameters are reported in table 3.1. Several sets of these samples are deposited in order to investigate the effects of different thermal annealing. The thermal treatment in air at $500\,°C$ or $650\,°C$ was performed in order to induce crystallization; in addition, it was followed by or substituted with a combined annealing and hydrogenation treatment at

| Sample | Gas | Gas Flow (SCCM) | P (Pa) | $d_{ts}$ (cm) | Real Thickness (µm) |
|---|---|---|---|---|---|
| $O_2$-$TiO_2$ | $O_2$ | 40 | 5 | 5 | 1,40 |
| $Ar/O_2$-$TiO_2$ | $Ar/O_2$ | 20(Ar) 20($O_2$) | 5 | 5 | 1,40 |
| $Ar/H_2$-$TiO_2$ | $Ar/H_2$ | 40 | 5 | 5 | 0.97 |

Table 3.1: Deposition Parameters

the same temperatures in a $Ar/H_2$ (97%-3%) mixture at atmospheric pressure, aiming at the introduction of oxygen vacancies and/or a H doping. Air thermal treatment was performed in a muffle, while the hydrogen treatment was performed using a handmade furnace. In this case the chamber was first evacuated in order to obtain a good vacuum (around $10^{-6}$ mbar), then it was filled with desired gases ($Ar/H_2$) to pressure around 1050 mbar. For each sample prepared in different deposition atmosphere, one sample was prepared by annealing the as-deposited film in air at 500 °C for 2 hours (denoted as Air-$TiO_2$). The hydrogen-treated sample was prepared by annealing the as-synthesized sample at 500 °C in $Ar/H_2$ for 3 hours (denoted as $ArH_2$-$TiO_2$). The co-treated sample was prepared by first annealing in air at 500 °C for 2 hours, followed by annealing in $Ar/H_2$ at 500 °C for 3 hours (denoted as Air + $ArH_2$-$TiO_2$). In all cases the time refers to the plateau, in which samples reach the maximun temperature above indicated. In the air annealing, the temperature ramp rate was 4 °C/min while the cooling occurred spontaneously. In the $Ar/H_2$ treatment, both temperature ramp and the cooling rate were approximately 10 °C/min. The qualitative trend of temperature in time during the two types of annealing is reported in Figure 3.2.

## 3.2    Morphological and structural characterization

SEM analyses were performed on $TiO_2$ on silicon substrates with a ZEISS Supra 40 FEG-SEM without any sample preparation. Film thickness was evaluated by cross-sectional SEM images. Raman spectra were measured on $TiO_2$ on glass with a Renishaw InVia micro Raman spectrometer with 514.5 nm laser excitation wavelength. As described in the section 2.2, Raman spectroscopy is a non-destructive technique, which is sensitive to the
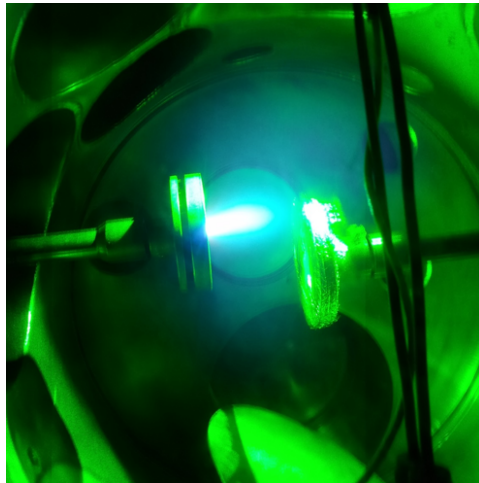
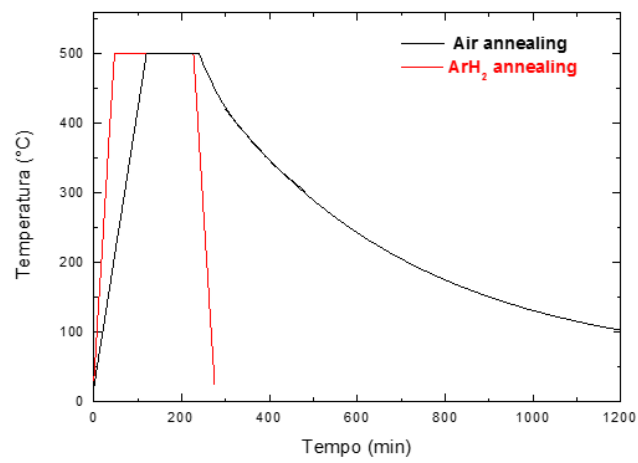***Figure 3.1:*** *Plume image during PLD deposition.*



***Figure 3.2:*** *Trend of temperature in time during annealing treatments.*

local crystalline order/disorder and it gives information about the structure, crystallinity and allotropic phase of $TiO_2$.[48]

**$TiO_2$ Raman analysis**

The three polymorphs of $TiO_2$ belong to different space groups: $D_{4h}(I4_1/amd)$ for anatase, $D_{2h}$ (pbca) for brookite, and $D_{4h}$ (P4$_2$/mnm) for rutile, which have distinctive characteristics in Raman spectra. For anatase $TiO_2$, there are six Raman active modes with frequencies at $144\,cm^{-1}$ ($E_g$), $197\,cm^{-1}$ ($E_g$), $399\,cm^{-1}$ ($B_{1g}$), 519 (superimposed with the $515\,cm^{-1}$ band) ($A_{1g}$, $B_{1g}$ ), and $639\,cm^{-1}$ ($E_g$), respectively . Rutile has four Raman active modes with frequency: $143\,cm^{-1}$ ($B_{1g}$), $447\,cm^{-1}$ ($E_g$), $612\,cm^{-1}$ ($A_{1g}$), $826\,cm^{-1}$ ($B_{2g}$). All Raman peaks of $TiO_2$ anatase and rutile are shown in Figure 3.3 and their values are listed in the following table 3.2. [48]. Brookite is the most difficult titania phase to prepare in thin-film form, however examples in literature report brookite Raman lines at 128, 246, 320, and $366\,cm^{-1}$.[49]
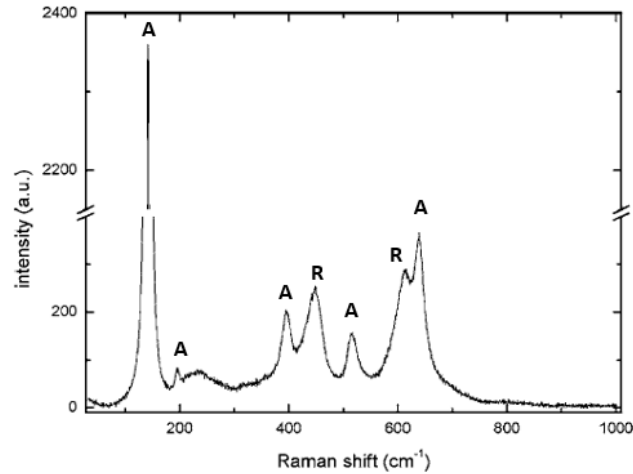


***Figure 3.3:*** *Raman spectrum of a commercially available rutile anatase micropowder mixture [48].*

| Raman peaks | | |
|---|---|---|
| | Published data ($cm^{-1}$) | Assigned mode |
| Rutile | 143 | $B_{1g}$ |
| | 447 | $E_g$ |
| | 612 | $A_{1g}$ |
| | 826 | $B_{2g}$ |
| Anatase | 144 | $E_g$ |
| | 197 | $E_g$ |
| | 399 | $B_{1g}$ |
| | 519 | $A_{1g}, B_{1g}$ |
| | 639 | $E_g$ |

Table 3.2: Raman peaks of active mode of rutile and anatase $TiO_2$ [48]

### 3.2.1 Pure $O_2$-deposited sample

In Figure 3.4 SEM cross section and surface images of as-deposited sample obtained in pure $O_2$ deposition atmosphere at 5 Pa pressure are shown. The thickness is quite uniform, around 1.4 µm. The morphology is granular and nanoscale porosity appears, however the tree-like hierarchical structure is not evident, in agreement with previous experiments, in which tree-like morphology occurred at pressure >10 Pa.[32]



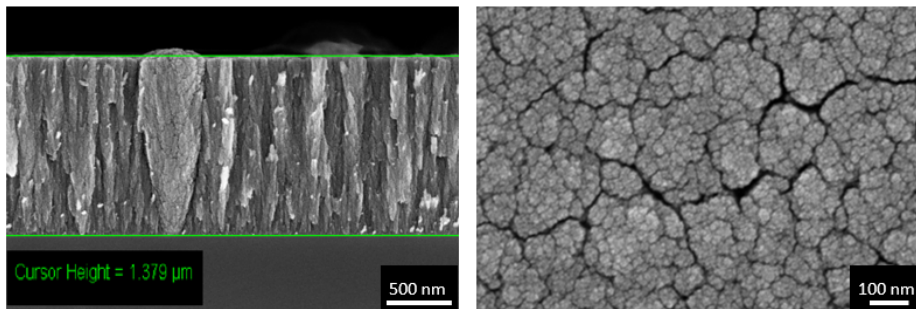***Figure 3.4:*** *SEM cross section (on the left) and surface (on the right) images of pure $O_2$-deposited sample.*

Figure 3.5 shows SEM images of the same sample grown in pure $O_2$ atmosphere as deposited, after annealing in air for 2 hours at 500 °C, after annealing in $Ar/H_2$ for 3 hours at 500 °C and finally after annealing in air for 2 hours followed by $Ar/H_2$ treatment for 3 hours both at 500 °C. Notably,

the thermal treatments don't affect the overall morphology of the structure and the thickness of the sample after each thermal treatments doesn't change . However nanoporous hierarchical tree-like structures become more evident after annealing, expecially after $Ar/H_2$ treatment, as shown in SEM images at high magnification reported in Figure 3.6. Figure 3.7 shows top view of the samples after each annealing. The same scale bare outlines a variation of porosity, both after air annealing and hydrogenation treatments. Moreover, air annealing seems to lead to a greater sintering effect than argon/hydrogen tratment, with increased coalescence and thus connectivity among nanoparticles.
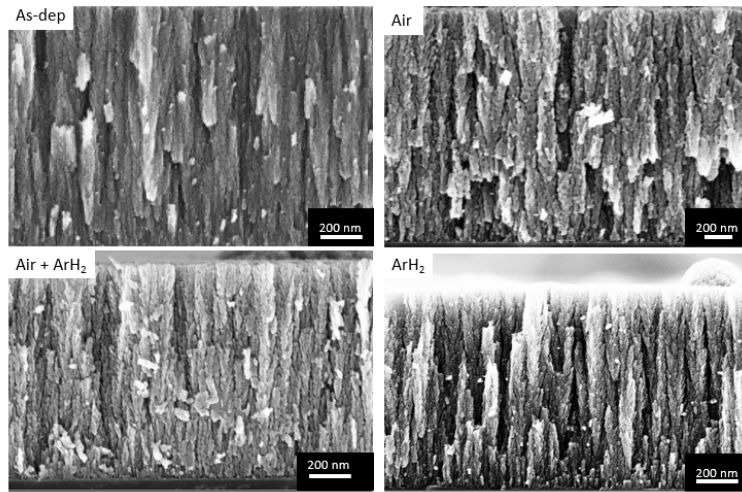


*Figure 3.5:* *SEM cross-section images of as-deposited, air annealed, $Ar/H_2$ annealed and air followed by $Ar/H_2$ annealed samples, deposited at $5\,Pa$ of pure $O_2$.*

The crystalline structure of the films was characterized by Raman spectroscopy. As expected, Raman spectroscopy indicates that as-deposited sample is amorphous, as a result of the room temperature growth process. On the contrary, all thermal treatments induce a transition to a crystalline structure, i.e. anatase $TiO_2$ (Figure 3.8). Moreover we can note that Raman spectra of $Ar/H_2$-treated and $Air+Ar/H_2$ co-treated samples are characterized by a photoluminescence (PL) background. The mechanism underlying this phenomenon is not fully understood. However, as reported in literature, photoluminescence at a certain energy can be viewed as indication of radiative recombination through defects states, and it is thus an indication
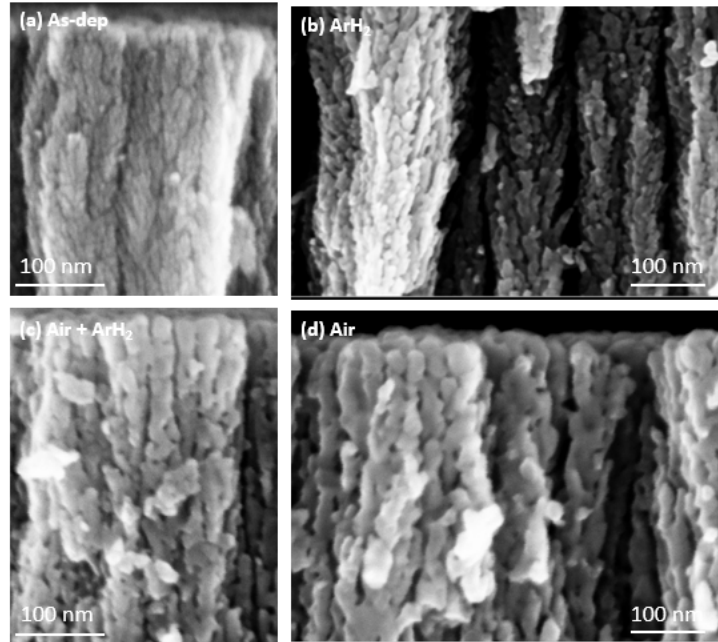
***Figure 3.6:*** *SEM cross section images at different magnification of the sample deposited at* $5\,\mathrm{Pa}$ $O_2$ *as-dep and after annealing.*
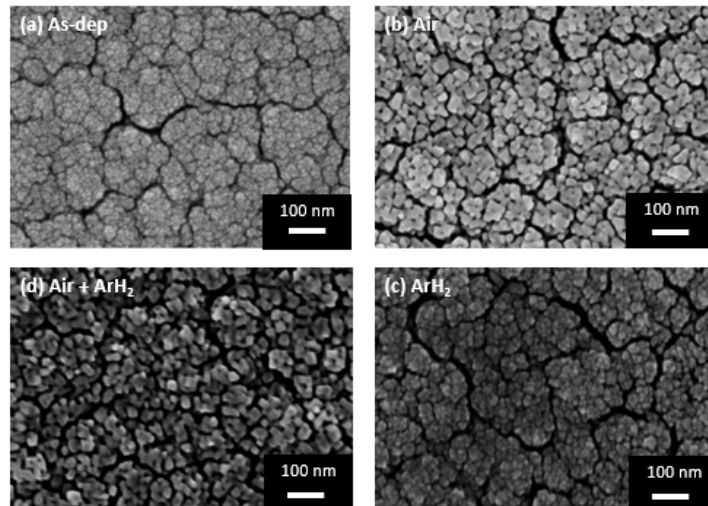


***Figure 3.7:*** *Top view SEM images of (a) as-deposited (b) air-annealed (c) Ar/$H_2$-annealed and (d) air + Ar$H_2$ annealed samples deposited in pure oxygen at* $5\,\mathrm{Pa}$.

of presence of defects most probably induced by treatment in hydrogen.[50]. Therefore in this thesis pholuminescence effect is not take into consideration, but it will be object of future studies. Furthermore, we can note that the peaks intensity of the sample after only $Ar/H_2$ annealing (line black in Figure 3.8) appears lower than the other two samples. It's probably due to a lower cristallinity degree after hydrogenation than after air thermal treatment.
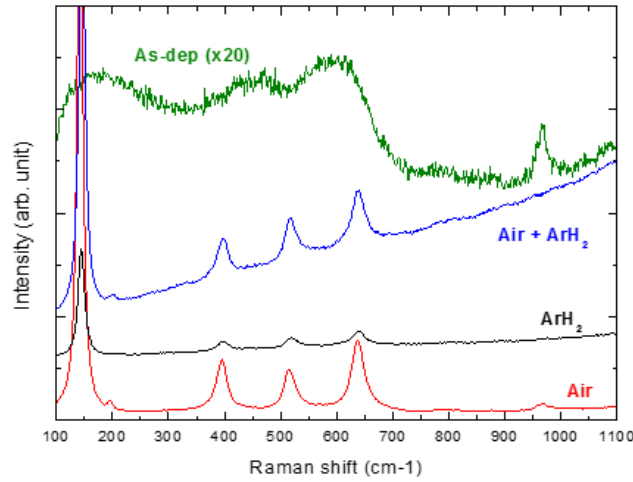


**Figure 3.8:** *Raman spectra of as-deposited (green line), Air-annealed (red), $Ar/H_2$ annealed (black), Air followed by $Ar/H_2$ annealed (blue) samples prepared via PLD at 5 Pa of pure $O_2$.*

### 3.2.2 Ar/O$_2$-deposited sample

The second set of samples was prepared at the same deposition pressure (5Pa) as the previous one, but the background gas in the PLD chamber was replaced with a mix of two gas at 50 %, argon and oxygen. Figure 3.9 shows top view and cross-section SEM images of as-deposited sample. As in the previous case, the thickness is quite uniform, around 1.4 µm. The morphology is characterized by oriented porous columnar domains of hundreds of nanometer size. As the samples deposited in pure $O_2$, the structure is quite hierarchical, composed by nanoscale particles, therefore tree-like domains becomes evident only after annealing.

Figure 3.10 shows SEM images of samples deposited at 5 Pa of $Ar/O_2$ as-deposited and after the three types of annealing, described in the for-
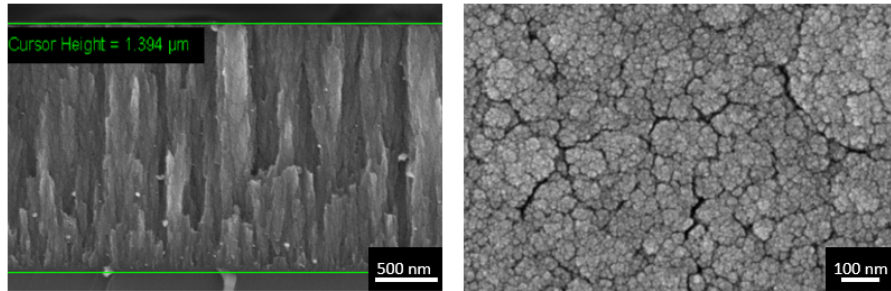
**Figure 3.9:** *SEM cross section (on the left) and surface (on the right) images of Ar/O₂ atmosphere deposited sample.*

mer section. Once again, the thermal treatments don't affect the overall morphology of the structure and the thickness of the sample after each thermal treatments doesn't change. However, air annealing seems to lead to a greater sintering effect than argon/hydrogen tratment, with increased coalescence and thus connectivity among nanoparticles, as seen in Figure3.11, in agreement with the results obtained from pure-$O_2$ deposited samples.



**Figure 3.10:** *SEM cross-section images of as-deposited, air annealed, Ar/H₂ annealed and air followed by Ar/H₂ annealed samples deposited in Ar/O₂ atmosphere at 5 Pa.*

Likewise, Raman spectroscopy indicates that as-deposited sample is amorphous or disordered. All thermal annealing induce a transition to a crys-

65

**Figure 3.11:** *Top view SEM images of (a) as-deposited (b) air-annealed (c) Ar/H$_2$-annealed and (d) air + ArH$_2$ annealed samples deposited at 5 Pa in a mixture of Ar and oxygen (at 50 %).*



**Figure 3.12:** *Raman spectra of as-deposited (green line), Air-annealed (red), Ar/H$_2$ annealed (black), Air followed by Ar/H$_2$ annealed (blue) samples prepared via PLD at 5 Pa of a ArO$_2$ mixture.*

66

talline anatase $TiO_2$ structure. In Figure 3.12 anatase $TiO_2$ peaks appear, while rutile peaks are not present. Again, PL background appears only after $Ar/H_2$ treatment.

### 3.2.3   $Ar/H_2$-deposited sample

The third set of samples were prepared at the same deposition pressure (5 Pa), but here the background gas in the chamber was a mix of argon and hydrogen, with 3% of $H_2$. Figure 3.13 shows top view and cross-section SEM images of as-deposited sample. The thickness is almost uniform but lower than the other two samples (around 1 µm). This is in agreement with different morphology, in fact a more compact and dense film is obtained.
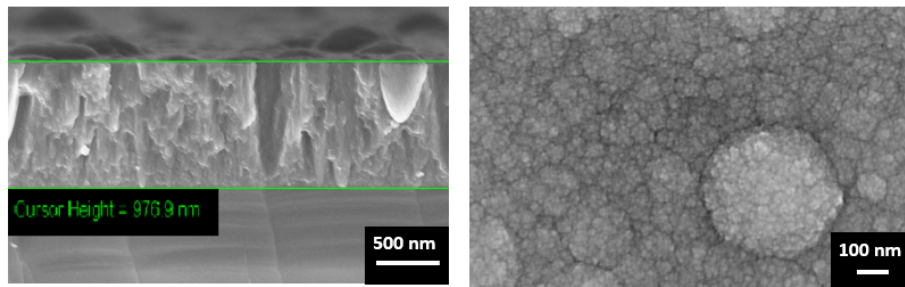


*Figure 3.13:* *Cross section SEM image (on the left) and top view SEM image (on the left) of as-deposited sample prepared via PLD at* 5 Pa *of a mixture of Ar and hydrogen.*

Figure 3.14 shows SEM images of samples deposited at 5 Pa of $Ar/H_2$, after deposition and after the three annealing procedure above discussed. Unlike all of the other cases, we can note that the vertically oriented structures seem to disappear after both air annealing and $Ar/H_2$ treatment, confirming a more dense and compact morphology. The effect of thermal treatments on morphology of $TiO_2$ film prepared in $Ar/H_2$ deposition atmosphere, is shown in Figure 3.15. Apparently, in this case the sintering effect due to air annealing vanishes. Because of the morphology obtained at 5 Pa of $Ar/H_2$ is too compact, probably characterized by low surface area, a new deposition was performed at higher background pressure in order to have more porous film. This new approch is described in the chapter 4. Raman spectra, shown in Figure 3.16 confirms anatase $TiO_2$ structure after all thermal annealing
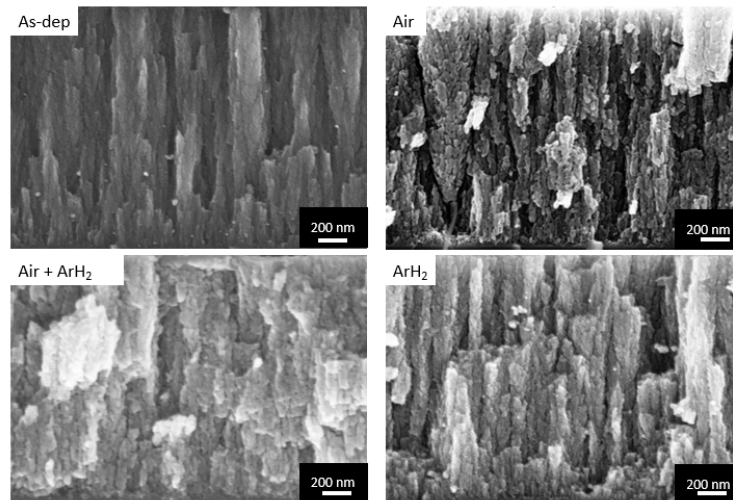
**Figure 3.14:** *SEM cross-section images of as-deposited, air annealed, Ar/H₂ annealed and air followed by Ar/H₂ annealed samples deposited in Ar/H₂ atmosphere at 5 Pa.*
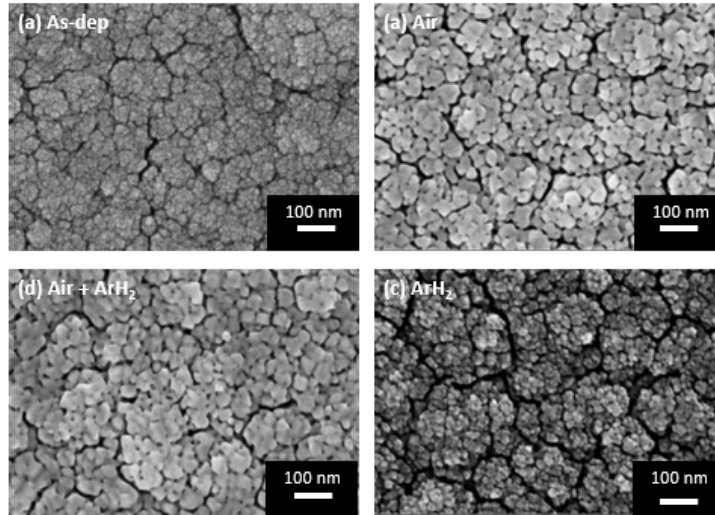


**Figure 3.15:** *Top view SEM images of (a) as-deposited (b) air-annealed (c) Ar/H₂-annealed and (d) air + ArH₂ annealed samples deposited at 5 Pa in a mixture of Ar and hydrogen.*
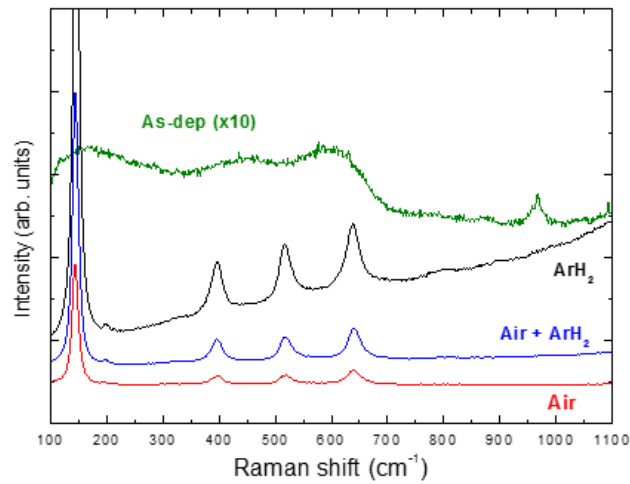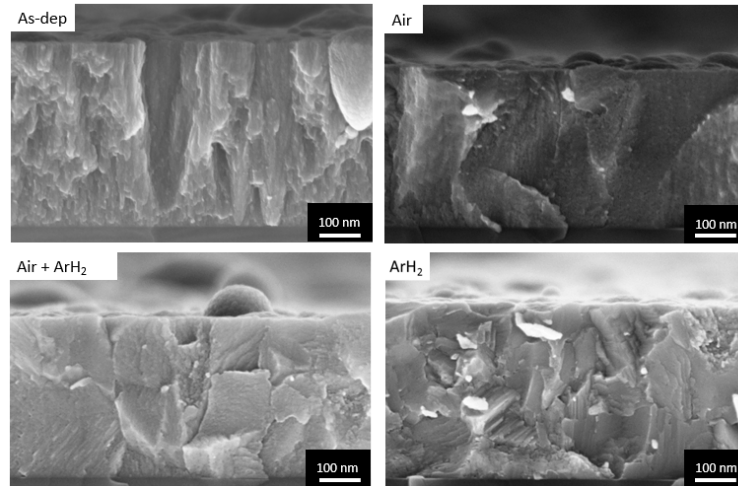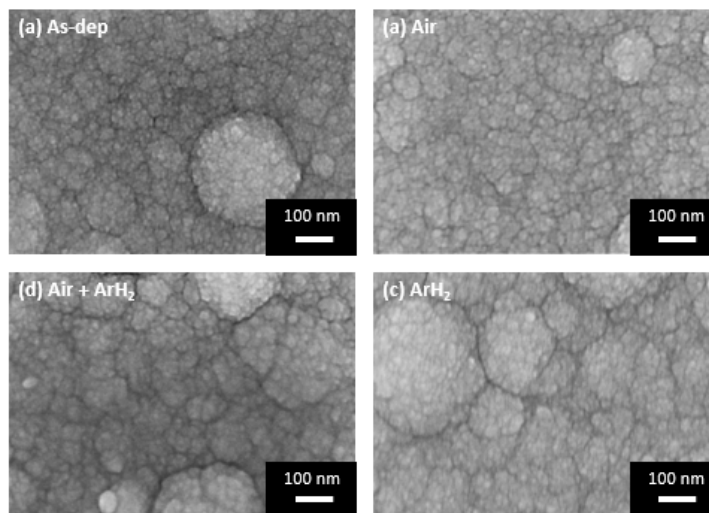
treatments and a PL background for samples after hydrogenation.
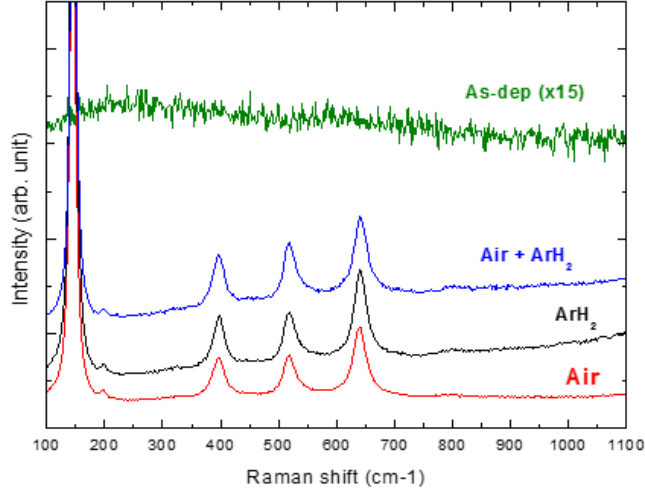


**Figure 3.16:** *Raman spectra of as-deposited (green line), Air-annealed (red), Ar/H$_2$ annealed (black), Air followed by Ar/H$_2$ annealed (blue) samples prepared via PLD at 5 Pa of ArH$_2$ mixture.*

## 3.3   Effect of annealing treatments: Raman analysis

In this section a study of the Raman spectra, in particular of the $E_g$ Raman peak at $144\,\mathrm{cm}^{-1}$ of anatase TiO$_2$ is presented. As described in the previous section, Raman spectra indicate that the three set of samples, after annealing in air at $500\,^\circ$C for 2 hours, after annealing in Ar/H$_2$ gas at $500\,^\circ$C for 3 hours and after air followed by Ar/H$_2$ annealing for 2 and 3 hours respectively are crystalline. The TiO$_2$ crystalline phase is always anatase. Figure 3.17 shows the position values of principal anatase Raman peaks for the samples prepared at $5\,\mathrm{Pa}$ in O$_2$ deposition atmosphere, obtained by fitting with Lorenztian function using OriginPro software. We can note a Raman shift of $2\,\mathrm{cm}^{-1}$ for ArH$_2$ and Air + ArH$_2$ samples. Likewise, Figure 3.18 and 3.19 report the position of main anatase peaks of samples after annealing prepared in Ar/O$_2$ and Ar/H$_2$ deposition atmosphere respectively. Here too, a small Raman shift is apparent. In the table 3.3 all anatase Raman peak position values for all samples are reported. We can note that there

are no significant Raman shifts not only for the main peak but also for the other ones.

In literature [48], it has been demostrated that the shift and linewidth of the $E_g$ Raman peak at $144\,\mathrm{cm}^{-1}$ of anatase $TiO_2$ nanopowders depend on two main contributions:

- the stoichiometric defects;

- the size of nanocrystal composing the film.

The stoichiometric influences the shape and position of $E_g$ Raman peak in the same way as particles size, due to confinament effect. Reducing the size (less than roughly $10\,\mathrm{nm}$) a significant Raman shift and broadening have been observed.

In Figure 3.17 $E_g$ peak of the sample after $Ar/H_2$ treatment appears to be less intense and broader, probably due to an incomplete cristallinity or stechiometry defects as oxygen vacancies. However this effect doesn't occurr in sample deposited in $Ar/O_2$ and $Ar/H_2$.



**Figure 3.17:** *Raman peaks of anatase $TiO_2$ sample prepared via PLD at 5 Pa of pure $O_2$ after air-annealing (red line), ArH (black) and Air followed by $ArH_2$ treatments (blue).*

70

***Figure 3.18:*** *Raman peaks of anatase $TiO_2$ sample prepared via PLD at 5 Pa of $Ar/O_2$ after air-annealing (red line), ArH (black) and Air followed by $ArH_2$ treatments (blue).*



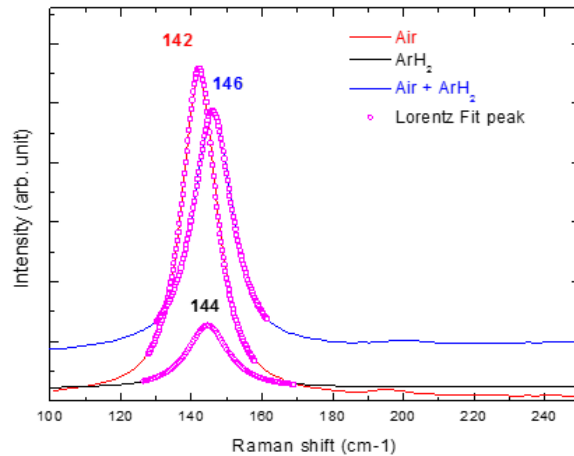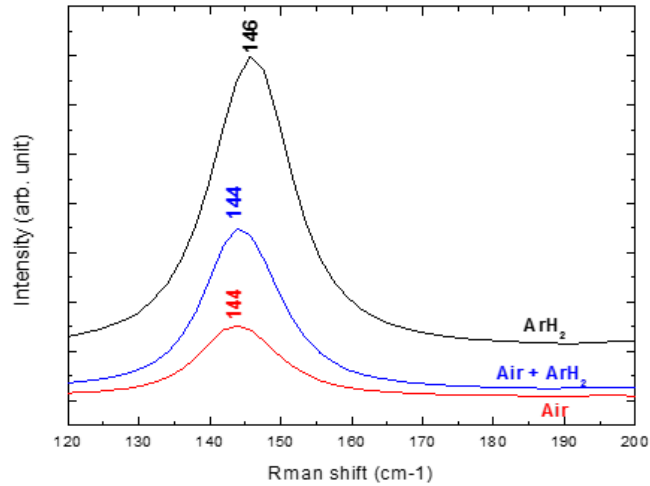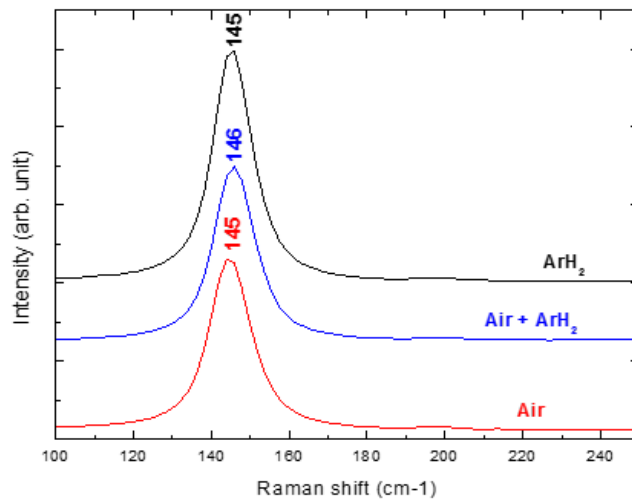***Figure 3.19:*** *Raman peaks of anatase $TiO_2$ sample prepare at 5 Pa of $Ar/H_2$ after air-annealing (red line), ArH (black) and Air followed by $ArH_2$ treatments (blue).*

71

| Sample | Annealing | $E_g$ | $E_g$ | $B_{1g}$ | $A_{1g} + B_{1g}$ | $E_g$ |
|---|---|---|---|---|---|---|
| O$_2$-dep TiO$_2$ | Air | 142 | 194 | 395 | 516 | 638 |
| | ArH$_2$ | 144 | 198 | 398 | 520 | 639 |
| | Air + ArH$_2$ | 146 | 199 | 397 | 518 | 639 |
| Ar/O$_2$-dep TiO$_2$ | Air | 144 | 198 | 396 | 519 | 639 |
| | ArH$_2$ | 146 | 198 | 396 | 518 | 638 |
| | Air + ArH$_2$ | 144 | 196 | 396 | 518 | 640 |
| Ar/H$_2$-dep TiO$_2$ | Air | 145 | 196 | 397 | 518 | 640 |
| | ArH$_2$ | 145 | 198 | 397 | 519 | 641 |
| | Air + ArH$_2$ | 146 | 198 | 397 | 519 | 641 |

Table 3.3: Anatase TiO$_2$ Raman peaks obtained by fitting with Lorentzian peak function.

## 3.4 Comparison of different deposition atmospheres

Figure 3.20 shows SEM images of pristine TiO$_2$ prepared via PLD in the same deposition conditions (pressure at 5 Pa and target-substrate distance of 50 mm), by varying the background gas. From the cross sections presented in figure 3.20 a,b the nanoporous morphology with vertically orientated structures is evident for both oxygen and argon/oxygen gases. On the contrary, the cross sectional image of the sample deposited in argon/hydrogen atmosphere (figure 3.20 c) shows a more compact and dense film. This effect can
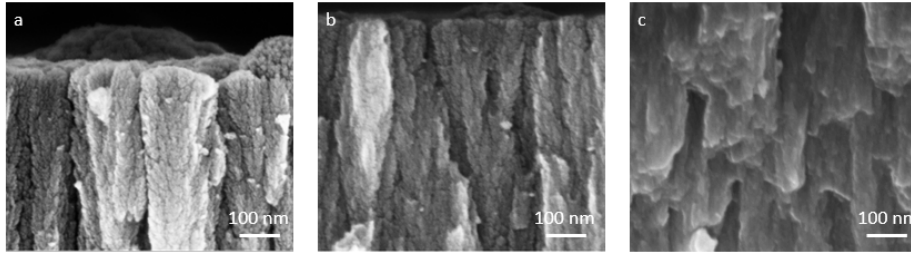


***Figure 3.20:*** *SEM cross section images of pristine TiO$_2$ deposited in pure (a) O$_2$, (b) Ar/O$_2$ and (c) Ar/H$_2$ atmosphere.*

be understood considering the PLD deposition phenomen and parameters, which affect the film growth, as explained in the section 2.1. The similarity between pure O$_2$ and Ar/O$_2$ is probably due to the relatively close values of the atomic mass of Ar and the molecular mass of O$_2$, resulting in com-

parable energy loss upon inelastic collisions with the ablated species. As consequence, analogous morphologies are obtained without any variation of deposition parameters. Instead, during $Ar/H_2$ deposition, due to smaller molecular mass of $H_2$ the kinetic energy with which the substrate is reached is higher, leading to less significant energy decrease in inelastic collision and a more compact film occurs. However, we also must consider that the amount of hydrogen is very low (3%), so other effect must be taken into account. The different morphologies are also probably related to the presence of oxygen during deposition, which reacts with ablated species deeply affecting the dynamic of plume expansion.

Raman spectra of pristine samples deposited at different background gas and after thermal teatments are reported. Figure 3.21 shows spectra of air annealed samples at 500 $^{\circ}C$ for 2 hours. Figure 3.22 shows spectra of $Ar/H_2$ annealed samples at 500$^{\circ}C$ for 3 hours. Figure 3.23 shows co-treated samples (Air + $ArH_2$ thermal annealing). No evident Raman shifts appear for samples deposited in the different background gases after the same thermal treatment and photoluminescence occurs only after hydrogenation.



**Figure 3.21:** *Raman spectra of air-annealed samples deposited at 5 Pa in pure $O_2$ (black line), in $Ar/O_2$ (red line) and in $Ar/H_2$ (blue line).*
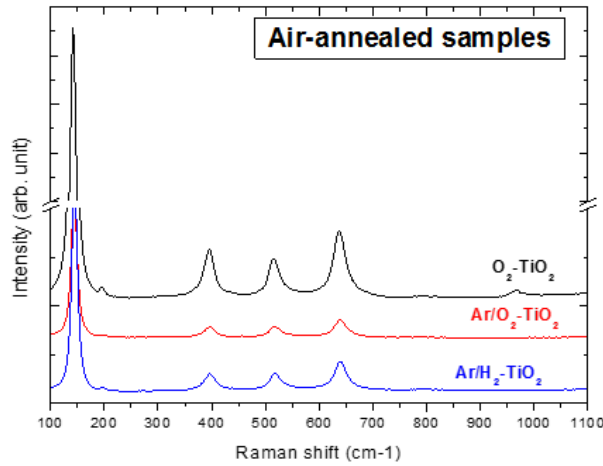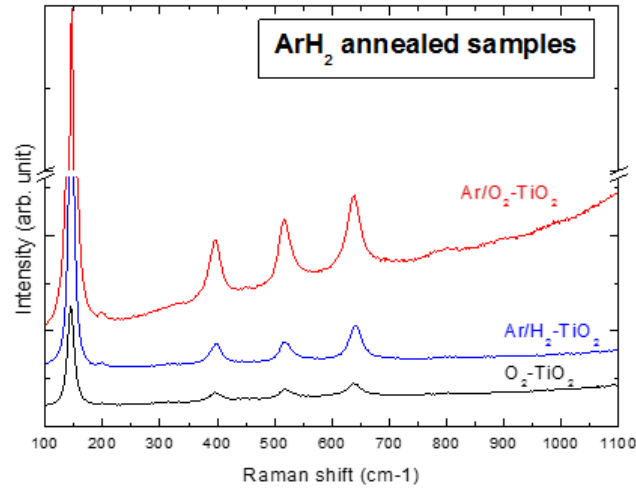
**Figure 3.22:** *Raman spectra of Ar/H₂-annealed samples deposited at 5 Pa in pure O₂ (black line), in Ar/O₂ (red line) and in Ar/H₂ (blue line).*
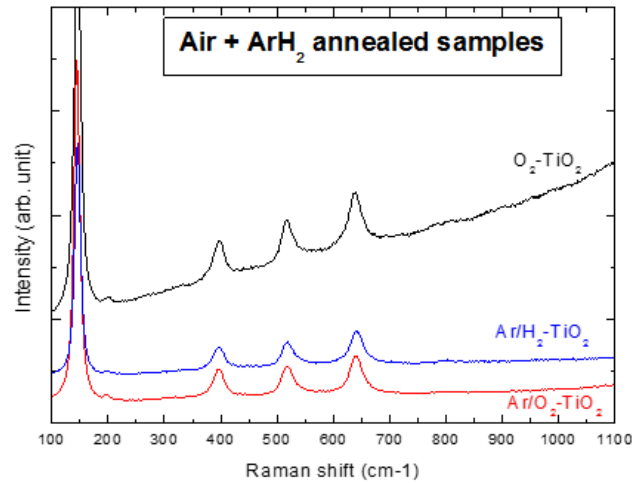


**Figure 3.23:** *Raman spectra of Air followed by Ar/H₂-annealed samples deposited at 5 Pa in pure O₂ (black line), in Ar/O₂ (red line) and in Ar/H₂ (blue line).*

74

## 3.5   Optical properties

In order to increase PEC efficiency, as described in section 1.4, many efforts have been focused on enhancing visible absorption by narrowing the band gap of $TiO_2$. Recently, as described in section 1.5, black titania with optical band gap $\sim 1.54\,eV$, narrowed by intraband transition, due to the presence of band tail states in the mid-gap, was reported.[8]

In this section, the optical properties were measured with a UV/VIS/NIR spectrophotometer. As mentioned in section 2.3, the total transmittance and reflectance and the diffused transmittance have been characterized by an integrating sphere module, in order to show the photoanode optical properties and to estimate the optical band gap.

As the first step, the total trasmittance of the samples, normalized with repect to the glass substrate has been measured. As described in previous section, the three set of samples deposited in three different background gases (pure $O_2$, a mixture of Ar and $O_2$ at 50 % and a mixuture of Ar with 3% of $H_2$) after the three different annealing (air annealing at $500\,°C$, $Ar/H_2$ annealing at $500\,°C$ and air annealing followed by $ArH_2$ treatment both at $500\,°C$) are considered. The experimental measured thickness is around $1.4\,\mu m$ for $O_2$ and $Ar/O_2$ deposited samples and it is around $0.9\,\mu m$ for $Ar/H_2$ deposited samples. Optical trasmittance (300 nm-2000 nm range) and absorbance spectra (300 nm-600 nm range) for each sample are presented in Figures 3.24, 3.25, 3.26, 3.27. In Figure 3.25, reflectance of the sample deposited in pure $O_2$ is also reported. We can note that the reflectance contribution is very low, so absorbance can be approximated as $A = 1 - (T + R) \approx 1 - T$.

As shown in the figures 3.24, 3.26, the color of the $TiO_2$ samples depends on the thermal treatment. For the pure $O_2$ and $Ar/O_2$ deposited samples, it changes from white (air annealed sample) to yellowish (air + $ArH_2$ annealed sample) and finally greywish ($ArH_2$ annealed sample). The dark color seems to suggest that the $TiO_2$ has a visible light absorption as a result of hydrogen treatment. Unlike, for $Ar/H_2$ deposited samples the color doesn't change after hydrogenation (Figure 3.27). In Figures 3.25 and 3.26 (on the right) the effect of the thermal treatments appears: in proximity of the optical band gap, the absorption edge is sharper after only air annealing. On the contrary the samples thermally treated in $Ar/H_2$ atmosphere have

smoother absorption edge shifted toward longer wavelength. This effect is probably due to the presence of the mid-gap defect states associated to oxygen vacancies, induced by $Ar/H_2$ atmosphere. However, this is not true for $Ar/H_2$ deposited samples, which show very small absorption changes after annealing in $Ar/H_2$ atmosphere (Figure 3.27 on the right).

Moreover, as shown in Figure 3.27 (on the left) the fringes in the visible and infrared range, due to interference phenomen, appear greater in the case of $Ar/H_2$ deposited samples. The fringes profile depends on the sample thickness and morphology. Therefore, in agreement with morphological characterization reported in the previous section, $Ar/H_2$ deposited samples appear more compact and dense. This probably means that they have more ordered structure, higher density and lower surface roughness which promote coherent optical phenomena. On the contrary, pure $O_2$ and $Ar/O_2$ deposited samples seem to have more porous and disordered morphology, which suppresses eventually coherent optical phenomena.

By comparing the absorption coefficient ($\alpha$) of the samples prepared at different atmosphere deposition (pure $O_2$ and $Ar/O_2$), after the same annealing treatment ($Ar/H_2$ annealing and air followed by $Ar/H_2$ treatment), it is possible to conclude that these samples show the same absorption qualitative trend. The absorption coefficient was estimated as $(1/d) * ln(\frac{T}{1-R})$, where d is the thickness, T the trasmittance and R the reflectance. In Figure 3.28 the samples annealed only in $Ar/H_2$ gas are reported, while in Figure 3.29 the samples annealed first in air and than in $Ar/H_2$ are shown. In both cases a small variation of $\alpha$ around band-gap edge appears and $Ar/O_2$ deposited samples seem to have just a little higher $\alpha$ value.

The light scattering capability of $TiO_2$ samples was evaluated by measuring the diffused-transmission and by calculating the haze factor. Haze factor is defined as the ratio between the diffuse transmitted light to the total transmitted light. The effect of the three thermal annealing on diffused trasmission light and on the homologous haze factor for the three set of samples is shown in Figures 3.30, 3.31 and 3.32. In the latter two cases as deposited sample spectra are also shown. We can note that in all cases, the air annealed samples show the highest amount of scattered light followed by Air+ $ArH_2$ treated and $ArH_2$ treated samples. However the normalized Haze factor is very similar for all samples.

Another important information that we can get from the optical mea-
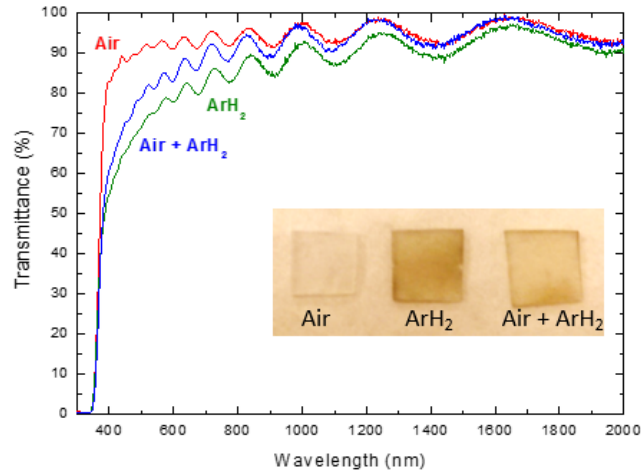
**Figure 3.24:** *Total normalized trasmittance vs. wavelength for samples deposited at 5 Pa of $O_2$ , after the three thermal treatments (inset: pictures for the differently treated samples).*
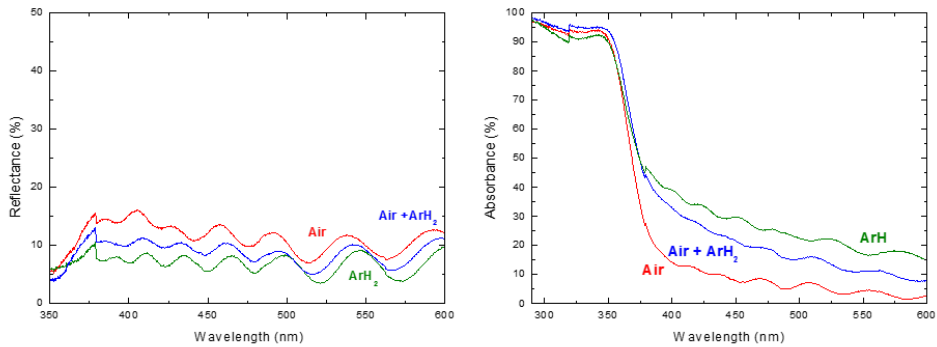


**Figure 3.25:** *Total reflection vs. wavelength (on the left) and absorbance vs. wavelength (on the right) for the samples deposited at 5 Pa of pure $O_2$ after thermal treatments.*
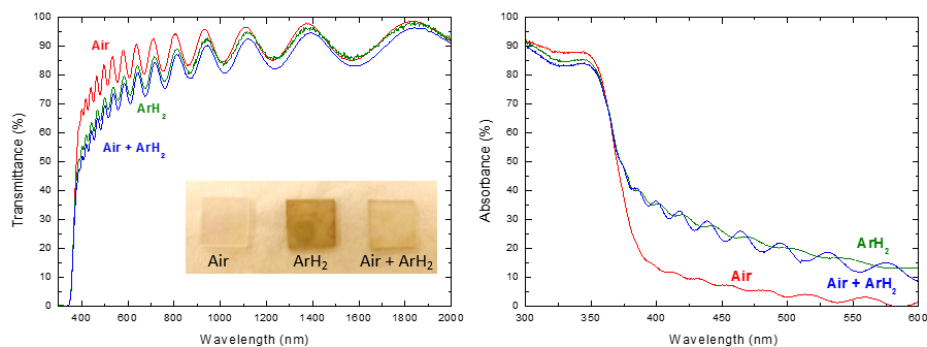
**Figure 3.26:** *Total normalized trasmittance (on the left) and absorbance (on the right) vs. wavelength for samples deposited at 5 Pa of $Ar/O_2$ , after the three thermal treatments (inset: pictures for the differently treated samples).*
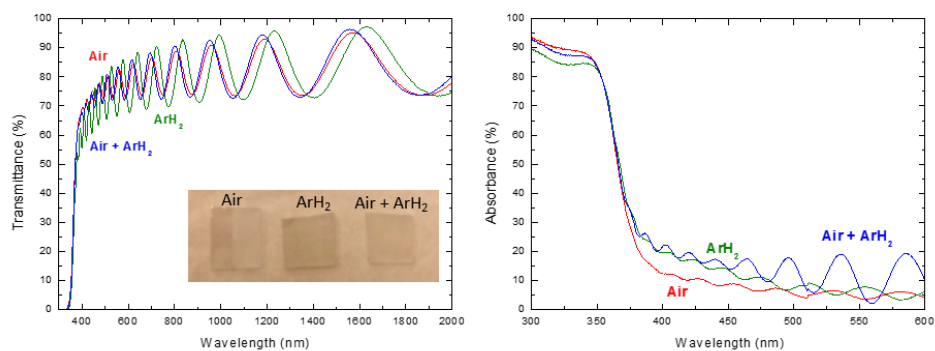


**Figure 3.27:** *Total normalized trasmittance (on the left) and absorbance (on the right) vs. wavelength for samples deposited at 5 Pa of $Ar/H_2$ , after the three thermal treatments (inset: pictures for the differently treated samples).*

78
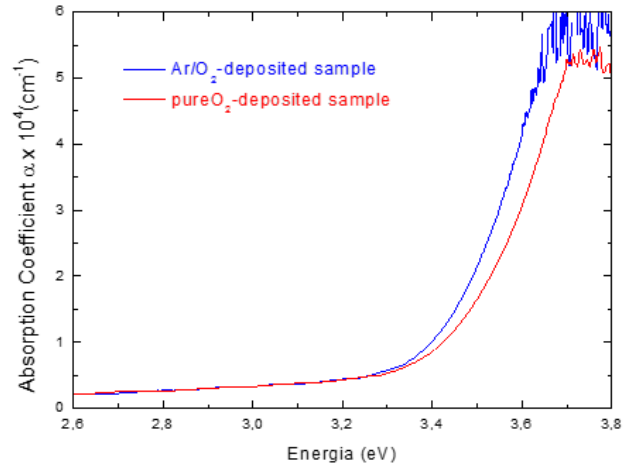
**Figure 3.28:** *Absorption coefficient of the samples deposited at* 5 Pa *of pure* $O_2$ *and* $Ar/O_2$ *after* $Ar/H_2$ *treatment at* 500 °C *for 3 hours.*
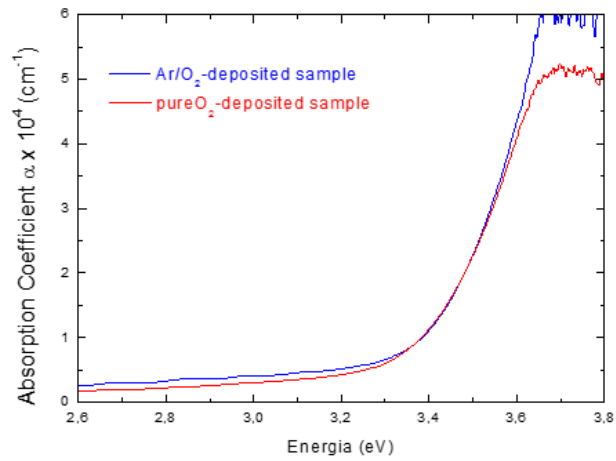


**Figure 3.29:** *Absorption coefficient of the samples deposited at* 5 Pa *of pure* $O_2$ *and* $Ar/O_2$ *after air annealing for 2 hours followed by* $Ar/H_2$ *treatment for 3 hours, both at* 500 °C.
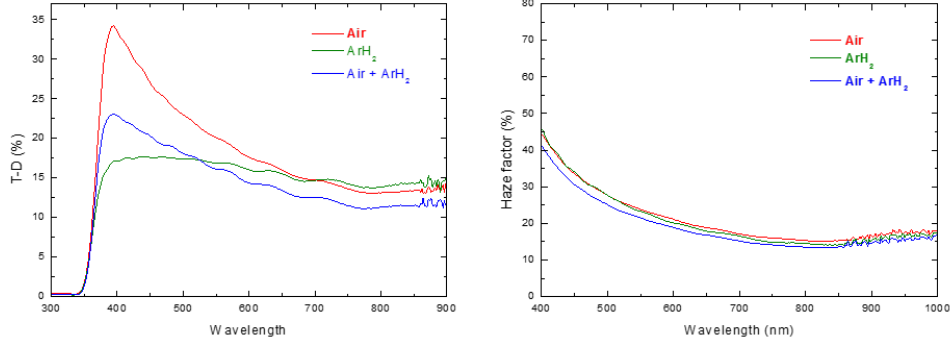
**Figure 3.30:** *Diffused Trasmission vs. wavelength (on the left) and haze factor (on the right)of the samples deposited at 5 Pa of pure $O_2$.*
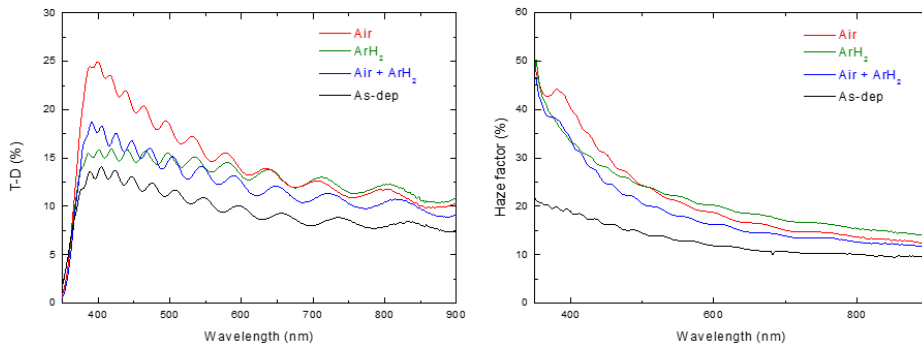


**Figure 3.31:** *Diffused Trasmission vs. wavelength (on the left) and haze factor (on the right) of the samples deposited at 5 Pa of $Ar/O_2$.*
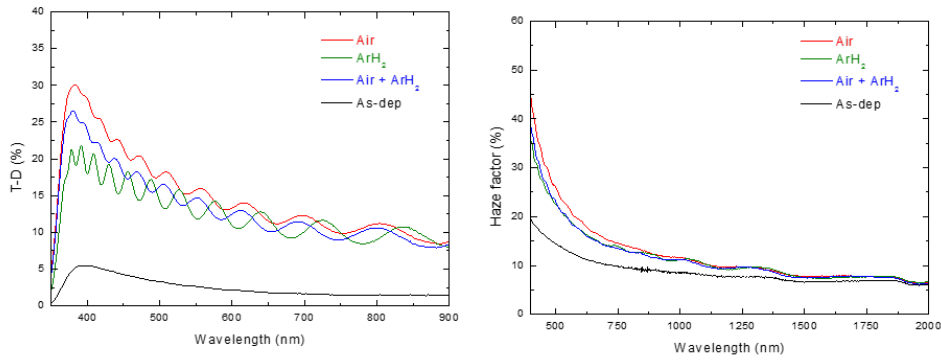


**Figure 3.32:** *Diffused Trasmission vs. wavelength (on the left) and haze factor (on the right)of the samples deposited at 5 Pa of $Ar/H_2$.*

surement is the optical bandgap of the samples. As described in the section 2.3, the bandgap can be calculated by Tauc plot method. Tipically, $\alpha^r$ or $(\alpha h\nu)^r$, where $\alpha$ is the absorption coefficient, is plotted versus energy near the absorption edge and $E_g$ value is extrapolated by linear fitting. For crystalline materials, the value of the exponent (r) depends on the type of the transition and it is generally accepted as 2 for a direct allowed-transition, 1/2 for an indirect allowed transition. As $TiO_2$ has indirect bandgap, 1/2 is used as exponent. Figure 3.33 shows an example of linear fit done on sample deposited at 5 Pa of $Ar/O_2$ and annealed in air for 2 hours at $500\,°C$ followed by hydrogenation in $ArH_2$ atmosphere at $500\,°C$ for 3 hours.

The values of optical bandgap calculated by Tauc plot for all samples are



**Figure 3.33:** *Tauc plot for sample deposited at 5 Pa of $Ar/H_2$ after annealed in Air and $ArH_2$.*

reported in table 3.4. All the annealed samples show the bandgap around $3.2\,eV$, which is the typically anatase optical bandgap. However a higher tail absorption appears for the hydrogenated samples, probably due to the presence of mid-gap defects states.

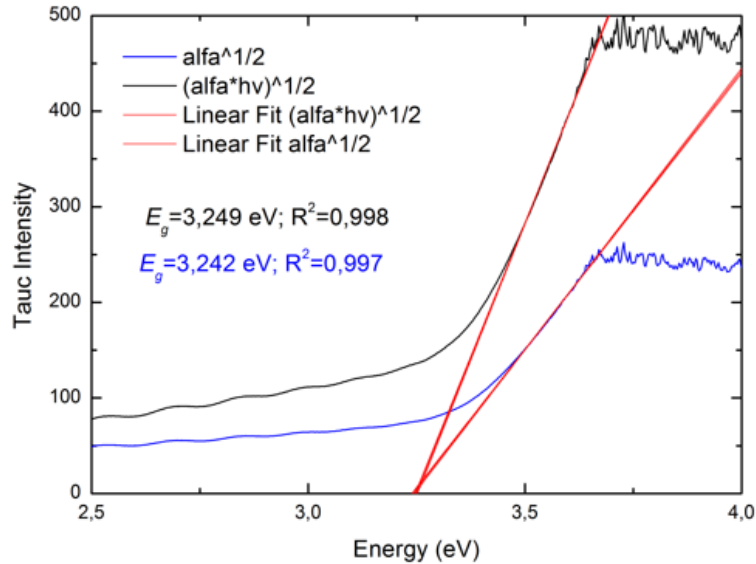| Sample name | Annealing | $E_g \propto (\alpha h\nu)^{1/2}$ (eV) | $R^2$ | $E_g \propto \alpha^{1/2}$ (eV) | $R^2$ |
|---|---|---|---|---|---|
| pure $O_2$-dep | Air | 3.221 | 0.996 | 3.215 | 0.997 |
| | $ArH_2$ | 3.236 | 0.997 | 3.241 | 0.998 |
| | Air + $ArH_2$ | 3.189 | 0.997 | 3.187 | 0.999 |
| $Ar/O_2$-dep | Air | 3.222 | 0.998 | 3.222 | 0.999 |
| | $Ar/H_2$ | 3.252 | 0.998 | 3.244 | 0.998 |
| | Air + $Ar/H_2$ | 3.249 | 0.998 | 3.242 | 0.997 |
| $Ar/H_2$-dep | Air | 3.188 | 0.998 | 3.169 | 0.997 |
| | $Ar/H_2$ | 3.235 | 0.999 | 3.226 | 0.999 |
| | Air + $Ar/H_2$ | 3.224 | 0.999 | 3.194 | 0.997 |

Table 3.4: Optical bandgap measured by tauc plot for different samples.

## 3.6 Photocurrent analysis

PEC characterizations were performed in a 0.1 M KOH electrolyte using a typically three-electrode electrochemical cell configuration. The schematic setup is shown in Figure 3.34. $TiO_2$ hierarchical quasi 1D architectures on
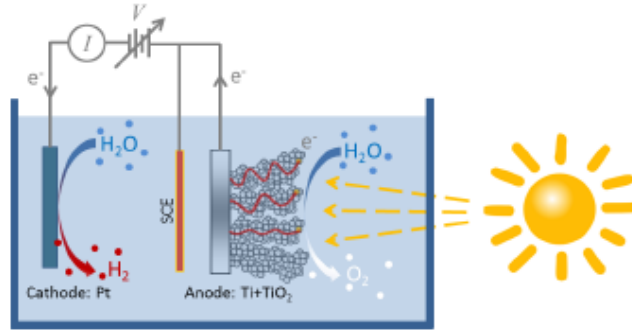


*Figure 3.34: Schematic setup of PEC*

titanium substrate were used as the working electrode; Pt served as the counter electrode; and a satured calomel electrode (SCE) was used as the reference electrode. A light source with intensity of $96\,000\,\mathrm{mW/cm^2}$ was used as solar simulator. Moreover a filter was applied to eliminate the UV light in order to evaluate the visible light effect.

Each sample was tested using the same procedure, which consist of:

- sample preparation;

- measure of open circuit potential (OCP) without illumination;

- lighting of the lamp and measure of OCP under illumination;

- photocurrent measurement under illumination;

- photocurrent measurement in dark;

- photocurrent measurement with UV filter.

Three different tests under illumination were performed and before them the OCP was always measured. Photoelectrochemical efficiencies were also evaluated via the equation:

$$\eta(\%) = \frac{j(V_{redox} - |V_{bias} - V_{OC,light}|)}{P_{light}} \tag{3.1}$$

where j is the photocurrent density ($\mu A/cm^2$), $V_{redox}$ is the standard potential for water-splitting reaction (1.23 V), $V_{bias}$ is the applied potential (bias potential), $V_{OC,light}$ is the potential at open circuit under illumination and $P_{light}$ is the power of incident light (in this case 96 000 $\mu W/cm^2$).

### 3.6.1 Pure O$_2$-deposited samples: effect of annealing treatments

In Figures 3.35 the photocurrent densities under illumination, in dark and with UV filter are reported for the sample deposited at 5 Pa of O$_2$ after air annealing, ArH$_2$ treatment and air followed by ArH$_2$ annealing. In all cases the dark current density remains at very low level ($<1\,\mu A/cm^2$), which indicates that the current observed for the cell is completely due to the photoactivity of the catalyst. Moreover, we can also note that the photocurrent density under illumination with UV filter is very low and very close to the dark current. This means that the photocurrent density is manly due to UV absorption. The photoconversion efficiency ($\eta$) of the photoanode, calculated using the equation (3.1) after air annealing, Ar/H$_2$treatment and air followed by Ar/H$_2$ treatment is shown in Figure 3.36. The maximun value is achieved by air annealed sample. Indeed, in order to evaluate the photocatalytic activity in time, the tests were repeated every month. The results are reported in Figure 3.37. The behaviour of photoanode under illumination seems quite stable also after about four months.

**Figure 3.35:** *Variation of photocurrent density vs applied potential of the sample deposited at 5 Pa of $O_2$ in dark condition (blue line), illumination (red line) and illumination with UV filter (green line), after the three thermal treatments.*



**Figure 3.36:** *Compare the efficiencies of $O_2$ deposited samples after the three different annealing (Air, $ArH_2$ and Air followed by $Ar/H_2$).*
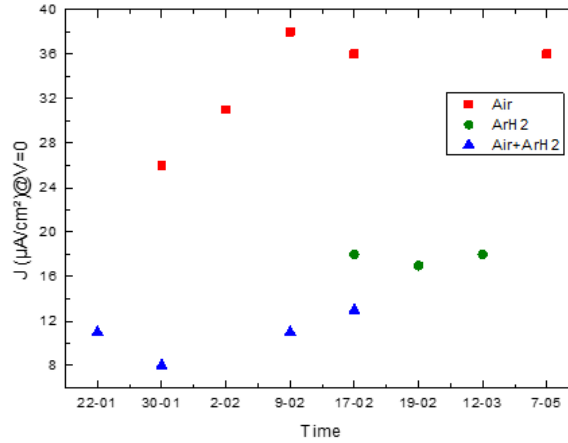
***Figure 3.37:*** *Time stability tests of the samples deposited at 5 Pa of pure $O_2$.*

### 3.6.2 Samples deposited in the other atmosphere: effect of annealing treatments

The same considerations done in the previous section for $O_2$ deposited samples at 5 Pa are also true for the other two set of samples ($Ar/O_2$ and $Ar/H_2$ deposited samples). Here the same spectra are reported in the Figures 3.38, 3.39 and 3.40 for $Ar/O_2$ deposited samples and in the Figures 3.41, 3.42 and 3.43 for $ArH_2$ deposited samples.

By comparing the efficiencies of all samples the $Ar/O_2$ deposited samples appears the most promising from photocatalytic point of view. In particular the samples after air annealing followed by $ArH_2$ treatments shows the highest efficiency, around $0.10\,\%$ (see Figure 3.39). However this value is also very low probably because the photoanodes are inactive in the visible range.
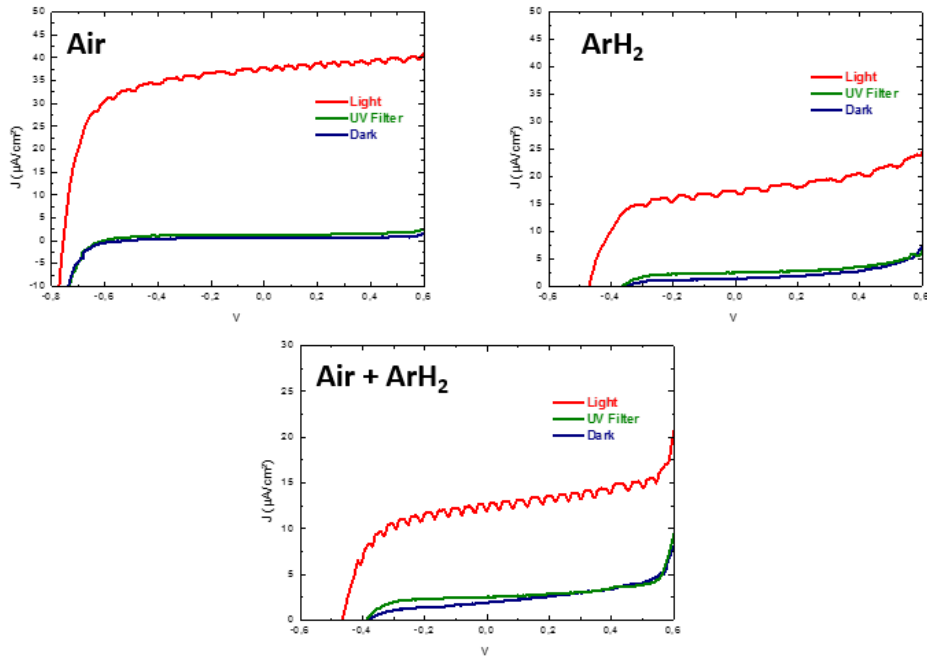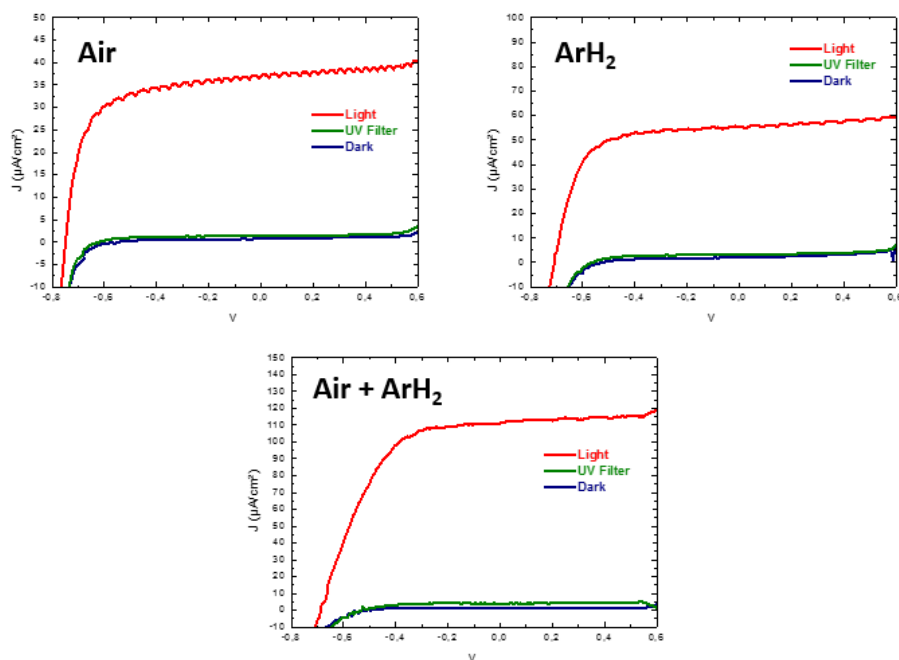
**Figure 3.38:** *Variation of photocurrent density vs applied potential of the sample deposited at 5 Pa of $ArO_2$ in dark condition (blue line), illumination (red line) and illumination with UV filter (green line), after the three thermal treatments.*
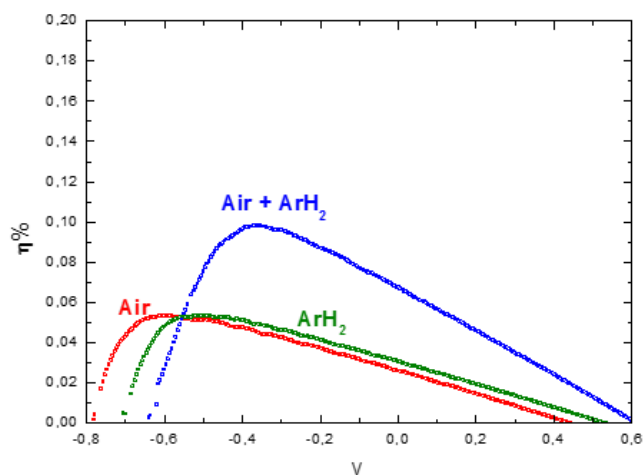


**Figure 3.39:** *Comparison of the efficiencies of $ArO_2$ deposited samples after the three different annealing (Air, $ArH_2$ and Air followed by $Ar/H_2$).*
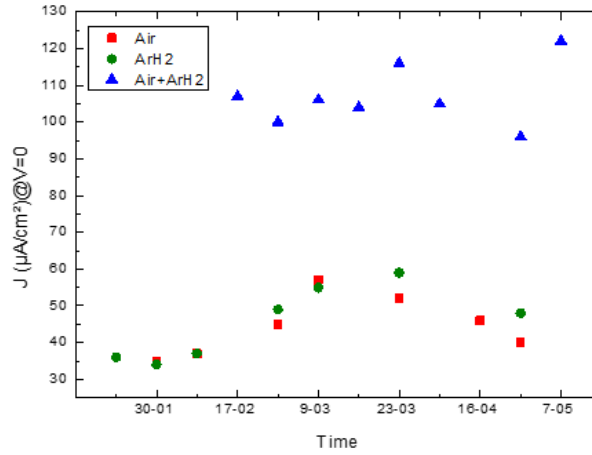
**Figure 3.40:** *Time stability tests of the samples deposited at 5 Pa of $ArO_2$.*
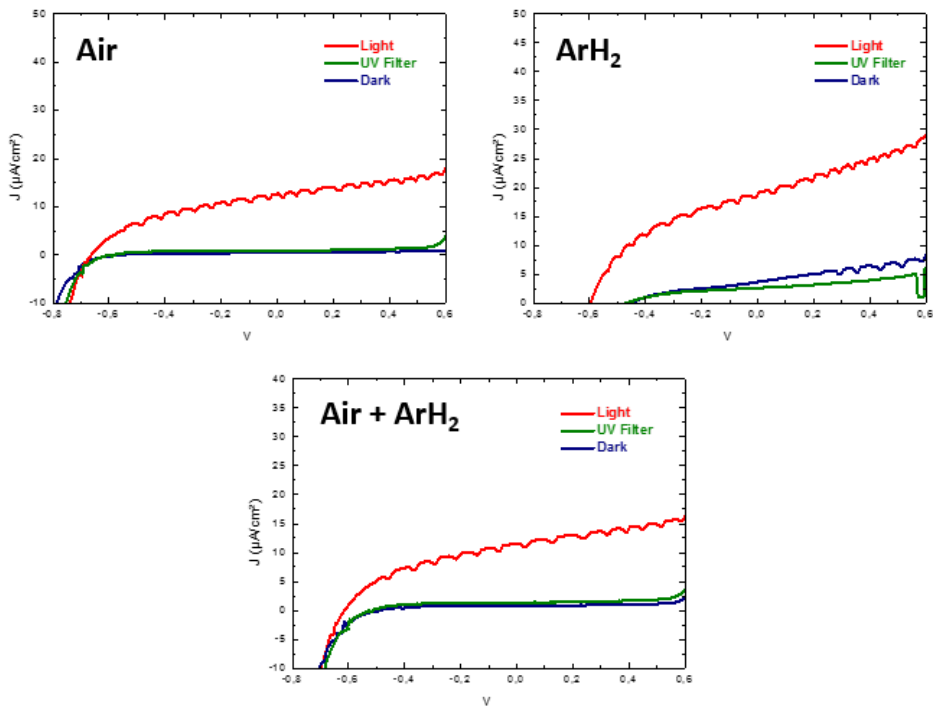


**Figure 3.41:** *Variation of photocurrent density vs applied potential of the sample deposited at 5 Pa of $ArH_2$ in dark condition (blue line), illumination (red line) and illumination with UV filter (green line), after the three thermal treatments.*
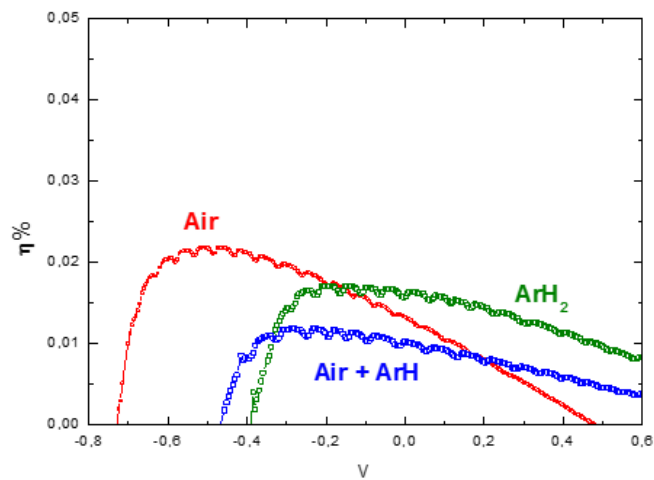
87
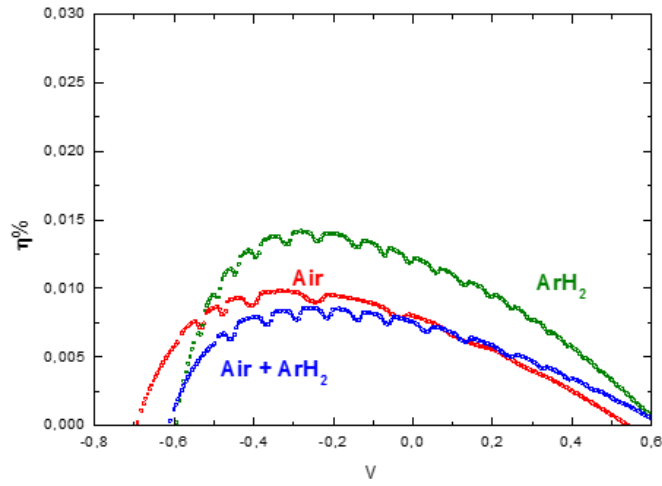
**Figure 3.42:** *Comparison of the efficiencies of $ArH_2$ deposited samples after the three different annealing (Air, $ArH_2$ and Air followed by $Ar/H_2$).*
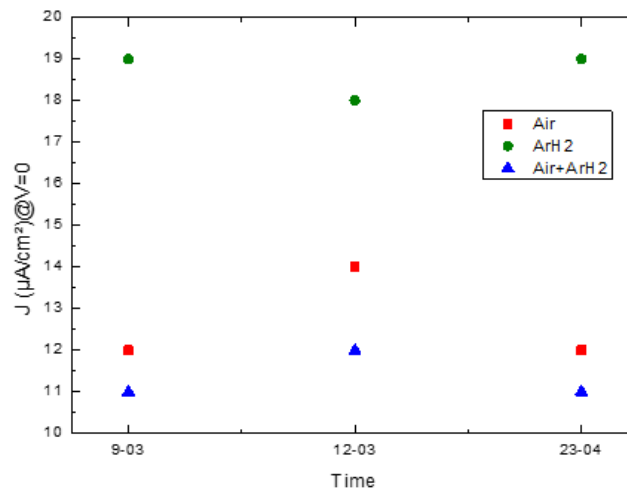


**Figure 3.43:** *Time stability tests of the samples deposited at 5 Pa of $ArH_2$.*

## 3.7 Summary and further developments

In this section the main results discussed in this chapter are reported.

- TiO$_2$ samples deposited in three different background gases (pure O$_2$, Ar/O$_2$ and Ar/H$_2$) are amorphous. Both air annealing and Ar/H$_2$ thermal treatment induce the transition from amorphous into crystalline anatase structure.

- From morphological point of view as deposited samples are nanoporous characterized by vertically oriented domains. After thermal annealing a hierarchical structure which consist of assemblies of nanocrystalline particles of TiO$_2$ appears for the samples deposited in pure O$_2$ and Ar/O$_2$ mixture while the samples grown in Ar/H$_2$ atmosphere become more compact and dense.

- Optical analysis shows that absorption increases in the visible range for samples deposited in pure O$_2$ and Ar/O$_2$ after Ar/H$_2$ thermal treatment and air followed by Ar/H$_2$ annealing. This effect doesn't occur for Ar/H$_2$ deposited samples. Anyway the estimated optical band gap is around 3.2 eV for all samples.

- Finally from photocurrent analysis, the most promising thermal annealing is the double treatment: air annealed at 500 °C for 2 hours followed by Ar/H$_2$ treatment at 500 °C for 3 hours. The maximun values of efficiency are shown for the samples deposited in Ar/O$_2$, while the less performance photoanodes are TiO$_2$ samples prepared by PLD in Ar/H$_2$ atmosphere.

In order to understand the physical mechanism and to evaluate the reproducibility of the best performance sample further analysis are performed. First of all, a sample deposited in Ar/O$_2$ atmosphere at 5 Pa was annealed in air for 5 hours. The Raman spectrum, shown in Figure 3.44 (a) confirms anatase structure, even if a low amount of rutile phase is also present. Photocurrent measuraments are reported in Figure 3.44 (b), the values of current under illumination are comparable with results obtained from the same sample annealed in air for 2 hours. This means that the increase of photocurrent observed in the case of co-treated TiO$_2$ (air annealing for 2

hours followed by hydrogen treatment for 3 hours) is not related to the time of annealing but it depends on hydrogenation.

Second, a copy of the best performance sample, deposited in $Ar/O_2$ at 5 Pa and annealed first in air and then in $Ar/H_2$ was performed in order to evaluate the reproducibility. SEM cross section images are shown in Figure 3.45, the thickness is around 1.5 μm and the morphology is comparable with the old sample treated in the same way. Raman spetrum ($TiO_2$ on silicon substrate) and photoconversion efficiency are reported in Figure 3.46. Again the structure is anatase and the current values of new and old sample are comparable.
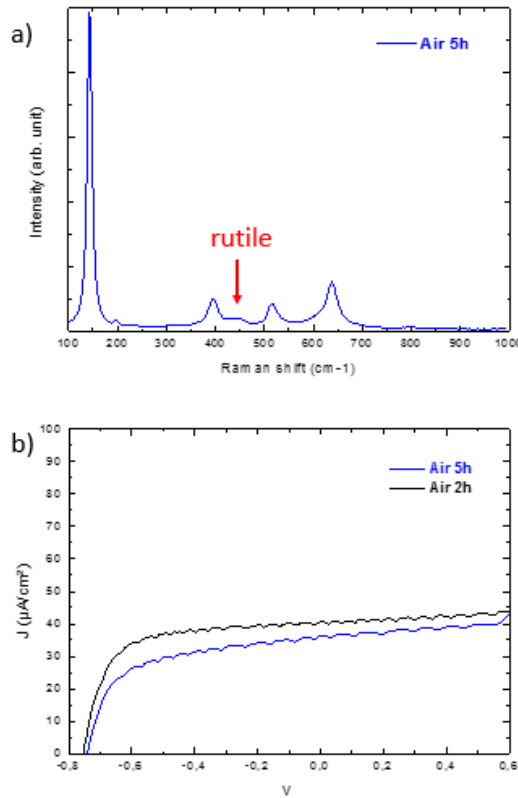


**Figure 3.44:** *a)Raman spectrum of the sample deposited at 5 Pa of $Ar/O_2$ after air annealing at 500 °C for 5 hours b)Comparison of photocurrent values for samples deposited in the same conditions (5 Pa, $Ar/O_2$) after air annealing at 500 °C for 2 hours (black line) and 5 hours (blue line)*
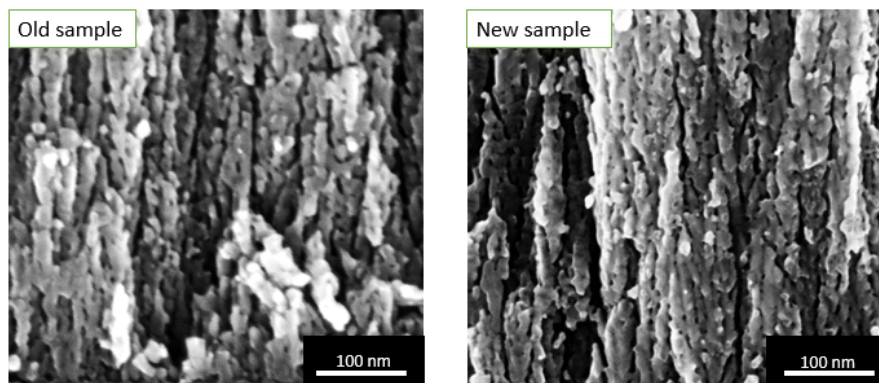
**Figure 3.45:** *Comparison of SEM cross section images of old and new samples associated to best performance photoanode, prepared by PLD at 5 Pa of $Ar/O_2$ after air annealing followed by hydrogen treatment.*
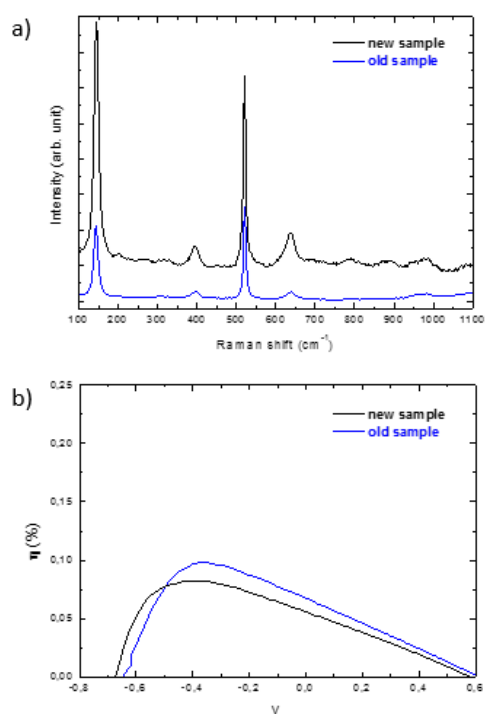


**Figure 3.46:** *Comparison of Raman spectra (a) and photoconversion efficiency (b) of the best performance photoanode and a new sample prepared in the same condition.*

Development of other experimental approches:
preliminary results

This chapter describes other novel approches performed in the attempt to improve morphological and structural properties and photocurrent efficiency of $TiO_2$ samples. The development of these approches is based on considerations deriving from the most significant results presented in chapter 3. In particular, we have followed two strategies:

- increase of post-deposition annealing temperature for the samples deposited in pure $O_2$;

- increase of deposition pressure for the samples deposited in $Ar/H_2$ atmosphere.

The samples deposited in pure $O_2$ were annealed as the previous ones, described in chapter 3, in air for 2 hours, in $Ar/H_2$ gas flow for 3 hours and first in air and then in $Ar/H_2$ for 2 and 3 hours respectively at 650 °C. This choice derived from the results obtained, in the past years in our laboratory.[32] It was demostrated that the increase of temperature during post-deposition thermal treatment from 500 °C to 650 °C leaded to increase photocurrent density over the whole potential range. In addition, in this case, a sample was also annealed in air at 500 °C in order to have a reference, as usual.

The second approch was also derived from previous researches in our laboratory. As already demostrated, by incresing the oxygen background pressure, the film becomes more porous and less dense.[32] As the same way, increasing the $Ar/H_2$ pressure to $10\,PA$ we expected a more porous tree-like morphology respect to the samples deposited at $5\,Pa$, which appear too compact.

In the section 4.1 morphological and structural characterization and photocurrent density of the samples deposited at $5\,Pa$ of pure $O_2$ after thermal treatments at $650\,°C$ are reported while in the section 4.2 the samples deposited in $Ar/H_2$ at $10\,Pa$ are investigated. Finally, a summary of main results is presented in section 4.3.

## 4.1    $O_2$-deposited samples annealed at $650\,°C$

SEM cross section images of the samples deposited at $5\,Pa$ of pure $O_2$ after thermal treatments at $650\,°C$ are shown in Figure 4.1. The sample calcinated
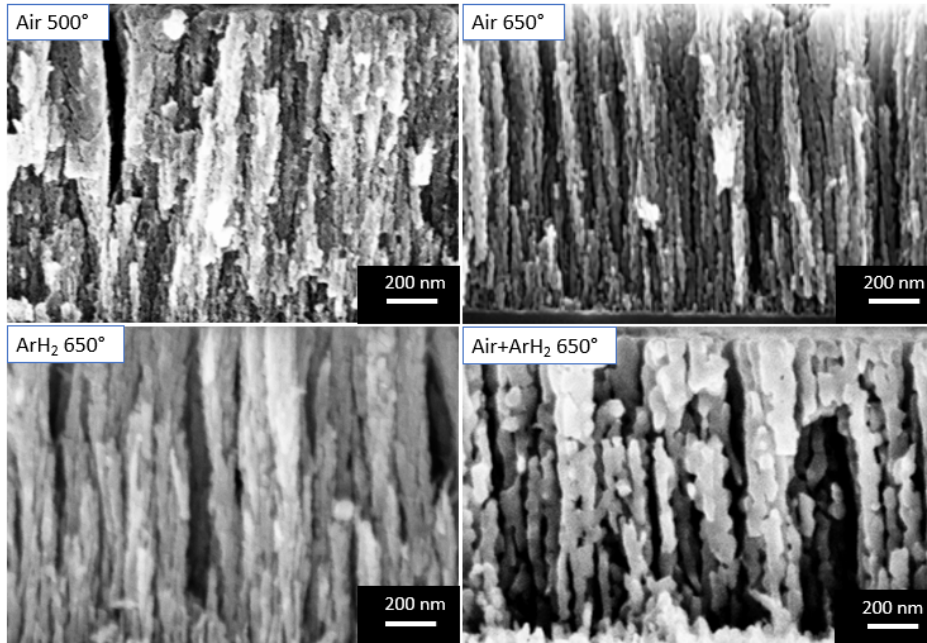


***Figure 4.1:*** *SEM cross section images of the samples deposited in pure $O_2$ at 5Pa after air annealing at $500\,°C$, air annealing at $650\,°C$, $Ar/H_2$ annealing at $650\,°C$ and air followed by $Ar/H_2$ treatment at $650\,°C$.*

at $500\,°C$ is also reported. We can note that the morphology is very similar

## 4.1 O$_2$-deposited samples annealed at $650\,^\circ$C

among all samples, however a coarsening effect or annealing sintering is visible after thermal treatments at $650\,^\circ$C due to higher temperature. In particular, a strong coalescence occurs for the sample calcinated first in air and then in $Ar/H_2$ atmosphere, leading to a quasi 1D columnar structure with evident reduction in porosity.

In Figure 4.2 Raman spectra are reported. Silicon and glass substrates are used for samples calcinated at $650\,^\circ$C and at $500\,^\circ$C respectively. Glass can't withstand high temperature so for samples annealed at $650\,^\circ$C silicon substrate were used. Raman analysis confirms anatase structure for the air treated samples both at $500\,^\circ$C and $650\,^\circ$C, in agreement with the results reported in chapter 3. On the contrary, thermal annealing in $Ar/H_2$ and air annealing followed by hydrogenation induces different Raman spectra. Both sample seem to have a strong amorphous background, due to the presence of amorphous carbon, visible in extended Raman spectrum (results not reported). Raman peaks are not well defined so the crystalline phase is not clear. However for sample annealed first in air and then in $Ar/H_2$, anatase Raman peaks are quite visible, even if trace of rutile are also present, while for sample annealed only in $Ar/H_2$ anatase phase seems to disappear and a transition towards rutile crystalline phase seems to start. In any cases, a decrease of peaks intensity is a proof of a loss of crystallinity. This effect is not clear and understood and it will be object of future studies. Figure



*Figure 4.2:* Raman spectra of the samples deposited at $5\,$Pa of pure $O_2$ after air annealing at $500\,^\circ$C and $650\,^\circ$C (on the left) and after $Ar/H_2$ and air followed by $Ar/H_2$ treatment both at $650\,^\circ$C(on the right).

4.3 shows the phocurrent analysis. As expected, the sample annealed in air
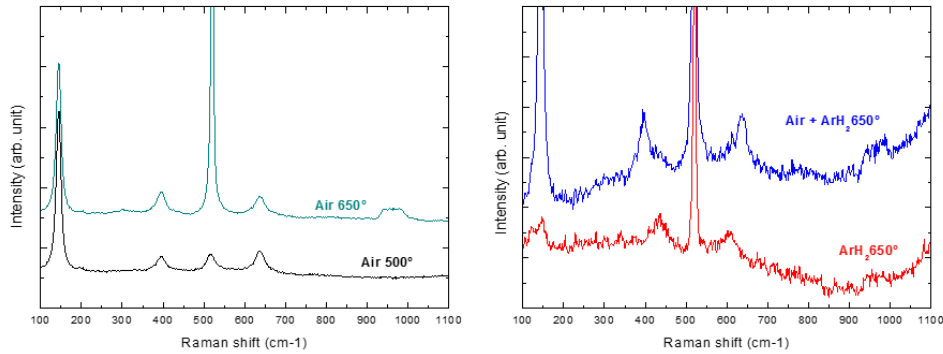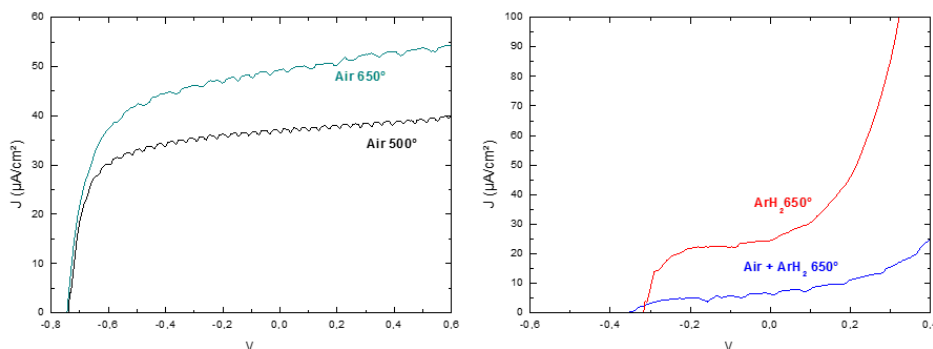
**Figure 4.3:** *Photocurrent density of the samples deposited at* 5 Pa *of pure* $O_2$ *after air annealing at* 500 °C *and* 650 °C *(on the left) and after* $Ar/H_2$ *and air followed by* $Ar/H_2$ *treatment both at* 650 °C*(on the right).*

at 650 °C has a higher photocurrent density than sample annealed in air at 500 °C, in agreement with the previous study.[32] On the contrary, the photocatalytic performance of the samples annealed in $Ar/H_2$ and annealed in air and then in $Ar/H_2$ at 650 °C is poor and unstable. These results can be explained by considering the Raman characterization results, which show a low degree of crystallinity and SEM images, which report a sintering effect, so low surface area, for samples after annealing in $Ar/H_2$ and in first in air and then in $Ar/H_2$.

## 4.2   $Ar/H_2$-deposited samples at 10 Pa

Figures 4.4 and 4.5 show SEM cross section images of the samples deposited in $Ar/H_2$ gas at 10 Pa and at 5 Pa as deposited and after thermal annealing at 500 °C.   By comparing the images, the effect of change of the $Ar/H_2$ background pressure appears. By increasing the pressure from 5 to 10 Pa the samples become more porous and less compact. The hierarchical vertically oriented domains are visible for the samples deposited at 10 Pa both as deposited and after all thermal treatments, as the previous samples deposited in pure $O_2$ and $Ar/O_2$ at 5 Pa.  In agreement with the results presented in chapter 3, again Raman spectra confirm amorphous structure for the as deposited sample and anatase crystalline structure for the samples after the three types of annealing (Figure 4.6). Anatase peaks intensity for $Ar/H_2$ treated $TiO_2$ appears very low probably due to the presence of photolumi-

**Figure 4.4:** *Comparison of SEM cross section images of the samples deposited in Ar/H$_2$ background atmosphere at 5 Pa and 10 Pa, as deposited and after air annealing.*
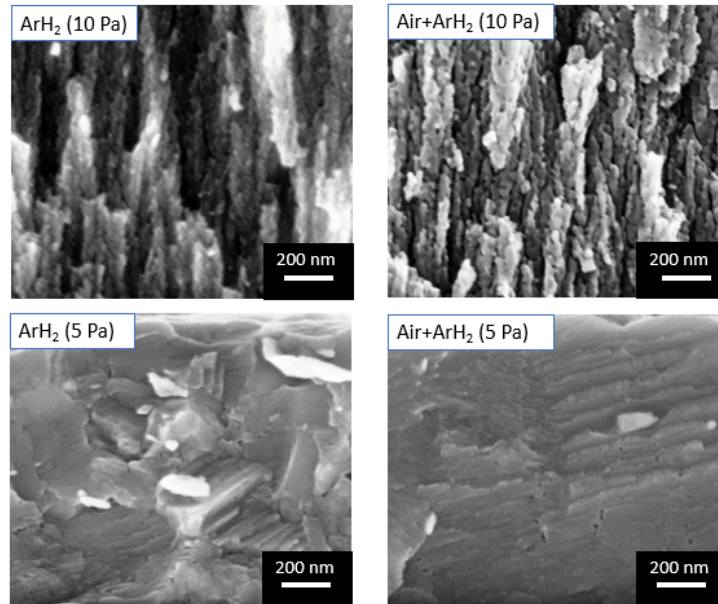


**Figure 4.5:** *Comparison of SEM cross section images of the samples deposited in Ar/H$_2$ background atmosphere at 5 Pa and 10 Pa, after hydrogen treatment and air annealing followed by hydrogenn treatment.*

nescence background.
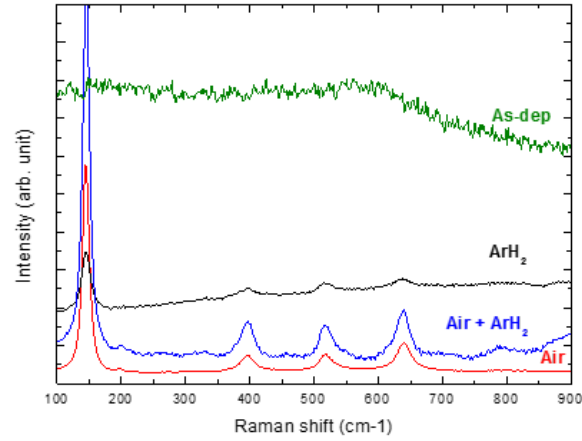


**Figure 4.6:** *Raman spectra of the samples deposited at 10 Pa of $Ar/H_2$ mixture as deposited (green line), after air annealing at $500\,°C$ (red line), after $Ar/H_2$ treatment at $500\,°C$ (black line) and after air annealing followed by $ArH_2$ treatment both at $500\,°C$ (blue line).*



**Figure 4.7:** *Comparison of photocurrent density od the samples deposited in $Ar/H_2$ background gas at $5\,Pa$ and $10\,Pa$ after air annealing $Ar/H_2$ treatment and air followed by $Ar/H_2$ annealing.*

Finally, photocurrent analysis shows an increase of efficiency for the sample deposited at $10\,Pa$ of $Ar/H_2$ after air annealing and air annealing followed by hydrogenation in comparison to the samples deposited at $5\,Pa$. On the contrary, the sample deposited in $Ar/H_2$ at $5\,Pa$ after only $Ar/H_2$ thermal treatment shows higher efficiency than sample deposited at $10\,Pa$. However, as seen in Figure 4.7, in all cases the efficiency lies under 0.015 %. This value is too low and in any case the other two set of samples, deposited in pure $O_2$ and $Ar/O_2$ mixture at $5\,Pa$, show higher efficiency. In conclusion, we can observed that in general this strategy appears unpromising, probably the deposition in $Ar/H_2$ atmosphere introduce too defects.

## 4.3 Summary

In summary, these new developments have demostrated that the increse of post-annealing temperature from $500\,^{\circ}C$ to $650\,^{\circ}C$ doesn't lead to improvement of performance of $TiO_2$ photoanode (deposited at 5 Pa of pure $O_2$), especially for hydrogenated samples.

- From a morphological point of view thermal treatments at $650\,^{\circ}C$ don't change the overall morphology, but by comparing with the samples calcinated at $500\,^{\circ}C$, a coarsening/coalescence phenomenon of nanoparticles occurs, in particular for sample after air and $Ar/H_2$ annealing.

- Raman analysis shows anatase crystalline structure for air-annealed samples, while different spectra appear for hydrogenated samples. This effect is not still clear and it will be obyect of future studies.
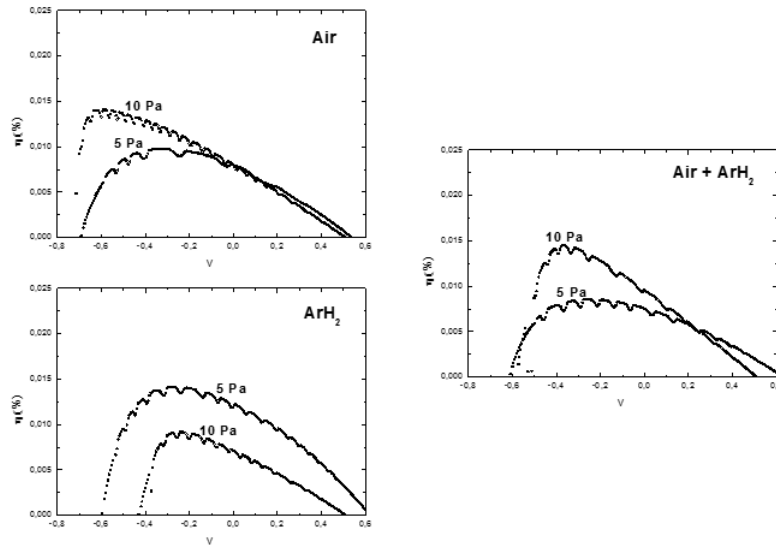
- Photocurrent analysis shows higher current density for air-annealed $TiO_2$ at $650\,^{\circ}C$ by comparison with air-annealed sample at $500\,^{\circ}C$. Instead the photocurrent performance drops after both $Ar/H_2$ treatment and air annealed followed by $Ar/H_2$ treatment.

The last consideration takes into account the samples deposited at $10\,Pa$ and $5\,Pa$ of $Ar/H_2$.

- By increasing the deposition pressure the morphology changes from compact and dense to porous and hierarchical.

- Raman spectra confirm the general trend described in chapter 3: amorphous and crystalline anatase structures for as-deposited and annealed-$TiO_2$ samples respectively.

- Finally, photocurrent analysis doesn't show a significant increase of photoanode performance for samples deposited at $10\,Pa$. Both deposited sample at $5\,Pa$ and $10\,Pa$ of $Ar/H_2$ show a too low efficiency value (below 0.015%).

CHAPTER 5

Conclusions and perspectives

Large surface area, low carriers recombination, preferential charge transport and visible light absorption are among the most important properties suitable for applications of novel photoanodes in PEC water splitting. These requirements have been addressed in the present work, leading to the development of nanostructured hydrogenated $TiO_2$ prepared at room temperature by Pulsed Laser Deposition (PLD). The aim of my thesis is to investigate if hydrogen treatments can be used as a general strategy to improve the performance of hierarchical quasi 1D nanomaterials $TiO_2$ as photoanode for PEC water splitting. In order to obtain hydrogenated-$TiO_2$ we have followed two strategies: introduction of hydrogen during the deposition stage (PLD deposition in $Ar/H_2$ atmosphere in addition to pure $O_2$ and $Ar/O_2$ deposition background gas), or during post-deposition thermal annealing (annealing in $Ar/H_2$ flow and double annealing, first in air and then in $Ar/H_2$).

Morphological properties were first investigated, identifying the effect of the different background gas during deposition at $5\,Pa$ (pure $O_2$, $Ar/O_2$ mixture at 50 % and $Ar/H_2$ gas with 3% of $H_2$) and of different thermal treatments at $500\,°C$ (air annealing, $Ar/H_2$ treatment and air annealing followed by $Ar/H_2$ treatment). In the case of pure $O_2$ or $Ar/O_2$ background gas deposition, the morphology appears nanoporous, characterized by a vertically oriented growth and it evolves towards a hierarchical assembly of

nanoparticles after thermal annealing. On the contrary $Ar/H_2$ atmosphere deposition at 5 Pa leads to more compact and dense film both as deposited and after thermal annealing.

To determine the crystal structure and possible phase changes during thermal treatments, Raman analysis was performed. In any case it reveals the same general trend: amorphous structure for as deposited samples and anatase crystalline structure for all annealed samples.

From optical analysis, the effect of hydrogenation appears. The samples deposited in pure $O_2$ and $Ar/O_2$ after hydrogen treatment and air annealing followed by hydrogenation show a tail absorption shift towards the visible range. This is probably due to the presence of mid-gap tail states associated to oxygen vacancies, induced by $Ar/H_2$ annealing, even though this effect is not fully understood and has still to be investigated. However, this phenomenon is very low for $Ar/H_2$ deposited samples. For all samples the estimated band gap is around 3.2 eV, the typical value of anatase $TiO_2$ band gap.

Finally, the photocurrent measurements (the tests were performed at Laboratory of Catalysis and Catalytic Processes, LCCP, by Prof.ssa Nova group) reveals that the most promising thermal annealing is the double treatment: air annealing for 2 hours and $Ar/H_2$ treatment for 3 hours both at 500 °C. The maximum efficiency value is obtained for $Ar/O_2$ deposited sample, around 0.15%.

In order to understand the physical mechanism and the reproducibility of the best performance sample, further analysis was carried out. A sample deposited in $Ar/O_2$ was annealed in air at 500 °C for 5 hours, displaying a photocurrent performance comparable with the same sample annealed in air for 2 hours. This evidence confirms that the increase of photo-activity is due to hydrogen treatment and not to the duration of annealing. Indeed a copy of the most promising sample was prepared in the same way in order to investigate the reproducibility. The new samples confirm the previous results.

Further developments performed on $Ar/H_2$ background gas deposited samples suggest that the deposition in $Ar/H_2$ atmosphere is not efficient for PEC water splitting application. New samples were prepared at 10 Pa of $Ar/H_2$ in order to have a more porous morphology in comparison to samples deposited at 5 Pa. Although the new samples have desired morphology

and Raman spectra show anatase crystalline phase, the new photocurrent performances appear also poor. The efficiency of both samples deposited at 5 Pa and 10 Pa lies below 0.015%. For this reason this strategy has been ignored.

Air annealing and hydrogen treatments were also carried out at 650 °C on samples deposited at 5 Pa of pure $O_2$, displaying negative results from a phoelectrochemical point of view. The morphology is similar to the samples treated at 500 °C, however a coarsening effect or annealing sintering of nanoparticles appears especially for sample annealed first in air and then in $Ar/H_2$. Raman spectra confirm anatase crystalline phase for sample annealed in air and in air followed by hydrogen treatment, even though in the last case an amorphous background appears. For samples annealed in $Ar/H_2$ seems to indigate a significant loss of crystallinity together with the presence of the rutile phase for $Ar/H_2$ annealing. In this case a decrease of surface area and of crystallinity probably causes the decrease of photocurrent density.

Among the possible future perspectives deriving from this work, it is possible to cite a deeper study of different thermal annealing, changing some of the variables that affect the sample performance (e.g.annealing duration or temperature). The three thermal treatments at 650 °C will be performed on other set of samples ($Ar/O_2$ deposited samples). In addition, a new hydrogen treatment will be investigated, exploiting the PLD apparatus equipped with ion gun. An Ion Gun typically refers to an instrument that generates a beam of ions with a well defined energy distribution. The ion beam is produced from a plasma that has been confined within a volume. Ions of a particular energy are extracted, accelerated, collimated and/or focused on the samples, previously annealed. The plasma is made starting from a mixture gas of Ar and $H_2$ with 3% of hydrogen. In this way we will try to introduce hydrogen and/or to obtain substechiometric $TiO_2$, by exposure to an ion beam. Finally, new target deposition will be investigate (e.g. metallic Ti target) and new characterization methods will be employed, such as X-Ray Diffraction (XRD) and Energy Disperdive X-Ray Spectroscopy (EDXS) in order to understand what happen into material at atomic scale. The role of hydrogen in producing lattice disorder in the nanocrystals must be clarified.

# Bibliography

(1) Osterloh, F. E.; Parkinson, B. A. *MRS Bulletin* **2011**, *36*, 17–22.

(2) Momirlan, M.; Veziroglu, T. N. *International Journal of Hydrogen Energy* **2005**, *30*.

(3) Anpo, M.; Kishiguchi, S.; Ichihashi, Y.; Takeuchi, M.; Yamashita, H.; Ikeue, K.; Morin, B.; Davidson, A.; Che, M. *Research on Chemical Intermediates* **2001**, *27*, 459–467.

(4) Umebayashi, T.; Yamaki, T.; Itoh, H.; Asai, K. *Journal of Physics and Chemistry of Solids* **2002**, *63*, 1909–1920.

(5) Reber, J. F.; Rusek, M. *The Journal of Physical Chemistry* **1986**, *90*, 824–834.

(6) Paulose, M.; Mor, G. K.; Varghese, O. K.; Shankar, K.; Grimes, C. A. *Journal of photochemistry and photobiology A: Chemistry* **2006**, *178*, 8–15.

(7) Fonzo, F. D.; Casari, C. S.; Russo, V.; Brunella, M. F.; LiBassi, A.; Bottani, C. E. *Nanotechnology* **2009**, *20*, 015604.

(8) Chen, X.; Liu, L.; Yu, P. Y.; Mao, S. S. *Science* **2011**, *331*, 746–750.

(9) Nowotny, J.; Sorrell, C. C.; Sheppard, L. R.; Bak, T *International Journal of Hydrogen Energy* **2005**, *30*, 521–544.

(10) Akira Fujishima, K. H. *Nature* **1972**, *238*, 37–8.

(11) Bak, T; Nowotny, J; Rekas, M; Sorrell, C. C *International Journal of Hydrogen Energy* **2002**, *27*, 991–1022.

105

(12)     Wang, G.; Ling, Y.; Wang, H.; Xihong, L.; Li, Y. *Journal of Photochemistry and Photobiology C: Photochemistry Reviews* **2014**, *19*, 35–51.

(13)     Walter, M. G.; Warren, E. L.; McKone, J. R.; Boettcher, S. W.; Mi, Q.; Santori, E. A.; Lewis, N. S. *Chemical reviews* **2010**, *110*, 6446–6473.

(14)     Memming, R. In *Semiconductor Electrochemistry*, 2008.

(15)     Van de Krol, R.; Liang, Y.; Schoonman, J. *Journal of Materials Chemistry* **2008**, *18*, 2311.

(16)     Sivula, K.; Formal, F. L.; Grtzel, M. *Chemistry of Materials* **2009**, *21*, 2862–2867.

(17)     Chen, X.; Shen, S.; Guo, L.; Mao, S. S. *Chemical Reviews* **2010**, *110*, 6503–6570.

(18)     Murphy, A. B.; Barnes, P. R. F.; Randeniya, L. K.; Plumb, I. C.; Grey, I. E.; Horne, M. D.; Glasscock, J. A. *International Journal of Hydrogen Energy* **2006**, *31*.

(19)     Roel van de Krol, M. G. In *Photoelectrochemical Hydrogen Production*, 2012.

(20)     Choi, W.; Termin, A.; Hoffmann, M. R. *The Journal of Physical Chemistry* **1994**, *98*, 13669–13679.

(21)     Hameed, A.; Gondal, M. A.; Yamani, Z. H. *Catalysis Communications* **2004**, *5*, 715–719.

(22)     Chen, X.; Glans, P.-A.; Qiu, X.; Dayal, S.; Jennings, W. D.; Smith, K. E.; Burda, C.; Guo, J. *Journal of Electron Spectroscopy and Related Phenomena* **2008**, *162*, 67–73.

(23)     Asahi, R.; Morikawa, T.; Ohwaki, T.; Aoki, K.; Taga, Y. *science* **2001**, *293*, 269–271.

(24)     Yashima, M.; Lee, Y.; Domen, K. *Chemistry of materials* **2007**, *19*, 588–593.

(25)     Tachikawa, T.; Tojo, S.; Kawai, K.; Endo, M.; Fujitsuka, M.; Ohno, T.; Nishijima, K.; Miyamoto, Z.; Majima, T. *The Journal of Physical Chemistry B* **2004**, *108*, 19299–19306.

(26) Khan, S. U. M.; Al-Shahry, M.; Ingler, W. B. *Science* **2002**, *297*, 2243–2245.

(27) Reyes-Garcia, E. A.; Sun, Y.; Raftery, D. *The Journal of Physical Chemistry C* **2007**, *111*, 17146–17154.

(28) Li, D.; Haneda, H.; Hishita, S.; Ohashi, N. *Chemistry of Materials* **2005**, *17*, 2596–2602.

(29) Xu, Q. C.; Wellia, D. V.; Yan, S.; Liao, D. W.; Lim, T. M.; Tan, T. T. Y. *Journal of hazardous materials* **2011**, *188*, 172–180.

(30) Jitputti, J.; Suzuki, Y.; Yoshikawa, S. *Catalysis Communications* **2008**, *9*, 1265–1271.

(31) Grimes, C. A.; Varghese, O. K.; Ranjan, S. In *Light, Water, Hydrogen*, Grimes, C. A., Varghese, O. K., Ranjan, S., Eds.; Springer US: 2008, pp 35–113.

(32) Matarrese, R.; Nova, I.; LiBassi, A.; Casari, C. S.; Russo, V. *Chemical Engineering* **2014**, *41*.

(33) Shen, S.; Mao, S. S. *Nanophotonics* **2012**, *1*, 31–50.

(34) Mao, S. S.; Shen, S. *Nature Photonics* **2013**, *7*, 944–946.

(35) Chen, J.-J.; Wu, J. C. S.; Wu, P. C.; Tsai, D. P. *The Journal of Physical Chemistry C* **2011**, *115*, 210–216.

(36) Hernndez-Alonso, M. D.; Fresno, F.; Surez, S.; Coronado, J. M. *Energy & Environmental Science* **2009**, *2*, 1231.

(37) Kudo, A.; Miseki, Y. *Chemical Society Reviews* **Dec. 16, 2008**, *38*, 253–278.

(38) Wang, G.; Wang, H.; Ling, Y.; Tang, Y.; Yang, X.; Fitzmorris, R. C.; Wang, C.; Zhang, J. Z.; Li, Y. *Nano Letters* **2011**, *11*, 3026–3033.

(39) Hoang, S.; Guo, S.; Hahn, N. T.; Bard, A. J.; Mullins, C. B. *Nano Letters* **2012**, *12*, 26–32.

(40) Liu, L.; Yu, P. Y.; Chen, X.; Mao, S. S.; Shen, D. Z. *Physical Review Letters* **2013**, *111*, 065505.

(41) Hu, Y. H. *Angewandte Chemie International Edition* **2012**, *51*, 12410–12412.

(42) Hoang, S.; Berglund, S. P.; Hahn, N. T.; Bard, A. J.; Mullins, C. B. *Journal of the American Chemical Society* **2012**, *134*, 3659–3662.

(43) Liu, N.; Schneider, C.; Freitag, D.; Hartmann, M.; Venkatesan, U.; Mueller, J.; Spiecker, E.; Schmuki, P. *Nano Letters* **June 2014**, *14*, 3309–3313.

(44) Carlo S. Casari, A. L. In *Advances in Laser and Optics Research*, 2011.

(45) D. Brandon, W. D. K., *Microstructural Characterization of Materials*, 2008.

(46) D. A. Skoog, J. J. L. In *Chimica analitica strumentale*, 1995.

(47) Tauc, J. *Materials Research Bulletin* **1968**, *3*, 37–46.

(48) Li Bassi, A.; Cattaneo, D.; Russo, V.; Bottani, C. E.; Barborini, E.; Mazza, T.; Piseri, P.; Milani, P.; Ernst, F. O.; Wegner, K.; Pratsinis, S. E. *Journal of Applied Physics* **2005**, *98*, 074305.

(49) Mona P. Moreta Richard Zallena, D. P. V. S. B. D. *Thin solid films* **2000**.

(50) Yan, Y.; Han, M.; Konkin, A.; Koppe, T.; Wang, D.; Andreu, T.; Chen, G.; Vetter, U.; Morante, J. R.; Schaaf, P. *Journal of Materials Chemistry A* **2014**, *2*, 12708–12716.